CHARACTERIZATION OF PLASMA-POLYMERIZED POLYETHYLENE GLYCOL-LIKE FILMS

A Dissertation
Presented to
The Academic Faculty

by

Shantanu Chaturvedi Pathak

In Partial Fulfillment
of the Requirements for the Degree
Doctor of Philosophy in the
School of Chemical and Biomolecular Engineering

Georgia Institute of Technology
December 2008

CHARACTERIZATION OF PLASMA-POLYMERIZED POLYETHYLENE GLYCOL-LIKE FILMS

Approved by:

Dr. Dennis W. Hess, Advisor
School of Chemical and Biomolecular Engineering
Georgia Institute of Technology

Dr. L. Andrew Lyon
School of Chemistry and Biochemistry
Georgia Institute of Technology

Dr. Clifford L. Henderson
School of Chemical and Biomolecular Engineering
Georgia Institute of Technology

Dr. J. Carson Meredith
School of Chemical and Biomolecular Engineering
Georgia Institute of Technology

Dr. Mark R. Prausnitz
School of Chemical and Biomolecular Engineering
Georgia Institute of Technology

Date Approved: August 18th, 2008

To my parents, Udaya and Sudha Pathak

ACKNOWLEDGEMENTS

I would first like to thank my advisor and research mentor Prof. Dennis W. Hess, who not only provided support and direction for my thesis work, but also contributed substantially in training a mind capable of surviving and excelling in professional environments. I also owe a lot to the Hess group members, all of whom provided a stimulating environment to work in, regardless of whether our discussions included research-related topics. These people include Dr. Galit Levitin, Dr. Ashwini Sinha, Dr. Ingu Song, Dr. Prabhakar Tamirisa, Dr. Lingbo Zhu, Yonghao Xiu, Balamurali Balu, Ashish Pande and Fangyu Wu. Special thanks go to the first three individuals on the list, with whom I have developed an especially close working and personal relationship.

To the members of my doctoral committee: Prof. Clifford L. Henderson, Prof. Mark R. Prausnitz, Prof. L. Andrew Lyon and Prof. J. Carson Meredith. I appreciate and am grateful for all their suggestions, critique and honest evaluations of my work. This extends to all the members of their groups and all others who compromised their time and efforts to help a fellow graduate student gather and analyze data.

I would like to thank my family, without whom this work would not have been possible or worthwhile. To my sister, Pallavi Medepalli, a source of comfort, to my brother, Sudhanshu Pathak, who always provided an arena of spirited discussion, to my father, Udaya Pathak, a man of undying dreams for his youngest, and my mother, Sudha Pathak, who provided something only a mother can, hope. Finally, I would like to thank my fiancé, Neha Kaushik, with whom I am lucky enough to share this and all future successes.

TABLE OF CONTENTS

LIST OF TABLES

LIST OF FIGURES AND SCHEMES

Page

SUMMARY

A parallel-plate capacitively-coupled plasma deposition system was designed and built for the growth of polyethylene glycol-like films. Deposition rate, bonding structure and dissolution and swelling behavior was characterized as a function of input RF power, reactor pressure and substrate temperature to provide information on the relationship between input plasma parameters and film properties. For the conditions studied in this thesis, deposition rates increased at increasing input powers and operating pressures and decreasing substrate temperatures. The PEG-like coatings resembled higher molecular weight solution-polymerized PEG films with a higher crosslinked structure. Manipulation of plasma deposition conditions allowed control of film crosslink density and resulted in tunable dissolution and swelling properties of the PEG-like polymer. At higher applied powers, lower operating pressures, and higher substrate temperatures, films had a higher crosslink density, thus leading to slower dissolution rates and smaller extents of swelling. Void space openings of swelled-state, PEG-like films were determined using electrophoretic drift and diffusion-controlled transport of fluorophore-tagged PAMAM dendrimers into the bulk of the coating. PAMAM dendrimers were used because of their well-defined sizes and negatively-charged succinamic acid surface groups as a means to probe pore sizes of the plasma films. It was estimated that the upper bound of pore size diameters in the plasma polymer was approximately equal to ~5.5-6.0 nm. Positron annihilation lifetime spectroscopy was used to determine average pore sizes and was estimated to equal ~0.60-0.65 nm.

CHAPTER 1

INTRODUCTION

1.1 Motivation

Coronary artery disease (CAD) is a condition where blockage of coronary arteries are prevented from delivering oxygenated blood to the heart muscle. According to 2005 statistics from the American Heart Association,[1] cardiovascular heart disease affected more than 15 million people in the United States. One way of combating coronary artery disease that does not involve invasive bypass surgery is the installation of stents, which are hollow cylindrical tubes 2-4 mm in diameter and 15-20 mm in length with a patterned slit structure and controlled geometry.[2] Stents first came to the forefront in biomedical device research in the early 1990s,[3] with the first patient trials of bare metal stents (BMS) beginning in the late 1980s[4, 5] and the seminal work being conducted as early as the late 1960s[6] and 1970s.[7]

Despite the overwhelming success in the development of stent technology through the 1990s and early 2000s, many researchers who performed pathological studies on patients after implantation found that occlusion to the stented artery reoccured soon after installation in a process called restenosis.[8-10] Restenosis is the renarrowing or blockage of an artery at the same site where treatment, such as an angioplasty or stent procedure, has already taken place. Of the patients that received BMS, about 25-30% suffered from coronary artery restenosis.[3] As a means to combat restenosis in patients, drug-eluting stents (DES) were gaining attention as possible replacements for first-generation BMS and by 2003, DES were released for clinical use.[11] These medical devices are stents carrying a coating, usually polymer, which slowly elute drugs into the coronary vessel walls. Results from clinical trials indicate that drug-eluting stent implantation reduces

restenosis rates to 7-8%, more than a three-fold reduction in comparison with rates for BMS.[3] Recent studies,[12-14] however, reflect concern regarding DES safety in patients due to late (>30 days) and very late (>1 year) stage thrombosis. This suggests that DES technology, while promising, still requires significant research for insights into: drug-coating interactions, drug release kinetics, mechanism of delivery, etc.

Thin film barrier technology has also been of interest since the mid-1970s. Barriers for food and medical applications are another area where significant efforts have been focused.[15-18] Specifically, barrier coating applications for food and medical packaging mainly require oxygen and water vapor diffusion barriers, although packaging and industrial applications also require barriers to other permeants. The use of plasma-enhanced chemical vapor deposition (PECVD) processes has been studied[17, 19, 20] as a means to lay high barrier silicon dioxide (SiO_2) and polymer[21] thin films to prevent gas permeation. Plasma-polymerization is a possible alternative because plasma-deposited polyethylene glycol films (1) are mechanically robust, thus allowing the user to handle the packaged good without loss of barrier performance, (2) exhibit good adhesion and controlled thicknesses to the packaging surface, and (3) are theoretically non-invasive and biocompatible in nature.

In this thesis, we focus on the characterization of the bulk properties of plasma-polymerized polyethylene glycol (PEG)-like films. Our intent is to address the common links between DES and barrier film applications. Application of PEG-like films to drug delivery or barrier layers requires a fundamental understanding of their structure and properties. In particular, internal defects and pore sizes are critical properties of such film materials that likely determine their applicability in drug loading for stents and water permeation for protection purposes. Fundamental insight into defects and pore sizes, can help explain film response behavior such as dissolution and swelling, both of which are important for the implementation of such films in a variety of applications.

1.2 References

1. Heart disease and stroke statistics. In American Heart Association: Dallas, 2008.

2. Kathuria, Y. P., The potential of biocompatible metallic stents and preventing restenosis. *Mater. Sci. Eng. A* 2006, 417, 40-48.

3. Panescu, D., Emerging technologies - drug eluting stents. *IEEE Eng. Med. Biol. Mag.* 2004, 21-23.

4. Sigwart, U.; Puel, J.; Mirkovitch, V.; Joffre, F.; Kappenberger, L., Intravascular stents to prevent occlusion and restenosis after transluminal angioplasty. *N. Engl. J. Med.* 1987, 316, 701-706.

5. Scott, N. A., Restenosis following implantation of bare metal coronary stents: Pathophysiology and pathways involved in the vascular response to injury. *Adv. Drug Deli. Rev.* 2006, 58, 358-376.

6. Dotter, C. T., Transluminally-placed coilspring endarterial tube grafts - Long-term patency in canine popliteal artery. *Invest. Radiol.* 1969, 4, 329.

7. Gruentzig, A. R.; Myler, R. K.; Hanna, E. S.; Turine, M. I., Coronary transluminal angioplasty. *Circulation* 1977, 56, 84.

8. Komatsu, R.; Ueda, M.; Naruko, T.; Kojima, A.; Becker, A. E., Neointimal tissue response at sites of coronary stenting in humans: macroscopic, histological, and immunohistochemical analyses. *Circulation* 1998, 98, 224-233.

9. Farb, A.; Sangiorgi, G.; Carter, A. J.; Walley, V. M.; Edwards, W. D.; Schwartz, R. S.; Virmani, R., Pathology of acute and chronic coronary stenting in humans. *Circulation* 1999, 99, 44-52.

10. van Beusekom, H. M.; van der Giessen, W. J.; van Suylen, R.; Bos, E.; Bosman, F. T.; Serruys, P. W., Histology after stenting of human saphenous vein bypass grafts: observations from surgically excised grafts 3 to 320 days after stent implantation. *J. Amer. Coll. Cardiol.* 1993, 21, 45-54.

11. http://www.fda.gov/cdrh/news/091406.html, 2008

12. Windecker, S.; Juni, P., Safety of drug-eluting stents. *Nat. Clin. Prac. Cardio. Med.* 2008, 5, 316-328.

13. Kukreja, N.; Onuma, Y.; Daemen, J.; Serruys, P. W., The future of drug-eluting stents. *Pharma. Research* 2008, 57, 171-180.

14. Kraitzer, A.; Kloog, Y.; Zilberman, M., Approaches for prevention of restenosis. *J. Biomed. Mat. Research Part B* 2008, 85B, 583-603.

15. Chatham, H., Oxygen diffusion barrier properties of transparent oxide coatings on polymeric substrates. *Surf. Coat. Technol.* 1996, 78, 1-9.

16. Creatore, M.; Palumbo, F.; d'Agostino, R., Deposition of SiOx films from hexamethyldisiloxane/oxygen radiofrequency glow discharges: process optimization by plasma diagnostics. *Plasmas and Polymers* 2002, 7, 291-310.

17. da Silva Sobrinho, A. S.; Latreche, M.; Czeremuszkin, G.; Klemberg-Sapieha, J. E.; Wertheimer, M. R., Transparent barrier coatings on polyethylene terephthalate by single- and dual-frequency plasma-enhanced chemical vapor deposition. *J. Vac. Sci. Technol. A* 1998, 16, 3190-3198.

18. Erlat, A. G.; Spontak, R. J.; Clarke, R. P.; Robinson, T. C.; Haaland, P. D.; Tropsha, Y.; Harvey, N. G.; Vogler, E. A., SiOx gas barrier coatings on polymer substrates: Morphology and gas transport considerations. *J. Phys. Chem. B* 1999, 103, 6047-6055.

19. da Silva Sobrinho, A. S.; Czeremuszkin, G.; Latreche, M.; Wertheimer, M. R., Study of defect numbers and distributions in PECVD SiO2 transparent barrier coatings on PET. *Proc. Mater. Res. Soc. Symp.* 1999, 544, 245-250.

20. da Silva Sobrinho, A. S.; Czeremuszkin, G.; Latreche, M.; Wertheimer, M. R., Defect-permeation correlation for ultrathin transparent barrier coatings on polymers. *J. Vac. Sci. Technol. A* 2000, 18, 149-157.

21. Sanchez-Urrutia, M.; Schreiber, H. P.; Wertheimer, M. R., Plasma deposition of copolymers and their permeation characteristics. *J. Appl. Polym. Sci.: Appl. Polym. Symp.* 1988, 42, 305.

CHAPTER 2

BACKGROUND

2.1 Plasmas or Glow Discharges

A plasma, which is commonly referred to as the fourth state of matter, consists of a collection of ions, radicals and free electrons. Although plasmas can be generated in a variety of ways[1-3] by applying thermal energy, photons, or electric fields of different frequencies to a volume of gas, we will consider only the case where plasma generation is achieved by application of a high frequency voltage to a gas that exists between two electrodes. A characteristic glow is observed primarily as a result of emission from excited-state chemical species formed in the gas volume by electron collisions. Degree of ionization is very small, with only one charged particle for every 100,000 to one million neutral species. Collisions between larger, slower neutral species and lighter, more mobile free electrons that respond rapidly to the applied electric field, create a net positive charge within the plasma body, and negatively charged surfaces in contact with this ionized gas. Energy transfer through elastic or inelastic collisions is dependent upon the nature of the gas discharge. Elastic collisions are the dominant form of energy exchange in noble gas discharges while inelastic collisions are prevalent in molecular gas discharges. Repetition of the collision process leads to additional free electrons and a self-sustaining plasma environment where a steady state is reached between generation and recombination of plasma species. Number density of electrons in the plasma bulk ranges from 10^9-10^{12} cm^{-3} depending upon the power, pressure, and specific gas utilized. Below ~10^9 cm^{-3}, the electrostatic force is weak enough to allow charge separation over large distances. Diffusion of free electrons to the sidewalls is too rapid and the plasma body loses the primary species responsible for collisions. Thus the plasma, and glow,

extinguishes. Electron densities greater then ~10^{12} cm^{-3} create high currents, significant gas heating and plasma instability. Because electrons are much lighter than neutral chemical species, energy transfer during collisions is inefficient; therefore, the electrons are able to attain velocities corresponding to high temperatures equivalent to thousands of degrees above thermal gas temperature. This is advantageous because reactions requiring significant activation energy can be facilitated in a low temperature neutral gas.

Mobility of plasma species is important in establishing charge distribution within the reactive environment. Free electrons diffuse and drift to reactor chamber walls and electrodes much more rapidly than do larger, less mobile ions. This charge depletion of the central glow region results in a net positive plasma body, with net negative charge on surfaces such as chamber walls and electrodes. A thin sheath, or charge imbalance layer, on the order of a Debye length, separates the plasma bulk from the boundary surfaces. An electric field therefore exists across the sheath region and positive ions from the plasma bulk are accelerated toward the negatively charged surfaces at near normal incidence.

2.1.1 Plasma Characteristics

2.1.1.1 Electron Energy

Material processing for film formation (or etching) is typically carried out in non-equilibrium plasmas where energies of ions and neutrals are significantly less than the energy of free electrons.[4, 5] This is referred to as a "cold" plasma and is also characterized by low discharge pressures and degrees of ionization. In cold plasmas, thermal conduction in a gas is much higher compared with neutral/electron collisions ($T_{ions} \approx T_{neutrals}$). Collisions between neutrals and electrons result in poor energy transfer because the mass of electrons is very low compared to the mass of ions and neutrals. Under an applied electric field, only charged particles are directly affected by the input of

external energy. In RF plasmas, most of the input power is coupled to the electrons because of their ability to respond rapidly to the applied field. Average energy, ε, of any species, *i*, in a plasma can be described by,

$$\varepsilon_i = \frac{3}{2} kT_i \qquad (2.1)$$

where *k* is the Boltzmann constant and equals 8.62×10^{-5} eV K^{-1}. Figure 2.1 shows how the electron energy distribution function ($f(\varepsilon)$), which is generally assumed to be approximately Maxwellian in shape, shifts as a function of average electron energy. Only those electrons in the high energy tail of $f(\varepsilon)$ that overlap with the reaction cross-section function, $\sigma(\varepsilon)$, have sufficient energy to cause ionization; however, the average electron energy is similar to many chemical bond energies and thereby can cause molecular dissociation.

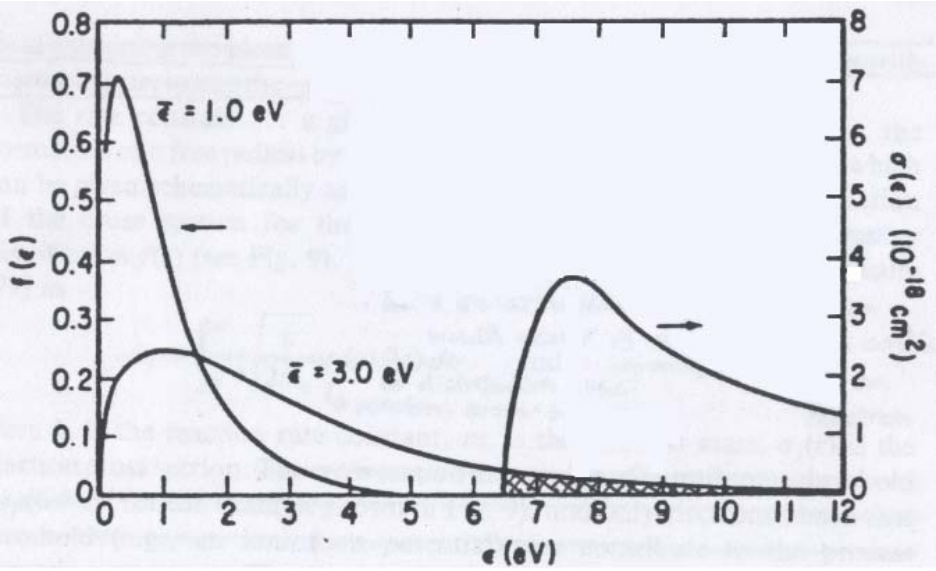

Figure 2.1. Effect of average electron energy, $\bar{\varepsilon}$, on electron energy distribution, $f(\varepsilon)$, compared to a reaction cross-section, $\sigma(\varepsilon)$[6]

2.1.1.2 Vapor-Phase Collisions

Within a plasma environment, both elastic and inelastic collisions contribute to the generation of reactive species.[7] Elastic collisions occur when particles collide without dissociating or absorbing energy into internal states while in inelastic collisions, the interacting species are promoted into excited states and/or dissociate or ionize. As stated earlier, elastic collisions are more important in noble gas discharges while inelastic collisions are dominant in molecular gas discharges. This occurs because the first ionization potential of noble gases (e.g. Argon: 15.76 eV) is higher than the average electron energy which ranges from 1-10 eV. As a result, few ionizations occur because only electrons in the high energy tail of the distribution have sufficient energy to cause ionization. Electron collisions with molecular precursors involve bond breaking and are mostly inelastic because of lower lying excited state levels and bond energies closer to the average electron energy (Fig. 2.1). As a result, electrons lose a larger portion of their kinetic energy through inelastic excitation and dissociative collisions than through elastic collisions.[8] Molecular gases have vibrational and rotational modes that can be excited by low energy electrons, thereby increasing the probability of energy transfer.

2.1.1.3 Governing Reactions in Plasmas

The production of chemical species within a plasma is governed by electron energy, and in turn, number and frequency of inelastic collisions. Although ions, electrons and radicals are continuously created and consumed by parallel reaction paths, the generation of free electrons is critical to sustain the plasma. The following are generic reaction types that represent the generation of chemical species in the vapor phase of a plasma discharge for a diatomic gas.[8]

- Ion and electron formation:

$$e^- + A_2 \rightarrow A_2^+ + 2e^- \qquad (2.2)$$

- Atom and radical formation:

$$e^- + A_2 \rightarrow 2A + e^- \quad (2.3)$$

- Heat and photon generation:

$$e^- + A_2 \rightarrow A_2^* + e^- \quad (2.4)$$

$$A_2^* \rightarrow A_2 + h\nu \quad (2.5)$$

$$e^- + A \rightarrow A^* + e^- \quad (2.6)$$

$$A^* \rightarrow A + h\nu \quad (2.7)$$

where, A_2^* and A^* are excited states of A_2 and A, respectively. For this relatively simple system, equation (Eqn. 2.2) is the primary free electron generation ionization reaction and equation (Eqn. 2.3) produces atomic species of the gas. Electronic excitation is described by equations (Eqn. 2.4) and (Eqn. 2.6) while optical emission responsible for the plasma glow is indicated in equations (Eqn. 2.5) and (Eqn. 2.7).[8]

2.1.1.4 Sheath Region

The sheath region is an electrical boundary layer that is created as free electrons diffuse or drift to the sidewalls, leaving a net positive plasma body. The applied voltage into the system is concentrated across this sheath, creating an electric field and an area of low charge density. Whereas the movement of chemical species in the main body of the plasma is primarily controlled by diffusion, movement of charged species within the sheath is directional, with the energies controlled by electric field, mobility and collisions.[9] Ion current through the sheath may be described by kinetic theory,

$$\bar{j} = \frac{\bar{n}}{4}\sqrt{\frac{8kT}{\pi m_i}} \quad (2.8)$$

if evaluated at the plasma-sheath boundary because mass balances dictate that all ions entering the electric field region are accelerated toward the electrode or wall. In equation 2.8, m_i is the mass of the gas molecules. Thermal flux of electrons is far greater than that of ions or neutrals ($j_e >> j_i, j_n$) because $T_e >> T_i, T_n$ and $m_e << m_i, m_n$. For insulating

materials, negative charge accumulates until the charge build-up at the surface reduces the electron flux to the same level as the ion flux on alternate half-cycles for high frequencies.[8] At this point the surface is at the floating potential for a specific gas and plasma condition. Surfaces experience continual bombardment of electrons by diffusion transport of high energy electrons (in the tail of the distribution) from the body. Ions are far less mobile than electrons when accelerating toward an insulating surface and their movement on a single RF half-cycle is negligible relative to that of electrons. However, because electrons are repelled by the sheath field, the sheath region is ion-rich with a net positive charge. These ions bombard the electrode surface with an energy determined by the potential drop across the sheath and by the number of collisions during transit.[8]

2.1.2 Reactor Systems

Deposition systems are available in a variety of configurations and are classified according to load capacity (single versus batch reactors), substrate position relative to the plasma (direct contact versus downstream), pressure regime, electrode geometry and generator frequency (i.e. power source). For the purposes of this study, discussion will be limited to parallel plate reactors. In this configuration, substrates are placed within the glow discharge region atop the bottom electrode, which may be either powered or grounded and may be of different area than the top electrode. Previous work[10, 11] describes the relationship between voltage distribution between the two electrodes as a function of electrode areas. Planar reactors have the advantage of controllable substrate temperatures and flexibility in monomer introduction (e.g. perforated "shower head" gas feed or entry from one side of reaction chamber). As the demand for shorter processing times, higher throughput and wafer-to-wafer reproducibility and uniformity have increased, variations of the parallel plate reactor have been introduced. The hexode reactor was created as a multiple wafer system designed by increasing electrode surface area to allow additional sample loading.[8, 12] Another major limitation is the lack of

independent control between ion energy and flux. To address this issue, the triode reactor was built with a perforated "electrode" positioned in between the powered and grounded electrodes to decouple power required to sustain the plasma and power needed to accelerate ions.[13] In addition to parallel plate systems, other reactor configurations have also been used etch/deposit thin films. These include: barrel reactors (etch only), downstream plasma reactors (glow discharge positioned upstream from substrates), and high density plasma reactors (e.g. electron cyclotron resonance, helicon).[12, 13]

2.1.3 Plasma Polymerization

Plasma polymerization[7, 14] is a specific type of plasma-enhanced deposition and involves reaction of carbon-based chemical species (ions, radicals, etc.) in both the plasma body and at surfaces where films are formed. Reactions in the vapor phase frequently result in powder formation and are dependent upon mean free paths and energies of the colliding reactants. Powders refer to vapor phase agglomerates which form more readily at higher operating pressures and power inputs due to enhanced collision rates and energetics. Film growth depends upon the reactive species flux and energy inputs to a surface via intentional heating and from impact of positive ions accelerated into the surface. Ion bombardment energy is a function of operating pressure and input power; species adsorption, desorption, and chemical reaction rates on the surface are affected by ion bombardment and by substrate temperature. As films are grown, ions strike the substrate thereby breaking surface bonds and forming "activated sites", where surface reactions are induced by either conformational rearrangement of dangling surface chains or by deposition of additional polymeric layers.

The term "plasma polymer" is a misnomer because deposited structures lack the repeat unit of conventional polymers.[15] However, these materials are crosslinked during the deposition process, are pinhole-free and homogeneous, have excellent adhesion to a variety of substrates and other films, have tunable chemical and mechanical stabilities

and do not require the use of crosslinking agents and/or solvents during synthesis. Control of plasma polymer thin film properties is well-investigated and many parameters contribute to physical and chemical characteristics such as crosslink density and morphology. For instance, these characteristics depend upon: the selection of monomer and flow rate,[16] power and excitation frequency,[17, 18] pressure,[19] substrate temperature[20, 21] and chamber geometry.[22]. Specific parameters that have particular importance to this thesis will be described below.

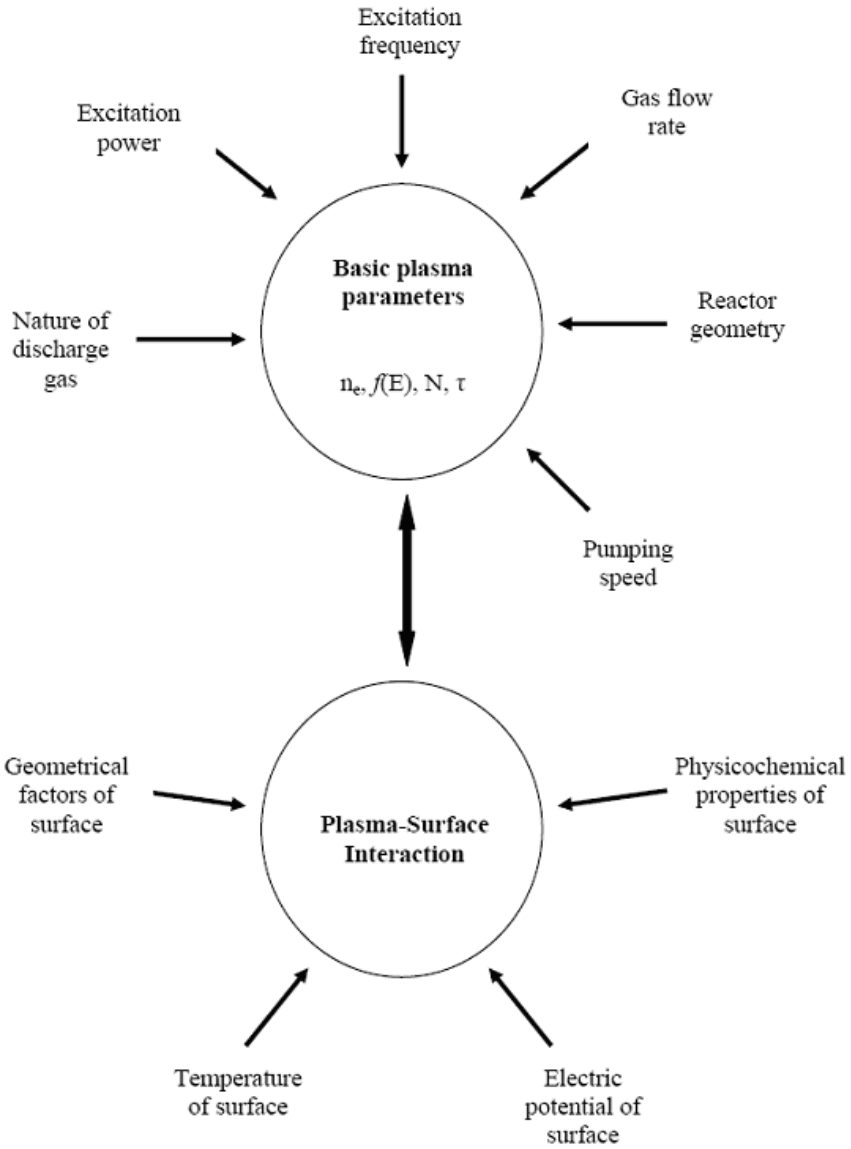

Figure 2.2. Relationship between basic plasma parameters and plasma process conditions[15]

2.1.3.1 Choice of Monomer and Flow Rate

A wide variety of different monomer types have been used in plasma polymerization processes. Indeed, a major advantage of using plasmas to deposit polymeric films is that precursors do not require polymerizable functional groups. Rather, reactive ions and neutrals are created in the vapor phase, drift or diffuse through the sheath region and react/recombine on the surface. Examples of non-polar monomers are hydrocarbons, which have been divided into three subclasses: triple-bond containing structures, double bond containing and cyclic structures and saturated monomers.[16] For compounds with similar molecular weights and deposition conditions, each of the three differ in deposition rates. Energies of carbon-carbon bonds (C–C: ~3.60 eV; C=C: ~6.40 eV; C≡C: ~8.70 eV) do not influence deposition rates as much as does the potential for electron generation in bond breaking collisions because electron energy distributions have their maxima between 1 and 10 eV (Fig. 2.1). Larger concentrations of free electrons yield more collisions and thus higher rates of reactive species generation.

Hydrocarbons containing polar groups yield films with a higher degree of hydrophilicity than those deposited using non-polar hydrocarbons. Previous studies[23] have used x-ray photoelectron spectroscopy and contact angle measurements to characterize differences in atomic percent, carbon-oxygen ratio and hydrophilic nature of polyethylene glycol (PEG) – like plasma polymerized films using various starting precursor molecules. Vinyl pyridine[24, 25] and allyl amine[26] are examples of polar monomers used in plasma processes for fabrication of new surfaces with controlled chemistries. Plasma polymerization of vinyl pyridine has been used as a surface modification technique in an effort to promote adhesion of polyimide surfaces to copper metal.[25] Allyl amine co-polymerizations[26] have been used to spacially control surface functionality of octadiene polymers as biomaterials. In contrast, fluorocarbon[27] plasma chemistry has been widely studied in the microelectronics industry both due to deposition

of protective hydrophobic layers and as a source of etchant species for the patterning and removal of silicon and silicon-containing films. By changing process conditions, it is possible to perform net etching or deposition of materials, although both processes occur simultaneously because etchant (F) and deposition precursors (e.g., CF_2) are generated in fluorocarbon-based plasmas.[28, 29]

Rate of precursor introduction is an important parameter in determination of film deposition rate. In the low flow rate regime, the deposition rate initially experiences a sharp increase with flow rate since deposition is limited by the concentration of gas available ("monomer-deficient region"). Of course, such results assume that the residence time is sufficient to consume all the monomer. As flow rates increase, deposition rate eventually decreases because of decreasing residence time of the monomer within the plasma region. This is labeled the "energy-deficient region" because at low residence times, there is a reduced probability of electron collisions which leads to a limited amount of energy transfer.

2.1.3.2 Power Source and Excitation Frequency

Power sources used for plasma polymerization utilize either direct current (DC) or alternating current (AC) discharges,[18] although there are numerous mechanisms by which the discharge can be sustained.[30] The mechanism for energy transfer from the sheath electric field to electrons is dependent on frequency of the activating field. For DC discharges, bombardment of the cathode with positive ions create secondary electrons which are accelerated away from the cathode due to the field direction. As they accelerate into the bulk plasma, additional ions and free electrons are generated from inelastic collisions. Since DC glow discharges have not been used in this work due to surface charging during deposition of the insulating films, no further consideration of these plasmas will be offered. Rather, the work described in this thesis used an RF

discharge at a frequency of 13.56 MHz, which is more amenable to insulating film deposition as described below.

In an AC discharge, the dominant mechanism of ion and electron generation depends on the frequency. At lower frequencies (i.e. 60 Hz), the effect is similar to that of a DC discharge at alternating polarity. As frequency is increased, bulky, high molecular weight ions are unable to follow changes in field polarity. At frequencies greater than 500 kHz, switching of electrode polarity is too fast to allow complete sweeping of ions to the electrodes on a half cycle. Ions within the plasma are stagnant relative to free electrons and as a result, there is a significant reduction in the loss of charged ions to surfaces relative to electron loss. Because electrons can follow the alternating field, they continuously gain energy from the applied field, and can undergo elastic collisions, which may increase their total energy. After the electron has accrued a sufficient amount of energy, inelastic collisions initiate bond breaking and additional reactive species are created. Electrons close to the electrode surface will be withdrawn from the plasma body at each positive half of the switching cycle, imparting a net negative charge to the electrode and thus the driving force for positive ion bombardment. The mechanism described here is generally applied for many types of AC discharges, including microwave and RF. Deposition rates of thin films are typically enhanced[31, 32] at microwave frequencies because of a relatively larger population of electrons in the high energy tail of the energy distribution curve. An example of this is seen in figure 2.1, where average electron energy for microwave plasmas is 3.0 eV versus 1.0 eV for RF discharges. Higher average electron energy leads to enhanced inelastic collisions, a higher rate of ion formation and higher ion bombardment flux.[15]

2.1.3.3 Geometrical Factors

The location of substrates within the deposition chamber is another important consideration in establishing film properties. Position of the sample is relative to the

entry location of the monomer and to either coils or plates which supply the electric field and thus initiate the plasma. For capacitively-coupled reactors, RF power is coupled to the gas using a blocking capacitor. In such parallel-plate reactors, film properties are generally uniform across the surface, although differences may be observed along the z-axis due to increases in volume power density. As electrodes are positioned closer together, the electric field in the sheath region increases in strength and ions impinge on the substrate surface with a higher bombardment energy. Changes in film response can be linked to film chemistry, which is altered by the distance between electrodes. This can especially be observed for fluorinated polymers due to the dependence of film properties on fluorine content.[27] For inductively-coupled discharges in tube reactors, it has been reported[33] that fluorine concentration in films from a tetrafluoroethylene (TFE) discharge varies depending on the placement of samples either upstream (fluorine-rich) or downstream (fluorine-poor) from monomer introduction. This occurs because as the gas flows through the plasma region beneath the coil (and over the sample), generation and recombination rates and thus concentration gradients vary as a function of position of substrates relative to the plasma region, which results in variation of ion concentrations and bombardment energies.

2.2 Hydrogels

Hydrogels are three-dimensional chemically-crosslinked polymeric networks capable of incorporating large amounts of water. The presence of crosslinks provides the network structure and physical integrity that allow the matrix to swell in aqueous media.[34] Hydrogels are versatile in nature and can be classified as neutral or ionic based on the chemistry of their side groups, affine or phantom networks based on their mechanical and structural properties and may be synthesized as amorphous, semi-crystalline or supermolecular structures.[35-37] Choice of monomer is an important parameter that establishes the chemical moieties present along the backbone of the

polymer; this is essential in understanding potential applications where the polymer may be useful, e.g., for drug delivery applications. Hydrogels have been used as carriers of drug molecules for delivery to sites in the gastrointestinal tract, colon, nose, etc.[38] Recently, drug-eluting stents have garnered much attention as a means to address coronary artery disease. Poly(amido amine),[39] PEG-alginate,[40] and magnetic-gelatin[41] based hydrogels have been studied for this purpose. A partial list of monomers used in the synthesis of hydrogels for pharmaceutical applications includes ethylene glycol, PEG acrylate, PEG methacrylate, PEG diacrylate, PEG dimethacrylate, and ethylene glycol dimethacrylate.[42]

The suitability of a hydrogel for a particular application, and specifically, drug delivery, depends on its network structure or bulk properties. The three most important parameters governing hydrogel structure are: polymer volume fraction in the swollen state, v_S, average molecular weight of polymer chains in between adjacent crosslinks, M_C, and mesh size, ξ. All three properties have been correlated with the common goal of identifying the amount and size of drug molecules that the hydrogel is able to incorporate. Polymer volume fraction is a numerical indication of the amount of fluid the hydrogel is able to intake and retain. The molecular weight between two consecutive crosslinks is a measure of material crosslink density and directly affects the void space available for drug molecule penetration, either through diffusion or forced entry. Reviews on the subject have focused on bulk properties of hydrogels synthesized by solution polymerization methods.[34, 43, 44]

Because of its ability to hydrate and its nontoxic and biocompatible characteristics, polyethylene glycol, or PEG, has been extensively studied[45, 46] as a biomaterial and has many applications in tissue engineering[47, 48] and drug delivery.[42, 49-53] Thin films of PEG-based hydrogels are of particular interest for their ability to function as drug delivery reservoirs and anti-fouling surfaces.[54-58] One common method to form chemically-crosslinked PEG hydrogel thin films is by using end-functional macromers.

Polymerization reactions are initiated between endgroups on different molecules and propagate through an entire polymer assembly to form a continuous, crosslinked network. Previous studies have utilized acrylate,[51, 59, 60] cinnamylidene acetate,[61] and nitrocinnamate[62] termination ends. Ultraviolet (UV) light has also been used[63] to initiate polymerization between free radicals on reactive PEG endgroups. Crosslink density and mesh size are controlled by the wavelength of light used and radiation dose. Other sources of radiation, including gamma rays[64] and electron beams,[65-67] do not require the use of a photoinitiator but rather use the high intensity radiation to create reactive free radicals by elimination of hydrogen atoms from PEG and thereby promote formation of carbon-carbon linkages. There also have been many creative attempts to to attach PEG molecules onto a surface. These include physical adsorption,[68] addition of PEO molecules to backbones of block copolymers,[69] surface grafting,[70] covalent chemical derivatization,[71] self-assembled monolayers[72] and synthesis of polymeric matrices incorporated with PEO molecules.[73]

The term 'biomaterial' may defined as a synthetic material for medical applications. For a biomaterial to successfully perform its intended function, it must be engineered with design specifications for permeability, biodegradability, strength and flexibility. Another concern is whether the material will induce adverse responses when in contact with physiological systems. Biocompatibility can be described as the ability of a material to limit inflammation or foreign body response of soft tissue or bone. Factors that may lead to negative responses from the body include: elution of low molecular weight species from the implant, movement of implant, geometry and bacterial infection.[74] The body will respond to these foreign materials with varying degrees of intensity.

Plasma deposition is an attractive alternative to traditional crosslinking recipes (described above) for those applications that require tightly controlled thickness, good adhesion and defect-free structures. Plasma-initiated reactions also allows creation of

new biomaterials and improvements to existing medical device technology. One major advantage of plasma processes is the conformal nature of deposition. Complex geometric shapes can be coated because transport of species in a plasma environment is a combination of molecular and convective diffusion.[74] Due to vapor phase collisions and high bombardment energies of ions impinging on the surface, plasma polymerized films are crosslinked during deposition, resulting in dense and pinhole-free layers. This suggests possible application as barrier and protective films.[75, 76] High energy bombardment of ions also promotes adhesion[77] to a variety of substrates including: metals, ceramics, semiconductors and paper. Grafting or surface modification is dependent on the chemical nature and functionalization of the substrate. A list of various advantages offered by plasma polymerization is given in table 2.1.

Table 2.1. Advantages of plasma deposited films.[74]

- Conformal.
- Pinhole free.
- Can be coated on unique substrates: Metals, glasses, polymers, ceramics, paper, etc.
- Good adhesion to substrates.
- Unique film chemistries can be achieved.
- Serve as excellent permeation barriers.
- Show low levels of leachables.
- Relatively easy to prepare.
- A well-developed technology for performing these depositions already exists.
- Can be characterized.
- Plasma-deposited layers are sterile upon preparation.

Plasma polymerization of polyethylene glycol-like films has been investigated extensively in attempts to generate anti-fouling surface layers.[23, 54, 56-58, 78-85] It has been shown[23] that PEG-like surfaces can be deposited from many different starting monomers. For instance, a detailed comparison was conducted between oligoglyme, crown ether, and dioxane precursors. Results indicated that the oligoglyme-polymerized films consist of randomly-branched, methyl-terminated chains of —(CH_2CH_2O)— repeat units and lack hydroxyl groups. Films polymerized from higher molecular weight precursors contain longer fragments of the intact monomer, suggesting looser crosslinked coatings.[23] Small percentages of carbon double bonded to oxygen were also detected. The outer surface of crown ether films consist of intact cyclic structures while dioxane films possess hydroxyl groups bound to an unsaturated hydrocarbonaceous matrix and ether carbon-bearing precursor fragments.[23]

Synthetic coatings of plasma-polymerized PEG-like films may be appropriate for application in a variety of commercial sectors, including the food processing industry. Recently,[54] plasma polymerization of 12-crown-4-ether and tri(ethylene glycol) dimethyl ether was used to deposit films onto stainless steel surfaces to assess their ability to reduce biofilm formation. The PEG-like films were more hydrophilic and had lower surface roughness values compared to those of unmodified substrates.[54] The coatings displayed resistance to *salmonella typhimurium,* a common food-borne pathogen; *staphylococcus epidermidis,* a bacterium that causes biomaterial infection; and *pseudomonas fluorescens,* a food spoilage bacterium. Anti-fouling properties may also be used in bio-MEMS (micro electromechanical system) devices. In previous studies,[79] standard photolithographic techniques were used to pattern plasma polymerized PEG-like films synthesized using tetra(ethylene glycol) dimethyl ether monomers. The authors used the patterned films for (1), micro-patterning of cell culture devices and (2), as a protective layer for electrodes in electrochemical sensing. Micro-patterning of cell cultures is used to investigate cellular activity and cell development and may be

incorporated as part of more complex structures such as micro-electrode arrays,[86] microchannels, or micro-analyzers. The ability of a hydrogel coating to absorb water ensures that the material shows elevated conductivity and thus may be important for sensing applications in the presence of biological molecules.[79] More common, however, is the use of PEG-like surfaces for biomedical devices.[40, 87, 88] One of the main sources of inflammation or foreign body reaction is the interaction of an implanted biomaterial with proteins in physiological systems. Upon insertion into the body, proteins such as fibrinogen and fibronectin adsorb onto the biomaterial surface. This facilitates interaction between the biomaterial and monocyte-derived macrophages. Monocytes are specific white blood cells that enable macrophage cells to release surface and structurally damaging agents that interact with the biomaterial. This leads to degradation and inflammation. Alternatively, the device may become encapsulated by the fibrous tissue. To prevent this chain of events, materials using plasma polymerized PEG-like coatings have been investigated to minimize protein-biomaterial interaction.[56-58]

2.3 Possible Applications

2.3.1 Drug-Eluting Stents

A stent is a metallic mesh tube used to reopen a clogged artery during angioplasty. The stent is collapsed over a balloon catheter as it is positioned into the area of the blockage. As the balloon inflates, the stent expands and locks into place along the artery endothelium, thus allowing improved blood flow to the heart. Over time, however, arteries will begin to reclose in a sequence of cellular and molecular events; this process is called restenosis and is outlined in figure 2.3.

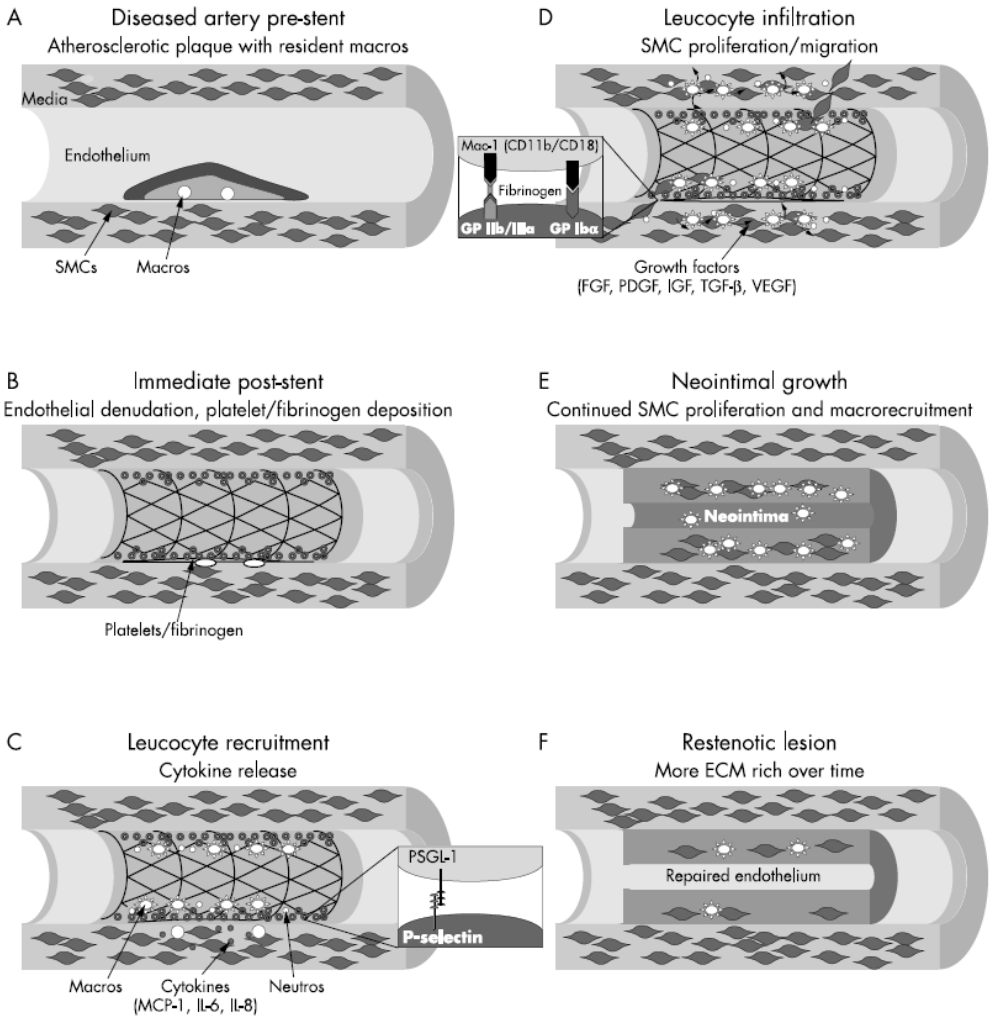

Figure 2.3. (A) Mature atherosclerotic plaque before inserting stent, (B) Immediate result of stent placement with endothelial denudation and platelet and fibrinogen deposition, (C and D) Leucocyte recruitment, infiltration, and SMC proliferation and migration in the days after insertion, (E) Neointimal thickening in the weeks after insertion, with continued SMC proliferation and monocyte recruitment, (F) Long term (weeks to months) change from a predominantly cellular to a less cellular and more extracellular matrix rich plaque.[89]

In order to delay the restenosis process, bare metal stents have been coated with thin polymer films to serve as reservoirs for drug molecules. Although DES technology is still in its infancy, recent advances have been chronicled in many reviews.[69-72] Improvements in coatings for drug-eluting stents have resulted in restenosis occurances to fall from approximately thirty percent to below ten percent.[90] The design of a polymer matrix for stent applications requires the detailed understanding of several issues,

including: stability, biocompatibility, drug elution rate, compatibility with drug, biodegradation kinetics/products, etc.

To date, many different types of polymer films have been investigated to determine their interactions with paclitaxel or sirolimus, drug molecules approved for use in clinical trials.[91] Among the polymer coatings tested were: poly(lactide-co-Σ-caprolactone),[92] chondroitin sulfate and gelatin,[93] and phosphorylcholine-based materials.[94, 95] In the study using poly(lactide-co-Σ-caprolactone), stents were inserted in diseased rabbit arteries. Paclitaxel (200 μg/stent) was released as the film degraded over time, with complete delivery occurring two months after insertion. Six months after implantation, no significant intimal thickening or inflammatory responses were detected. It was determined that either (1), a two month delivery period of paclitaxel is sufficiently long to prevent the re-growth of neointima, or (2), the drug remains present and active within the artery endothelium long after delivery from the stent.[92]

Chondroitin sulfate and gelatin (CSG) films were also tested as drug reservoirs for delivery of paclitaxel in rabbit arteries.[93] CSG-coated stents were loaded with paclitaxel at varying doses (approximately 42, 20, 8.5 and 1.5 μg/stent) and percent reduction of neointimal thickness was measured and compared with control CSG-coated stents without paclitaxel as well as the uncoated metallic stents. Results showed[93] that only at the higher dosages, 42 and 20 μg, does the neointima thickness reduce significantly. The 42 μg loaded stent produced a 49% and 48% reduction in neointimal thickness versus the CSG-coated stents without paclitaxel and the uncoated metallic stents, respectively. The 20 μg loaded stent produced a 36% and 35% reduction in neointimal thickness compared with the CSG-coated stents without paclitaxel and the uncoated metallic stents, respectively. However, after one month of activity, the lack of complete healing suggests persistent deposition of platelet cells and fibrinogen proteins; inflammation was also detected at damage sites. Contrasting results between different systems shows the importance of reservoir media, and their role in the release behaviour of drug molecules

(200 μg/2 months for poly(lactide-co-Σ-caprolactone) vs. 42 or 20 μg/ 1 month for CSG) and occurrence of inflammatory reactions. Artery inflammation is determined by the polymer film chemistry while release rates are a function of film degradability, mesh size and drug-polymer interaction.

Interactions between drug and polymer have been investigated for phosphorylcholine (PC)-based materials. For the PC-based films characterized in previous studies,[94] loading capacity was investigated as a function of drug molecular weight. Higher crosslinked PC films with smaller interstitial spacings are only able to support drugs of lower molecular weight up to 1200 Daltons, well within the range of paclitaxel (~850 Da) and sirolimus (~910 Da). In general, hydrophilic drugs are able to elute more rapidly than their hydrophobic counterparts because of drug interactions with hydrophobic domains in the polymer matrix.[94] The researchers considered release to be complete when less than ten percent of the drug remained on the stent. Release profiles of different drugs were correlated with the oil-water partition coefficient of the compounds, which is an indirect determinant of hydrophobicity and a measure of molecular structure.

The use of hydrogels in stent applications is seen as a promising alternative to the conventional polymers that have been tested as drug delivery reservoirs because of their ability to supply improved control of molecule release behavior. One class that has been extensively studied is thermoresponsive co-polymer hydrogel-based systems.[96] Thermoresponsive polymers are part of a family of stimuli-responsive hydrogels that change physical properties as a function of temperature. These hydrogels experience a phase transition between an open-pore, swelled, hydrophilic state and a closed-pore, collapsed, hydrophobic state. In the swelled state, hydrogen-bonding interactions dominate and water molecules are able to enter the matrix while in the collapsed state, hydrophobic interactions increase, leading to a decrease in water solubility. The temperature at which this occurs is called the lower critical solution temperature (LCST);

above this point, the hydrogel is considered hydrophobic and below this temperature it is hydrophilic. As a drug delivery vehicle, probably the most well-characterized systems are poly(*N*-isopropylacrylamide) (pNiPAAm) and its derivatives.[96] Previous investigations[97] have studied the release behavior of heparin (hydrophilic) from both hydrophilic-biased (i.e. pNiPAAm/acrylic acid co-polymer) and hydrophobic-biased (i.e. pNiPAAm/butyl methacrylate co-polymer) hydrogel networks. The delayed release from the hydrophobic-biased hydrogel extended the delivery lifetime and was correlated to hydrogel swelling kinetics. Manipulation of hydrogel LCST has also been examined[98, 99] by introducing various levels of hydrophobic character in pNiPAAm/NtBAAm (N-*tert*-butylacrylamide). When tested with colchicine, a small, hydrophobic drug surrogate, release rates were inversely proportional to NtBAAm monomer present within the co-polymer.[99]

Polyethylene glycol (PEG)-based films have also garnered recent interest in coronary stent applications.[40] The role of PEG in PEG-alginate hydrogel composite films was investigated and it was reported that addition of PEG increases the compliance and physical strength of the film relative to pure alginate, which has a higher tensile strength than pure PEG by 1-2 orders of magnitude. By reducing the overall coating stiffness PEG acts as a plasticizer[40] and increases film stability in physiological systems, especially in areas not supported by the stent. The addition of PEG did not significantly alter PEG-alginate swelling properties, which exhibited swelling ratios of close to one before and after hydration (i.e. unchanged thicknesses). Instead, release of paclitaxel in buffer solution was controlled by film degradation which was a function of ion concentrations.[40] PEG derivative films have recently been investigated as shape-memory materials for their ability to exercise control over the thermomechanical response of the stent device.[87] The time necessary for full shape recovery is dependent on polymer glass transition temperature (T_G), crosslink density, and deformation, or storage, temperature (T_D). Experiments were conducted with *tert*-butyl acrylate and poly(ethylene glycol)

dimethacrylate films crosslinked between 10-40%. The different crosslinked coatings have similar T_G (50-55°C) but exhibit significantly different rubbery modulus (10%: 1.5 MPa; 20%: 5.6 MPa; 40%: 11.5 MPa). This difference in rubbery modulus accounted for differences in recovery times, with the 40% crosslinked films reverting to its original shape the fastest.[87] Novel PEG-based systems are also being developed as biomaterials for ureteral stents.[88]

2.3.2 Barrier Films

Thin film barrier technology has been of interest since the mid-1970's. Barrier properties are dependent on the permeability of the polymer and the thickness of the film. Ultrathin layers of conventional polymers generally have a limited barrier protection, especially in cases where the penetrant is small, i.e. NO_2, H_2O, O_2, etc.[100] Plasma polymerized thin films have been found useful when, (1) the thickness of the coating must be limited for application purposes (i.e. magnetic disks), (2) a thin "capping" layer is required over traditional polymers to improve overall protection quality and (3) corrosive resistance is needed.[100] Two important considerations in identifying appropriate films are adhesion to a substrate and bulk properties of the protective layer. Plasma polymers have excellent adhesion to various substrates including metals, glasses, polymers, ceramics and paper.[74] Although stability of a coating is often referenced at an air interface, the influence of water on a polymer-substrate interface is often an important factor in determining the effectiveness of a barrier. Because water penetration through the polymer matrix to the polymer-substrate interface can be rapid, conventional polymers are subject to delamination, resulting in weak mechanical stability and poor protection. Many early studies focused on engineering water vapor barriers for water-sensitive optical elements.[101 102] Moisture sensitive alkali metal halide crystalline materials in optical devices require protection against high humidity environments and

previous studies[101] have featured plasma-polymerized tetrafluoroethylene (TFE) and chlorotrifluoroethylene (CTFE) films as moisture-resistant coatings.

Bulk properties of plasma polymers are another principal concern in tuning barrier layer properties. Plasma polymers have very short segments between crosslinks and an absence of regular polymeric segments. As a result, transport models applicable for conventional polymers, whose permeability is described as the product between solubility (governed by intermolecular interactions between polymer and penetrant) and diffusivity (governed by intermolecular interactions of the polymer), are not valid for plasma polymers.[103 104] Rather, transport through many plasma polymers can be described as a combination of the solution-diffusion theory for conventional polymers and molecular sieves.[100] The growth of defects to the film bulk during the plasma deposition process can also play an important role in the effectiveness of a barrier film.[105] Previous studies of single-layer plasma-deposited SiO_2 barriers[106-108] show that transport of oxygen through the film body is due to the presence of defects and that lateral diffusion into small, closely-spaced pinholes results in a permeation rate higher than if larger defects were spaced further apart.[109 110] For the defect-driven permeation mechanism, even for high-quality single-layer barrier films, the activation energy for oxygen permeation is characteristic of diffusion through the substrate, regardless of the coating material or deposition technique.[111 108]

2.3.3 Anti-Fouling Surfaces

As has been previously stated in this chapter, plasma-polymerized films have been extensively studied as anti-fouling surfaces in biomedical applications. Specifically, it has been shown that PEG-like films from tetraethylene glycol dimethyl ether monomers can provide a non-sticky surface that prevents protein adhesion.[56 57, 58] Our work focuses on enhancing the understanding of bulk properties of plasma-deposited PEG-like films. This is in contrast to most previous studies where the intent has been the

development of methods to modify and tune the surface properties to achieve non-fouling behavior.

2.4 Scope of Thesis

In this work, one goal is to fundamentally understand how the properties of plasma-polymerized polyethylene glycol-like coatings can be altered to illicit different response behaviors in water solution. An analysis of the PEG-like film structure and chemistry is detailed in Chapter 3, with swelling and dissolution behavior discussion provided in Chapter 4. Physical properties are related to plasma deposition conditions, where operating parameters such chamber pressure, substrate temperature and input RF power are manipulated (Chapter 3). In addition, pore sizes are investigated in Chapter 5 through transport of fluorophore-labeled dendrimers with controlled size dimensions by diffusion and electrophoretic drift. Positron annihilation lifetime spectroscopy provides an additional means of quantifying the average pore size of our films. Conclusions and future work considerations are included in Chapter 6.

2.5 References

1. Abe, H.; Yoneda, M.; Fujlwara, N., Developments of plasma etching technology for fabricating semiconductor devices. *Jap. J. Appl. Phys.* **2008,** 47, 1435-1455.

2. Bondur, J. A., Dry process technology (reactive ion etching). *J. Vac. Sci. Technol.* **1976,** 13, 1023-1029.

3. Gerlach-Meyer, U.; Coburn, J. W.; Kay, E., Ion-enhanced gas-surface chemistry: The influence of the mass of the incident ion. *Surface Science* **1981,** 103, 177-188.

4. Crompton, R. W.; Sutton, D. J., Experimental investigation of the diffusion of slow electrons in nitrogen and hydrogen. *Proc. Roy. Soc. Lond. A: Math. Phys. Sci.* **1952,** 215, 467-480.

5. Crompton, R. W.; Huxley, L. G. H.; Sutton, D. J., Experimental studies of the motions of slow electrons in air with application to the ionosphere. *Proc. Roy. Soc. Lond. A: Math. Phys. Sci.* **1953,** 218, 507-519.

6. Yanagihara, K.; Yasuda, H., Plasma Polymerization of Tetrafluoroethylene. IV. Comparison of Ethylene and Tetrafluoroethylene by Measurement of Electron Temperature and Density of Positive Ions. *J. Polym. Sci., Polym. Chem. Ed.* **1982,** 20, 1833-1846.

7. Bell, A. T., Fundamentals of plasma polymerization. *J. Macromol. Sci. Chem.* **1976,** A10, 369-381.

8. Flamm, D. L.; Herb, G. K., Plasma Etching Technology - An Overview. In *Plasma Etching: An Introduction*, Manos, D. M.; Flamm, D. L., Eds. Academic Press, Inc.: San Diego, 1989.

9. Godyak, V. A.; Sternberg, N., Dynamic model of the electrode sheaths in symmetrically driven rf discharges. *Phys. Rev. A* **1990,** 42, 2299-2312.

10. Koenig, H. R.; Maissel, L. I., Application of RF discharges to sputtering. *IBM J. Res. Dev.* **1970,** 14, 168-171.

11. Coburn, J. W.; Kay, E., Positive-ion bombardment of substrates in RF diode glow-discharge sputtering. *J. Appl. Phys.* **1972,** 43, 4965-4971.

12. Reinberg, A. R., Plasma Etch Equipment and Technology. In *Plasma Etching: An Introduction*, Manos, D. M.; Flamm, D. L., Eds. Academic Press, Inc.: San Diego, 1989.

13. Mucha, J. A.; Hess, D. W.; Aydil, E. S., Plasma Etching. In *Introduction to Microlithography*, 2nd ed.; Thompson, L. F.; Willson, C. G.; Bowden, M. J., Eds. American Chemical Society: Washington D.C., 1994.

14. Yasuda, H., Glow-discharge polymerization. *J. Polym. Sci. Macromol. Revs.* **1981,** 16, 199-293.

15. Morosoff, N., An Introduction to Plasma Polymerization. In *Plasma Deposition, Treatment, and Etching of Polymers*, d'Agostino, R., Ed. Academic Press, Inc.: San Diego, 1990.

16. Yasuda, H., Formation of polymeric materials by a nonpolymerization process: Glow discharge polymerization. *Contemp. Top. Polym. Sci.* **1979,** 3, 103-123.

17. Nasser, E., *Fundamentals of Gaseous Ionization and Plasma Electronics*. Wiley: New York & London, 1971.

18. Maissel, L. I., Applications of Sputtering to the Deposition of Films. In *Handbook of Thin Film Technology*, Maissel, L. I.; Glang, R., Eds. McGraw-Hill: New York, 1970.

19. Westwood, A. R., Glow discharge polymerization. 1. Rates and mechanisms of polymer formation. *Eur. Poly. J.* **1971,** 7, 363-375.

20. Lopez, G. P.; Chilkoti, A.; Briggs, D.; Ratner, B. D., Substrate temperature effects on film chemistry in plasma deposition of organics. III. Analysis by static secondary ion mass spectrometry. *J. Polym. Sci., Polym. Chem. Ed.* **1992,** 30, 2427-2441.

21. Lopez, G. P.; Ratner, B. D., Substrate temperature effects on film chemistry in plasma depositions of organics. II. Polymerizable precursors. *J. Polym. Sci., Polym. Chem. Ed.* **1992,** 30, 2415-2425.

22. Morosoff, N., Surface Modification by Plasma Polymerization. In *Innovations in Materials Processing*, Bruggeman, G.; Weiss, V., Eds. Plenum: New York, 1985.

23. Johnston, E. E.; Bryers, J. D.; Ratner, B. D., Plasma Deposition and Surface Characterization of Oligoglyme, Dioxane, and Crown Ether Nonfouling Films. *Langmuir* **2005,** 21, 870-881.

24. Zhu, Y. Q.; Kang, E. T.; Neoh, K. G., Plasma graft copolymerization of 4-vinylpyridine on dense and porous SiLK for electroless plating of copper and for retardation of copper diffusion. *J. Electrochem. Soc.* **2005,** 152, F107-F114.

25. Wang, W. C.; Kang, E. T.; Neoh, K. G., Electroless plating of copper on polyimide films modified by plasma graft copolymerization with 4-vinylpyridine. *Appl. Surf. Sci.* **2002,** 199, 52-66.

26. Beck, A. J.; Jones, F. R.; Short, R. D., Plasma copolymerization as a route to the fabrication of new surfaces with controlled amounts of specific chemical functionality. *Polymer* **1996,** 37, 5537-5539.

27. d'Agostino, R.; Cramarossa, F.; Fracassi, F.; Illuzzi, F., Plasma Polymerization of Fluorocarbons. In *Plasma Deposition, Treatment, and Etching of Polymers*, d'Agostino, R., Ed. Academic Press, Inc.: San Diego, 1990.

28. Coburn, J. W.; Winters, H. F., Plasma etching - A discussion of mechanisms. *J. Vac. Sci. Technol.* **1979,** 16, 391-403.

29. d'Agostino, R.; Capezzuto, P.; Bruno, G.; Cramarossa, F., Mechanism of etching, polymerization and deposition in R.F. (radio frequency) discharges. *Pure & Appl. Chem.* **1985,** 57, 1287-1298.

30. Lieberman, M. A.; Gottscho, R. A., Design of High-Density Plasma Sources for Materials Processing. In *Plasma Sources for Thin Film Deposition and Etching*, Francombe, M. H.; Vossen, J. L., Eds. Academic Press, Inc.: San Diego, 1994; Vol. 18.

31. Wertheimer, M. R.; Moisan, M., Comparison of microwave and lower frequency plasmas for thin film deposition and etching. *J. Vac. Sci. Technol. A* **1985,** 3, 2643-2649.

32. Claude, R.; Moisan, M.; Wertheimer, M. R.; Zakrzewski, Z., Comparison of microwave and lower frequency discharges for plasma polymerization. *Appl. Phys. Lett.* **1987,** 50, 1797-1799.

33. Yasuda, H.; Morosoff, N.; Brandt, E. S.; Reilley, C. N., Plasma polymerization of tetrafluoroethylene. I. Inductive radio frequency discharge. *J. Appl. Polym. Sci.* **1979,** 23, 1003-1011.

34. Peppas, N. A.; Mikos, A. G., Preparation Methods and Structure of Hydrogels. In *Hydrogels in Medicine and Pharmacy*, Peppas, N. A., Ed. CRC Press: Boca Raton, 1986; Vol. 1.

35. Peppas, N. A.; Merrill, E. W., Differential scanning calorimetry of crystallized PVA hydrogels. *J. Appl. Polym. Sci.* **1976,** 20, 1457-1465.

36. Hickey, A. S.; Peppas, N. A., Mesh size and diffusive characteristics of semicrystalline poly(vinyl alcohol) membranes prepared by freezing/thawing techniques. *J. Membr. Sci.* **1995,** 107, 229-237.

37. Bell, C. L.; Peppas, N. A., Biomedical membranes from hydrogels and interpolymer complexes. *Adv. Poly. Sci.* **1995,** 122, 125-175.

38. Huang, Y.; Leobandung, W.; Foss, A.; Peppas, N. A., Molecular aspects of muco- and bioadhesion: Tethered structures and site-specific surfaces. *J. Control. Release* **2000,** 65, 63-71.

39. Jagur-Grodzinski, J., Polymers for tissue engineering, medical devices, and regenerative medicine. Concise general review of recent studies. *Polym. Adv. Technol.* **2006,** 17, 395-418.

40. Livnat, M.; Beyar, R.; Seliktar, D., Endoluminal hydrogel films made of alginate and polyethylene glycol: Physical characteristics and drug-eluting properties. *J. Biomed. Mat. Research Part A* **2005,** 75, 710-722.

41. Huang, L.-Y.; Yang, M.-C., Behaviors of controlled drug release of magnetic-gelatin hydrogel coated stainless steel for drug-eluting-stents application. *J. Magnetism Magnetic Mater.* **2007,** 310, 2874-2876.

42. Peppas, N. A.; Bures, P.; Leobandung, W.; Ichikawa, H., Hydrogels in pharmaceutical formulations. *Eur. J. Pharma. Biopharma.* **2000,** 50, 27-46.

43. am Ende, M. T.; Mikos, A. G., Diffusion-Controlled Delivery of Proteins from Hydrogels and Other Hydrophilic Systems. In *Protein Delivery: Physical Systems*, Sanders, L. M.; Hendren, R. W., Eds. Plenum Press: Tokyo, 1997.

44. Lowman, A. M.; Peppas, N. A., Hydrogels. In *Encyclopedia of Controlled Drug Delivery*, Mathiowitz, E., Ed. Wiley Publishing New York, 1999.

45. Harris, J. M., *Poly(ethylene glycol) Chemistry: Biotechnical and Biomedical Applications*. Plenum Press: New York, 1992.

46. Harris, J. M.; Zalipsky, S., Poly (ethylene glycol): Chemistry and Biological Applications. In *American Chemical Society*, Washington D.C., 1997.

47. Hoffman, A. S., Hydrogels for biomedical applications. *Adv. Drug Delivery Rev.* **2002,** 54, 3-12.

48. Hubbell, J. A., Synthetic biodegradable polymers for tissue engineering and drug delivery. *Curr. Opin. Solid State Mater. Sci.* **1998,** 3, 246-251.

49. Graham, N. B.; McNeill, M. E., Hydrogels for controlled drug delivery. *Biomaterials* **1984,** 5, 27-36.

50. Iza, M.; Stoianovici, G.; Viora, L.; Grossiord, J. L.; Couarraze, G., Hydrogels of poly(ethylene glycol): mechanical characterization and release of a model drug. *J. Control. Release* **1998,** 52, 41-51.

51. Leach, J. B.; Schmidt, C. E., Characterization of protein release from photocrosslinkable hyaluronic acid-polyethylene glycol hydrogel tissue engineering scaffolds. *Biomaterials* **2005,** 26, 125-135.

52. Quick, D. J.; Anseth, K. S., DNA delivery from photocrosslinked PEG hydrogels: encapsulation efficiency, release profiles, and DNA quality. *J. Control. Release* **2004,** 96, 341-351.

53. Ravichandran, P.; Shantha, K. L.; Panduranga Rao, K., Preparation, swelling characteristics and evaluation of hydrogels for stomach specific drug delivery. *Inter. J. Pharma.* **1997,** 154, 89-94.

54. Denes, A. R.; Somers, E. B.; Wong, A. C. L.; Denes, F., 12-Crown-4-ether and tri(ethylene glycol) dimethyl-ether plasma-coated stainless-steel surfaces and their ability to reduce bacterial biofilm deposition. *J. Appl. Poly. Sci.* **2001,** 81, 3425-3438.

55. Kingshott, P.; Griesser, H. J., Surfaces that resist bioadhesion. *Curr. Opin. Solid State Mater. Sci.* **1999,** 4, 403-412.

56. Shen, M.; Pan, Y. V.; Wagner, M. S.; Hauch, K. D.; Castner, D. G.; Ratner, B. D.; Horbett, T. A., Inhibition of monocyte adhesion and brinogen adsorption on glow discharge plasma deposited tetraethylene glycol dimethyl ether. *J. Biomater. Sci. Polym. Edn.* **2001,** 12, 961-978.

57. Shen, M.; Martinson, L.; Wagner, M. S.; Castner, D. G.; Ratner, B. D.; Horbett, T. A., PEO-like plasma polymerized tetraglyme surface interactions with leukocytes and proteins: in vitro and in vivo studies. *J. Biomater. Sci. Polym. Edn.* **2002,** 13, 367-390.

58. Shen, M.; Wagner, M. S.; Castner, D. G.; Ratner, B. D.; Horbett, T. A., Multivariate surface analysis of plasma-deposited tetraglyme for reduction of protein adsorption and monocyte adhesion. *Langmuir* **2003,** 19, 1692-1699.

59. Revzin, A.; Russell, R. J.; Yadavalli, V. K.; Koh, W.-G.; Deister, C.; Hile, D. D.; Mellott, M. B.; Pishko, M. V., Fabrication of poly(ethylene glycol) hydrogel microstructures using photolithography. *Langmuir* **2001,** 17, 5440-5447.

60. Revzin, A.; Tompkins, R. G.; Toner, M., Surface engineering with poly(ethylene glycol) photolithography to create high-density cell arrays on glass. *Langmuir* **2003,** 19, 9855-9862.

61. Andreopoulos, F. M.; Beckman, E. J.; Russell, A. J., Light-induced tailoring of PEG-hydrogel properties. *Biomaterials* **1998,** 19, 1343-1352.

62. Micic , M.; Zheng, Y.; Moy, V.; Zhang, X.-H.; Andreopoulos, F. M.; Leblanc, R. M., Comparative studies of surface topography and mechanical properties of a new, photo-switchable PEG-based hydrogel. *Coll. and Surf. B: Biointerf.* **2002,** 27, 147-158.

63. Mellott, M. B.; Searcy, K.; Pishko, M. V., Release of protein fromhighly cross-linked hydrogels of poly(ethylene glycol) diacrylate fabricated by UV polymerization. *Biomaterials* **2001,** 22, 929-941.

64. Zhang, L. H.; Zhang, W. D.; Zhang, Z. C.; Yu, L.; Zhang, H. F.; Qi, Y. C.; Chen, D. G., Radiation effects on crystalline polymers. 1. gamma-radiation-induced cross-linking and structural characterization of polyethylene oxide. *Radiat. Phys. Chem.* **1992,** 40, 501-505.

65. Yoshii, F.; Zhanshan, Y.; Isobec, K.; Shinozakic, K.; Makuuchi, K., Electron beam crosslinked PEO and PEO/PVA hydrogels for wound dressing. *Radiat. Phys. Chem.* **1999,** 55, 133-138.

66. Rosiak, J. M.; Ulanski, P., Synthesis of hydrogels by irradiation of polymers in aqueous solution. *Radiat. Phys. Chem.* **1999,** 55, 139-151.

67. Krsko, P.; Sukhishvili, S.; Mansfield, M.; Clancy, R.; Libera, M., Electron-beam surface-patterned poly(ethylene glycol) microhydrogels. *Langmuir* **2003,** 19, 5618-5625.

68. Lee, J. H.; Kopecek, J.; Andrade, J. D., Protein-resistant surfaces prepared by PEO-containing block copolymer surfactants. *J. Biomed. Mat. Research Part A* **1989,** 23, 351-368.

69. Grainger, D. W.; Kim, S. W.; Feijen, J., Poly(dimethylsiloxane)-poly(ethylene oxide)-heparin block copolymers.1. synthesis and characterization. *J. Biomed. Mat. Research Part A* **1988,** 22, 231-249.

70. Sofia, S. J.; Premnath, V.; Merrill, E. W., Poly(ethylene oxide) grafted to silicon surfaces: Grafting density and protein adsorption. *Macromolecules* **1998,** 31, 5059-5070.

71. Jenney, C. R.; Anderson, J. M., Effects of surface-coupled polyethylene oxide on human macrophage adhesion and foreign body giant cell formation in vitro. *J. Biomed. Mat. Research Part A* **1999,** 44, 206-216.

72. Prime, K. L.; Whitesides, G. M., Adsorption of proteins onto surfaces containing end-attached oligo(ethylene oxide) - a model system using self-assembled monolayers *J. Amer. Chem. Soc.* **1993,** 115, 10714-10721.

73. Drumheller, P. D.; Hubbell, J. A., Densely crosslinked polymer networks of poly(ethylene glycol) in trimethylolpropane triacrylate for cell-adhesion-resistant surfaces. *J. Biomed. Mat. Research Part A* **1995,** 29, 207-215.

74. Ratner, B. D.; Chilkoti, A.; Lopez, G. P., Plasma Deposition and Treatment for Biomaterial Applications. In *Plasma Deposition, Treatment, and Etching of Polymers*, d'Agostino, R., Ed. Academic Press, Inc.: San Diego, 1990.

75. Corbin, G. A.; Cohen, R. E.; Baddour, R. F., Solvent permeation in plasma-fluorinated polyethylene. *J. Appl. Polym. Sci.* **1985,** 30, 1407-1418.

76. Akovali, G., Plasma polymerization of ethane and some properties of pp-ethane as a protective coat. *J. Appl. Polym. Sci.* **1986,** 32, 4027-4042.

77. Sadhir, R. K.; James, W. J.; Yasuda, H. K.; Sharma, A. K.; Nichols, M. F.; Hahn, A. W., The adhesion of glow-discharge polymers, Silastic and Parylene to implantable platinum electrodes: results of tensile pull tests after exposure to isotonic sodium chloride. *Biomaterials* **1981,** 2, 239-243.

78. Haque, Y.; Ratner, B. D., Preparation and properties of plasma-deposited films with surface energies varying over a wide-range. *J. Appl. Polym. Sci.* **1986,** 32, 4369-4381.

79. Hanein, Y.; Pan, Y. V.; Ratner, B. D.; Denton, D. D.; Bohringer, K. F., Micromachining of non-fouling coatings for bio-MEMS applications. *Sensors and Actuators B* **2001,** 81, 49-54.

80. Mar, M. N.; Ratner, B. D.; Yee, S. S., An intrinsically protein-resistant surface plasmon resonance biosensor based upon a RF-plasma-deposited thin film. *Sensors and Actuators B* **1999,** 54, 125-131.

81. Pan, Y. V.; McDevitt, T. C.; Kim, T. K.; Leach-Scampavia, D.; Stayton, P. S.; Denton, D. D.; Ratner, B. D., Micro-scale cell patterning on nonfouling plasma polymerized tetraglyme coatings by protein microcontact printing. *Plasmas and Polymers* **2002,** 7, 171-183.

82. Bremmell, K. E.; Kingshott, P.; Ademovic, Z.; Winther-Jensen, B.; Griesser, H. J., Colloid probe AFM investigation of interactions between fibrinogen and PEG-like plasma polymer surfaces. *Langmuir* **2006,** 22, 313-318.

83. Bretagnol, F.; Lejeune, M.; Papadopoulou-Bouraoui, A.; Hasiwa, M.; Rauscher, H.; Ceccone, G.; Colpo, P.; Rossi, F., Fouling and non-fouling surfaces produced by plasma polymerization of ethylene oxide monomer. *Acta Biomat.* **2006,** 2, 165-172.

84. Kumar, D. S.; Fujioka, M.; Asano, K.; Shoji, A.; Jayakrishnan, A.; Yoshida, Y., Surface modification of poly(ethylene terephthalate) by plasma polymerization of poly(ethylene glycol). *J. Mater. Sci.: Mater. Med.* **2007,** 18, 1831-1835.

85. Muir, B. W.; Tarasova, A.; Gengenbach, T. R.; Menzies, D. J.; Meagher, L.; Rovere, F.; Fairbrother, A.; McLean, K. M.; Hartley, P. G., Characterization of low-fouling ethylene glycol containing plasma polymer films. *Langmuir* **2008,** 24, 3828-3835.

86. James, C. D.; Davis, R.; Meyer, M.; Turner, A.; Turner, S.; Withers, G.; Kam, L.; Banker, G.; Craighead, H.; Issacson, M.; Turner, J.; Shain, W., Aligned microcontact printing of micrometer-scale poly-L-lysine structures for controlled growth of cultured neurons on planar micro-electrode arrays. *IEEE Trans. Biomed. Eng.* **2000,** 47, 17-21.

87. Yakacki, C. M.; Shandas, R.; Lanning, C.; Rech, B.; Eckstein, A.; Gall, K., Unconstrained recovery characterization of shape-memory polymer networks for cardiovascular applications. *Biomaterials* **2007,** 28, 2255-2263.

88. Dong, Y.; Zhang, Z.; Feng, S.-S., d-alpha-Tocopheryl polyethylene glycol 1000 succinate (TPGS) modified poly(l-lactide) (PLLA) films for localized delivery of paclitaxel. *Int. J. Pharm.* **2008,** 350, 166-171.

89. Bhatia, V.; Bhatia, R.; Dhindsa, M., Drug-eluting stents: new era and new concerns. *Postgrad. Med. J.* **2004,** 80, 13-18.

90. Udipi, K.; Chen, M.; Cheng, P.; Jiang, K.; Judd, D.; Caceres, A.; Melder, R. J.; Wilcox, J. N., Development of a novel biocompatible polymer system for extended drug release in a next-generation drug-eluting stent. *J. Biomed. Mat. Research Part A* **2007,** 85, 1064-1071.

91. Ong, A. T. L.; Serruys, P. W., Technology insight: an overview of research in drug-eluting stents. *Nat. Clin. Prac. Cardio. Med.* **2005,** 2, 647-658.

92. Drachman, D. E.; Edelman, E. R.; Seifert, P.; Groothuis, A. R.; Bornstein, D. A.; Kamath, K. R.; Palasis, M.; Yang, D.; Nott, S. H.; Rogers, C., Neointimal thickening after stent delivery of paclitaxel: change in composition and arrest of growth over six months. *J. Amer. Coll. Cardiol.* **2000,** 36, 2325-2332.

93. Farb, A.; Heller, P. F.; Shroff, S.; Cheng, L.; Kolodgie, F. D.; Carter, A. J.; Scott, D. S.; Froehlich, J.; Virmani, R., Pathological analysis of local delivery of paclitaxel via a polymer-coated stent. *Circulation* **2001,** 104, 473-479.

94. Lewis, A. L.; Vick, T. A.; Collias, A. C. M.; Hughes, L. G.; Palmer, R. R.; Leppard, S. W.; Furze, J. D.; Taylor, A. S.; Stratford, P. W., Phosphorylcholine-based polymer coatings for stent drug delivery. *J. Mater. Sci. Mater. Med.* **2001,** 12, 865-870.

95. Nederberg, F.; Watanabe, J.; Ishihara, K.; Hilborn, J.; Bowden, T., Organo hydrogel hybrids. formation of reservoirs for protein delivery. *Biomacromolecules* **2005,** 6, 3088-3094.

96. Kavanagh, C. A.; Rochev, Y. A.; Gallagher, W. M.; Dawson, K. A.; Keenan, A. K., Local drug delivery in restenosis injury: thermoresponsive co-polymers as potential drug delivery systems. *Pharma. Therap.* **2004,** 102, 1-15.

97. Gutowska, A.; Bae, Y. H.; Feijen, J.; Kim, S. W., Heparin release from thermosensitive hydrogels. *J. Control. Release* **1992,** 22, 95-104.

98. Rochev, Y.; Golubeva, T.; Gorelov, A.; Allen, L.; Gallagher, W. M.; Selezneva, I.; Gavrilyuk, B.; Dawson, K., Surface modification for controlled cell growth on copolymers of N-isopropylacrylamide. *Prog. Coll. Polym. Sci.* **2001,** 118, 153-156.

99. Doorty, K. B.; Golubeva, T. A.; Gorelov, A. V.; Rochev, Y. A.; Allen, L. A.; Dawson, K. A.; Gallagher, W. M.; Keenan, A. K., Poly(N-isopropylacrylamide) co-polymer films as potential vehicles for delivery of an antimitotic agent to vascular smooth muscle cells. *Cardiovasc. Pathol.* **2003,** 12, 105-110.

100. Yasuda, H., Plasma polymerization for protective coatings and composite membranes. *J. Membr. Sci.* **1984,** 18, 273-284.

101. Hollahan, J. R.; Wydeven, T.; Johnson, C. C., Combination moisture resistant and antireflection plasma polymerized thin films for optical coatings. *Appl. Opt.* **1974,** 13, 1844-1849.

102. Wydeven, T.; Johnson, C. C., Water-vapor resistance of plasma-polymerized coatings on potassium-bromide windows. *Polym. Eng. Sci.* **1981,** 21, 650-657.

103. Cho, D. L.; Yasuda, H. K.; Mittal, K. L., *Adhesion, Barrier, and Passivation Characteristics of Plasma Polymerized Thin Films*. Plenum: New York, 1985.

104. Yasuda, H.; Stannett, V., Permeability. In *Polymer Handbook*, 2nd ed.; Brandrup, J.; Immergut, E. H., Eds. Wiley: New York, 1975.

105. Chatham, H., Oxygen diffusion barrier properties of transparent oxide coatings on polymeric substrates. *Surf. Coat. Technol.* **1996,** 78, 1-9.

106. da Silva Sobrinho, A. S.; Latreche, M.; Czeremuszkin, G.; Klemberg-Sapieha, J. E.; Wertheimer, M. R., Transparent barrier coatings on polyethylene terephthalate by single- and dual-frequency plasma-enhanced chemical vapor deposition. *J. Vac. Sci. Technol. A* **1998,** 16, 3190-3198.

107. da Silva Sobrinho, A. S.; Czeremuszkin, G.; Latreche, M.; Wertheimer, M. R., Study of defect numbers and distributions in PECVD SiO2 transparent barrier coatings on PET. *Proc. Mater. Res. Soc. Symp.* **1999,** 544, 245-250.

108. da Silva Sobrinho, A. S.; Czeremuszkin, G.; Latreche, M.; Wertheimer, M. R., Defect-permeation correlation for ultrathin transparent barrier coatings on polymers. *J. Vac. Sci. Technol. A* **2000,** 18, 149-157.

109. Rossi, G.; Nulman, M., Effect of local flaws in polymeric permeation reducing barriers. *J. Appl. Phys.* **1993,** 74, 5471-5475.

110. Hanika, M.; Langowski, H.-C.; Moosheimer, U.; Peukert, W., Inorganic layers on polymeric films—Influence of defects and morphology on barrier properties. *Chem. Eng. Technol.* **2003,** 26, 605-614.

111. Tropsha, Y. G.; Harvey, N. G., Activated rate theory treatment of oxygen and water transport through silicon oxide/ poly(ethylene terephthalate) composite barrier structures. *J. Phys. Chem. B* **1997,** 101, 2259-2266.

CHAPTER 3

EFFECT OF PLASMA PROCESSING CONDITIONS ON DEPOSITION RATE AND STRUCTURE

3.1 Introduction

In this chapter, a parallel-plate capacitively-coupled plasma deposition system, designed and built for the growth of polyethylene glycol-like films, is described. The reactor system was characterized by systematic variation of plasma parameters, initially, to determine if deposition rates of the resultant polymer films were consistent with previously reported PEG-like film studies. Chemical bonding structures in the film, as determined by Fourier transform infrared spectroscopy, offer another indication of the extent to which deposited film properties correlate with those of films formed by traditional solution polymerization methods. Characterization of deposition rates and bonding structures provide information on the relationship between plasma parameters invoked and the film properties, and thereby suggest potential applications for the coatings. Indeed, a wide variety of plasma-polymerized films have been studied[1-4] to determine how processing conditions alter polymer deposition rate and film chemistry. Among the most well-investigated plasma parameters are: RF power[5, 6], reactor pressure[5] and substrate temperature.[7, 8]

The effect of radio frequency input power on deposition rate and film properties is sometimes coupled with other plasma parameters to allow comparison of results from different reactor geometries and flow rates. One way to standardize these results is through the use of the ratio W/W_o, where W is the actual input power and W_o is the minimum power required to initiate and sustain the plasma at a specific pressure.[9] This ratio has been reported to have little dependence on pressure and geometry of the

discharge chamber and so can be an effective tool in describing the power dependence of deposition rate.[9] Another commonly used ratio is *W/FM*, where *F* is the monomer flow rate and *M* is the molecular weight of the precursor.[10] This expression represents the power applied per unit mass of material and thus does not depend on the chamber geometry nor on flow patterns within the reactor. In addition, this ratio is useful when comparing power dependence of deposition rate of different monomers. The standard used in this study is power density, which can be used to describe the power per unit area of the substrate electrode (W/cm^2) or, the power applied to the glow volume region of the discharge (W/cm^3).[1, 11] For RF powered systems, power density may be used because it provides the simplest set of guidelines for power ranges (~0.1-1.0 W/cm^2) in a parallel plate electrode configuration,[12] especially when other reactor geometries are not compared and flow rates are constant.

Reactor pressure is sometimes misunderstood to be the pressure of the system *before* the glow discharge is initiated, p_b, rather than the system pressure *during* the polymerization process, p_d. It has been demonstrated[13] that the pressure before plasma initiation is entirely dependent on the pumping speed of the vacuum system but that after plasma ignition, pressure increases, p_i, are due to the creation of additional vapor species (increase in the number of moles of gas) from bond breaking collisions. The specific p_i observed is a function of monomer structure and discharge power.[13] Deposition pressure equals the sum of p_b and p_i. Since the gas velocity and degree of ionization are dependent on pressure,[14] p_d, and not p_b, is the determining factor for control of polymer properties. For a substrate at a certain temperature, a thermal boundary layer exists over the surface and extends for some distance over which the gas molecules inside this region are maintained at a temperature close to that of the substrate.[15] Because this layer is much thicker than the mean free path of the gas molecules, the species impinging on the growing film are already at the surface temperature. However, previous studies[16] on fluorocarbon films have noted that deposition is a highly exothermic process. Over the

timeframe of a deposition, substrate temperatures can increase substantially, especially if the set point temperature is low. As surface temperature set points rise, the increase is less noticeable. For the fluorocarbon system investigated,[16] a much smaller increase in substrate temperatures was noticed at 180°C versus 120°C (~40°C) at constant power and deposition time, and this was correlated to lower deposition rates and higher heat transfer to surroundings.

3.2 Experimental Details

3.2.1 Plasma Reactor Description and Deposition

A parallel-plate capacitively-coupled radio frequency (RF) discharge reactor was designed to deposit polyethylene glycol (PEG)-like films using tetraethylene glycol dimethyl ether (TGDE) as a precursor. A schematic of the deposition system is shown in figure 3.1.

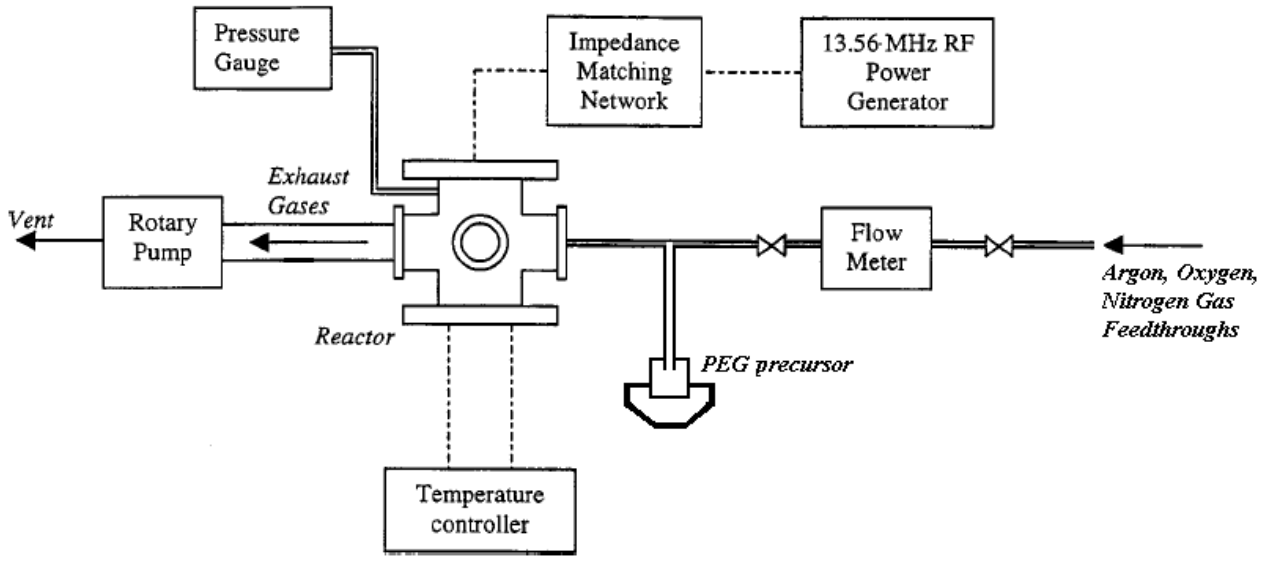

Figure 3.1. Parallel-plate plasma reactor system

A standard stainless steel eight-inch six-way ultra-high vacuum deposition chamber was purchased from the Kurt J. Lesker Company. Blank conflat flanges were machined with ports for (1) monomer introduction, (2) pressure monitoring, (3) temperature control, (4) vacuum outlet, (5) power feedthrough, and (6) sample loading. Monomer residence time was controlled using an Alcatel two-stage C2 Series 2033 rotary vane pump and heating tape from Omega Engineering was wrapped around the entire reactor exterior to allow homogeneous heating and prevention of precursor condensation on the inside walls. A glow discharge was initiated using a 50-Ω Rohde & Schwarz SML01 rf power source at a frequency of 13.56 MHz; a Heathkit SA-2060A impedance matching network was inserted between the signal generator and powered top electrode to ensure efficient power transfer to the low pressure gas. Samples were placed on the bottom grounded electrode and heated using two 1.50 inch Omegalux CSH series cartridge heaters. A type K thermocouple and feedthrough were used to monitor the temperature of the bottom electrode. Figure 3.2 shows a schematic of the electrode configuration.

Each electrode measured 2.5 inches in diameter and the interelectrode spacing was 0.5 inch. The top electrode was tapped with two connection points: one for an RF cable which transmits RF power to the electrode, and another for a 0.5 inch diameter ceramic rod that facilitated electrical isolation. A ceramic spacer separated the bottom electrode from the metallic support to (1) help confine the discharge region to the volume between the electrodes and (2) prevent creation of a heat sink.

Tetraethylene glycol dimethyl ether (Sigma-Aldrich – 99%, TGDE) was used as the precursor in polymerization processes and was introduced from a side entry port of the deposition chamber. Effluent, including any unreacted monomer species, was pumped out of the system from an exit port located at the opposite end (180°) from the entry. Figure 3.3 shows the monomer structure. Liquid TGDE was heated to approximately 150°C under vacuum and pressure-driven vapor flow was manually

controlled with a Teflon plug. Heated quarter-inch stainless steel tubing carried the vaporized TGDE from the storage flask to the chamber, using argon as a carrier gas. Flow rates of argon, oxygen (plasma cleaning) and nitrogen (pressurization) were controlled with an MKS Instruments type 1179A mass flow controller.

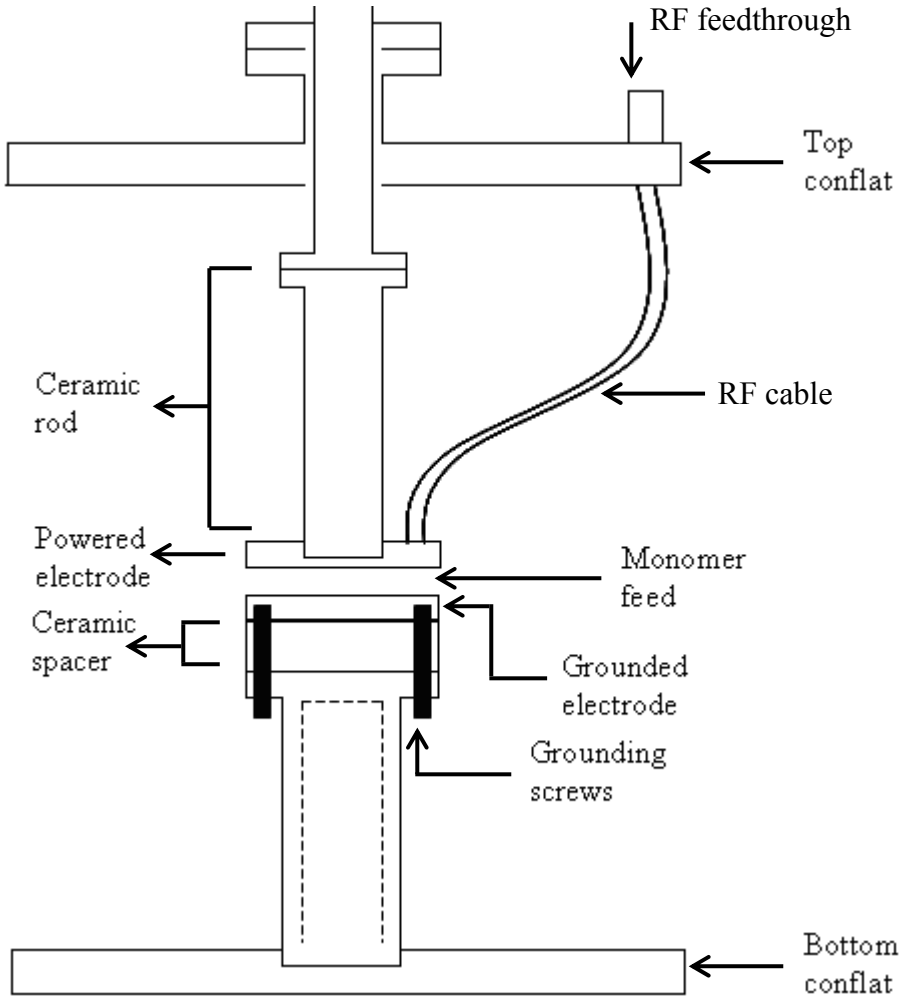

Figure 3.2. Electrode configuration within the reactor

Prior to film deposition, substrates were cleaned using an oxygen plasma. In a pure oxygen plasma, electron impact dissociated oxygen atoms and plasma-generated ozone attack organic contaminants and form volatile CO, H_2O and CO_2 products.[15, 17] This surface pretreatment also altered the silicon substrate and therefore enhanced

adhesion of the PEG films to the substrate. Oxygen plasma treatments were conducted for two minutes at 1000 mTorr reactor pressure, 55 W RF power, and a flowrate of 75 standard cubic centimeters per minute (sccm). A manual throttle valve (MKS Instruments) was used to control pressure by manipulation of pump conductance, since an increase in the number of moles of vapor species increased after a discharge was struck. Thin films of PEG-like material were deposited at varying pressure, RF power and substrate temperature; the specific conditions investigated are summarized in table 3.1. Film thickness and bonding structure were characterized using variable angle spectroscopic ellipsometry (VASE) and Fourier transform infrared spectroscopy (FTIR).

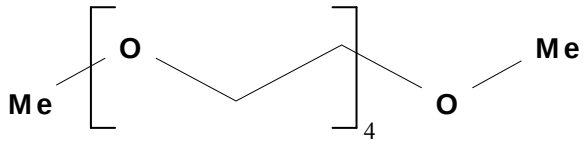

Figure 3.3. Tetraethylene glycol dimethyl ether structure

3.2.2 Variable Angle Spectroscopic Ellipsometry

Film thickness was determined using a variable angle M-2000V spectroscopic ellipsometer from J.A. Woollam Co., Inc. Measurements were performed over a wavelength range of 370 to 1000 nm at angles of 65, 70 and 75°,[18] and evaluated using a Cauchy model layer[19] and a standard silicon substrate library data file.[20] The dispersion relation of a Cauchy layer can be described using the equation:

$$n = A + \frac{B}{\lambda^2} + \frac{C}{\lambda^4} \qquad (3.1)$$

where, n is the refractive index, λ the wavelength of light and A, B, and C are the Cauchy constants. Static data acquisition and analysis was carried out using the accompanying WVASE32 software which allowed data fitting with the multilayer Marquardt-Levenburg algorithm. Fitting was performed so that the mean square error (MSE) associated with

the fit was less than 30. Furthermore, fits to the data were discarded if the refractive index of the fitted Cauchy layer did not show an exponential decrease with an increase in the wavelength.

3.2.3 Fourier Transform Infrared Spectroscopy

Solid state Fourier transform infrared spectroscopy (FTIR) was performed under vacuum (~1500 mTorr) at a resolution of 4 cm^{-1} on the plasma-polymerized PEG films using a Bruker Optics IFS 66 series FTIR spectrometer to determine the bonding structures present in the film. Data collection was performed under vacuum in the mid-IR range from 4000 to 400 cm^{-1}. Film spectra were collected in the absorbance mode and averaged over 256 scans to minimize noise and maximize signal-to-noise ratio. Spectra from a background silicon wafer was collected as a reference and subtracted from film spectra.

3.3 Results and Discussion

3.3.1 Effect of Plasma Processing Conditions on Deposition Rate

Initial attempts to characterize the plasma reactor system began by studying the effects of excitation power, operating pressure and substrate temperature on polymer film deposition rate. Input RF power was established at 32 and 55 W which correspond to power densities of ~1.0 and ~1.5 W/cm^2, respectively. Deposition pressures were maintained at 1000, 1200 or 1400 mTorr and substrate temperatures were controlled at either 95 or 110°C. Reaction conditions and their associated deposition rates are summarized in table 3.1.

Table 3.1. Variation of RF power, chamber pressure and sample temperature and their effects on plasma deposition rate

Sample No.	Excitation Power (W)	Reactor Pressure (mTorr)	Substrate Temperature (°C)	Deposition Rate (nm/min)
1	32	1400	95	28.6
2	32	1400	110	19.8
3	55	1400	110	28.9
4	55	1000	110	27.4
5	32	1000	110	19.6
6	55	1200	110	29.0
7	55	400	110	14.4
8	32	750	110	12.1
9	55	1000	135	11.8

3.3.1.1 Excitation Power

The effect of applied power on polymer deposition rate may be determined directly by comparing samples 2 versus 3 (constant pressure: 1400 mTorr; substrate temperature: 110°C) and 4 versus 5 (constant pressure: 1000 mTorr; substrate temperature: 110°C). The deposition rate for sample 3 at an input power of 55 W equals ~29 nm/min versus ~20 nm/min for sample 2 at 32 W. Likewise, the deposition rate for sample 4 at an input power of 55 W is ~27 nm/min compared with ~20 nm/min for sample 5 at 32 W. In both comparisons, a higher power input (55 W) resulted in an increased deposition rate. At higher RF powers, average electron energies increase, which corresponds to a larger fraction of electrons in the high energy tail of the electron energy distribution function.[11] Thus, a greater amount of energy is transferred in each inelastic collision, which leads to enhanced ion and free electron formation. This generates a higher electron density and thus an increased current density.[21, 22] A greater ion concentration enhances the flux of reactive species accelerated by the sheath electric field onto the substrate surface.[1, 11] Such phenomena yield an increased deposition rate at higher power levels, consistent with the results observed. Similar results have been

reported for fluorocarbon polymerization,[6, 16] where it was determined that increases in deposition rate with increases in power are indicative of power-limited regime process.

3.3.1.2 Reactor Pressure

Operating pressure is another important parameter that affects the deposition rate in plasma polymerization processes. The effect of pressure may be evaluated by comparing samples 3, 4, 6, and 7. Each of these experimental runs was conducted at a constant RF power input of 55 W and a substrate temperature of 110°C. Deposition rate rapidly increases from ~14 nm/min to ~27 nm/min as system pressure increases from 400 mTorr to 1000 mTorr, respectively. An increasing deposition rate with pressure has been observed previously with plasma deposited polymer films.[3, 19, 20] However, sequential increases of 200 mTorr (1200 mTorr: 29 nm/min) up to 1400 mTorr (~29 nm/min) does not significantly alter deposition rate. A similar trend is seen in comparing samples 2, 5, and 8, where power was kept constant at 32 W and sample temperature was maintained at 110°C. The deposition rate started at ~12 nm/min at a pressure of 750 mTorr and leveled off to ~20 nm/min at 1000 and 1400 mTorr. Because the pressure-driven flow rate of monomer into the chamber remains constant over the duration of the experiment, an increase in pressure in this reaction vessel results in a greater concentration of vapor phase ionic species, which are created by an increased number of inelastic collisions after glow discharge ignition.[1, 23] The increase in inelastic collisions is achieved by manually controlling the residence time of the flow species through manipulation of pump conductance. By reducing the exhaust flow rate, the residence time of reactant species in the discharge increases, thus increasing the probability of energy transfer collisions.[22] However, if the concentration of vapor phase reactants is too high as a result of increased pressure, electron energies fall and energy transfer is reduced; thus, the number density of electrons and ionic species decreases.[17] This is because as the number of inelastic

collisions increases, average electron energy decreases ($\bar{\varepsilon} \propto \frac{C_1}{p_g}$; C_1 = constant, p_g = gas pressure). Both electron energy and collision frequency affect the reactive species (ion and radical) generation and recombination rates and the energies at which they impinge the substrate surface. Past studies[3, 24] have shown that the rate of polymer deposition goes through a maximum with increasing pressure and that any further increases in pressure result in a decrease of deposition rate. In this study, the upper bound of operating pressure is limited to 1400 mTorr since poor quality films were obtained at elevated pressures. Specifically, the films appear inhomogeneous and cloudy, apparently due to enhanced particle formation, and thus unsuitable for thickness measurements using ellipsometry.

3.3.1.3 Substrate Temperature

The effect of substrate temperature on deposition rate can be determined by comparing samples 1 and 2 (constant power: 32 W; pressure: 1400 mTorr) and also samples 4 and 9 (constant power: 55 W; pressure: 1000 mTorr). The deposition rate for sample 1 was ~ 29 nm/min at 95°C versus ~20 nm/min for sample 2 at 110°C. For sample 4, the deposition rate was ~27 nm/min at 110°C versus ~12 nm/min for sample 9 at a substrate temperature of 135°C. Deposition rate increases with a decrease in sample temperature in both instances. As with the limiting case of the highest pressure investigated, experimental runs conducted at substrate temperatures lower than 95°C resulted in non-reflective and unstable samples. Using Antoine's equation[25] it was determined that for the deposition pressures used in this study, the minimum temperature required to prevent condensation of TGDE is ~95-100°C. The poor quality samples obtained at lower substrate temperatures may be due to monomer condensation. The controlling determinants of polymer deposition are transport of reactive species to the substrate and chemical surface reactions. The observed relationship between deposition

rate and substrate temperature correlates well with trends reported previously[15, 19, 22, 23] and is indicative of an adsorption-limited process with a negative Arrhenius activation energy, as expressed by

$$r = Ae^{-E_a T} \tag{3.2}$$

where r is the deposition rate, A is the extrapolated specific deposition rate at temperature, T, equal to zero and E_a is the activation energy. It has been determined[26] that the activation energy is independent of discharge conditions such as RF power or monomer flow rate but rather, is related to a particular class of precursor (e.g. hydrocarbons versus fluorocarbons). For an adsorption-limited process, a negative Arrhenius activation energy suggests[27] that even though rate constants of surface reactions increase with increasing substrate temperatures, the surface concentration of adsorbed reactive species decreases more rapidly, leading to an overall decrease in deposition rate. If monomer flow rate (therefore pressure) and input power are constant, the density of reactive species in the plasma will also remain constant because free electrons in the bulk will have equal mean free paths and energies. Ions entering the sheath region, and therefore the thermal boundary layer close to the substrate, should also have roughly equivalent energies.[11, 15] Based on the relationship between deposition rate and substrate temperature,[16, 28] if substrate temperature rises substantially over the course of the deposition time,[16] the rate of film growth would decrease with time. Because substrate temperature increases by only 2-3°C over the deposition time, the deposition rate of samples 1, 2, 4, and 9 is constant and thickness increases are roughly linear with time.

3.3.2 Bonding Structure of Plasma-Polymerized PEG-Like Films

Solid-state Fourier transform infrared spectroscopy (FTIR) is a technique that can be used to compare the bonding structures of the plasma-polymerized PEG-like films to those of solution-polymerized, spun-cast PEG layers. The FTIR spectrum of a plasma-

polymerized PEG-like film is shown in figure 3.4; absorbance peaks and associated bonding structures are summarized in table 3.2. Figure 3.4 is a representative spectrum of FTIR data from samples 1-9 because over the deposition conditions investigated in this thesis, plasma processing conditions did not significantly alter film chemistry. For plasma-polymerized films, it has been determined[6, 29] that film chemistry is dictated more by the structure of the precursor than by processing conditions.

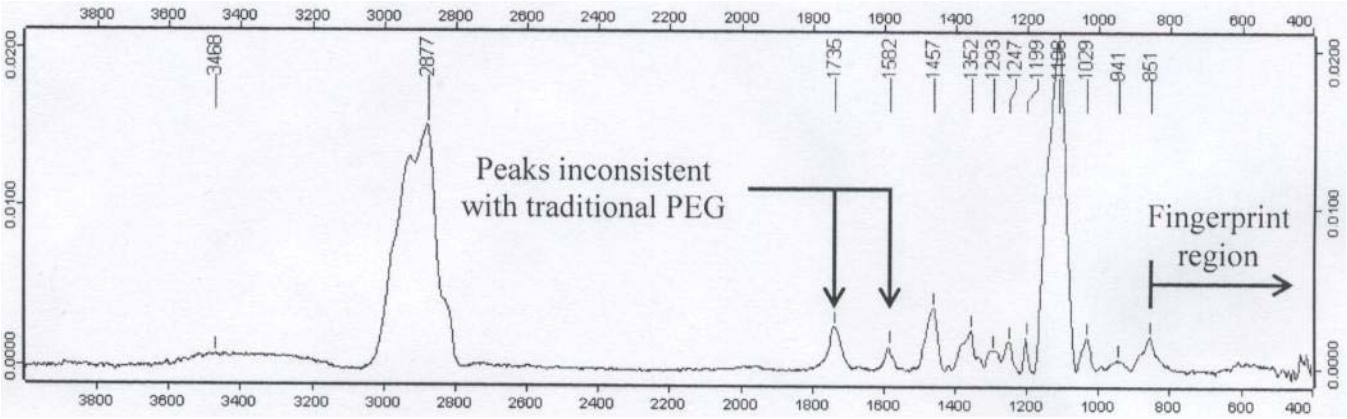

Figure 3.4. FTIR spectrum for a plasma-polymerized PEG-like film (~200 nm) deposited at 55 W, 110°C and 1000 mTorr

Table 3.2. Bonding structure assignments for peaks appearing in plasma-deposited PEG-like films that are also observed in solution-polymerized PEG[30]

Functional Group	Stretch Frequency (cm^{-1})	Comments
Hydrogen-bonded O–H	3468	Usually with variable intensity
–O–CH_3	2877	–CH_3 asymmetric stretch. Between 2985-2920 cm^{-1} for non-ethers
	1457	–CH_3 symmetric/asymmetric deformation vibration
	1199	–CH_3 rocking vibration
Saturated aliphatic ethers, C–O–C	1108	C–O–C asymmetric stretch
	1029	C–O–C symmetric stretch Weak or absent from symmetric ethers
	941	
	851	
–$(CH_2)_n$–	1293	Not usually seen in IR. Intensity increases with *n*
EtO– (ethers)	1352	CH_2 wagging vibration
	1247	CH_2 twisting vibration

Figure 3.4 indicates that the plasma-deposited film has a characteristic absorption at ~1108 cm^{-1}, which is associated with the C-O-C asymmetric vibration. In addition, peaks at 1352 cm^{-1} (CH_2 wagging) and 1247 cm^{-1} (CH_2 twisting) provide evidence for the presence of ethyl ether (EtO-) moieties. Because inelastic electron-molecule collisions in the discharge generate a variety of ions, free radicals and excited state molecules, chemical bonding structures that are not characteristic of solution-polymerized PEG layers are generated in the plasma-deposited films. Hence, the term "PEG-like" is used to describe the resulting film structure. The specific chemical functionalities that differentiate the current films from those of traditional PEG materials are summarized in table 3.3. The peak at 1735 cm^{-1} indicates the presence of a carbonyl group, although it is unclear whether this peak is associated with ketone, aldehyde, carboxylic acid or ester functionalities. However, formation of ketones and esters may be more likely due to the existence of C-O-C linkages in the precursor structure. Aldehydes and acids are analogous to hydroxyl groups in that they generally signify chain termination, and thus, termination of further crosslinking. Based of the lack of a strong –OH absorption in the IR spectrum, it is unlikely that the majority of carbonyl moieties originate from aldehydes and carboxylic acids.

Table 3.3. Bonding structure assignments for peaks appearing in plasma-deposited PEG-like films but lacking in spectra of solution-polymerized PEG[30]

Functional Group	**Stretch Frequency (cm^{-1})**	**Comments**
C=C conjugated with C=C or C=O.	1582.	C=C–C=C usually ~1600 cm^{-1}.
Saturated aliphatic ketones or, aldehydes or, carboxylic acids or, esters.	1735.	Carbonyl group (C=O) common to all functional groups.

FTIR spectra of the plasma-polymerized polymer films indicated that the coatings were PEG-like in structure by comparison to both bulk PEG[30, 31] as well as to earlier work[32] on pulsed-plasma polymerized films that used diethylene glycol dimethyl ether as

the precursor. Comparison of the IR spectrum of traditional solution-polymerized PEG[30] with our plasma-polymerized PEG indicates that the plasma polymerized films resemble a high molecular weight polymer, as evidenced by narrow (sharp) peaks and the lack of a strong –OH stretch in the region of 3400-3600 cm^{-1}. Comparisons of low- and high-molecular weight solution-polymerized PEG are shown in figure 3.5. From figure 3.5, a direct, inverse correlation can be made between the molecular weight of a polymer chain and the intensity of the hydroxyl stretching vibration. For PEG brushes on a gold substrate,[33] refractive index values vary between 1.42-1.45 (pure PEG polymer solutions have similar refractive indices[34]). In chemically-crosslinked structures, hydroxyl moieties typically represent termination groups. Thus, the weak OH absorption observed in figure 3.4 suggests a more heavily crosslinked polymeric matrix, consistent with the fact that refractive indices of the plasma-polymerized films range between ~1.48-1.50. Previous investigations[35] of plasma polymers confirm that refractive index is an indirect measurement of crosslink density.

It is also instructive to compare FTIR spectra from films obtained in this study to those formed by pulsed-plasma polymerization of diglyme;[32] a typical spectrum of a PEO-like film from Ref. 27 is shown in figure 3.6. From figure 3.6, intense, sharp peaks at ~1130 cm^{-1} and ~1188 cm^{-1} reflect the presence of a C-O-C stretch and are evidence of a C-O polymerized functional group. The C-O-C peak, which is shifted toward shorter wavelengths, is ascribed to an elevated C-O-C ratio in the film structure[32] as compared to the higher molecular weight layer whose FTIR spectrum is shown in figure 3.5(b). These observations, along with the higher refractive indices of films in the current study, indicate a more highly crosslinked coating. The spectrum in figure 3.6 also shows the presence of a C=C bond that is conjugated with an ether group. The conjugation causes the C=C stretch at ~1630 cm^{-1} to separate into two peaks.[32] Comparison to figure 3.4 demonstrates that the C=C peak occurs at 1582 cm^{-1}, which suggests conjugation with

either another ethane group, or with the carbonyl group positioned at 1735 cm^{-1}. Finally, both spectra detect the presence of hydroxyl moieties within the body of the film.

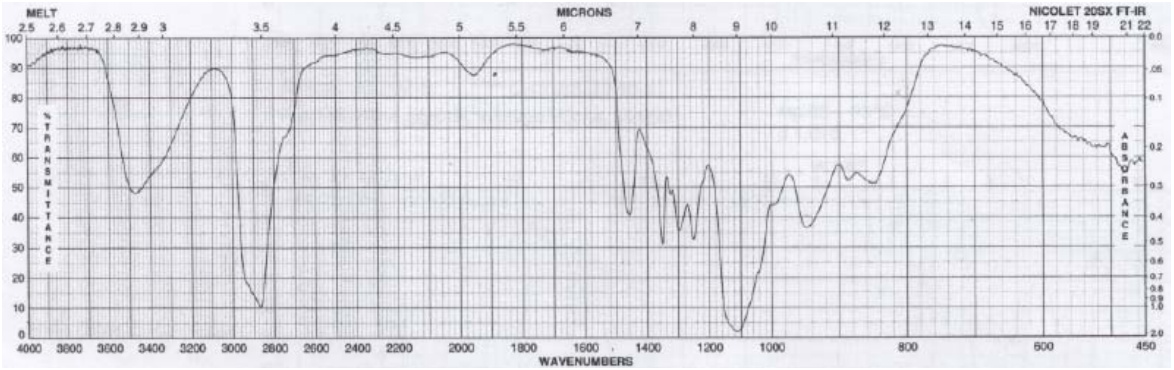

(a)

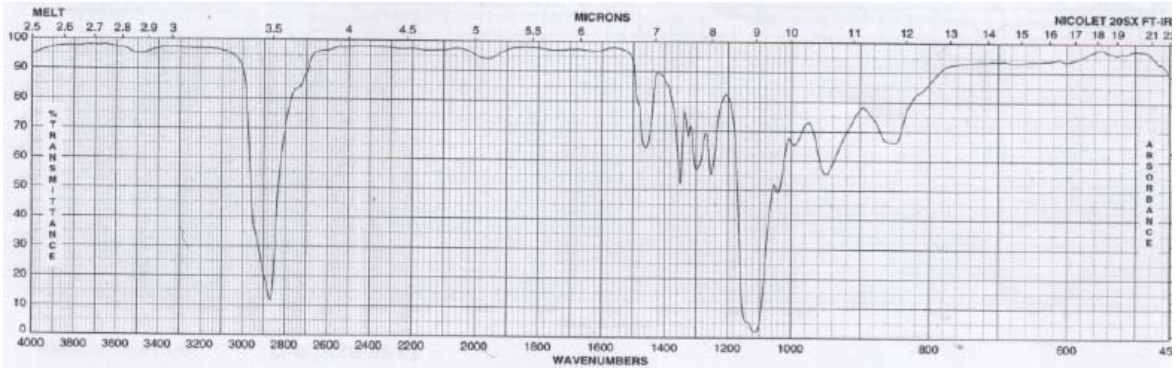

(b)

Figure 3.5. FTIR spectra of solution-polymerized PEG for (a) molecular weight 600 g/mol and, (b) molecular weight 10000 g/mol[30]

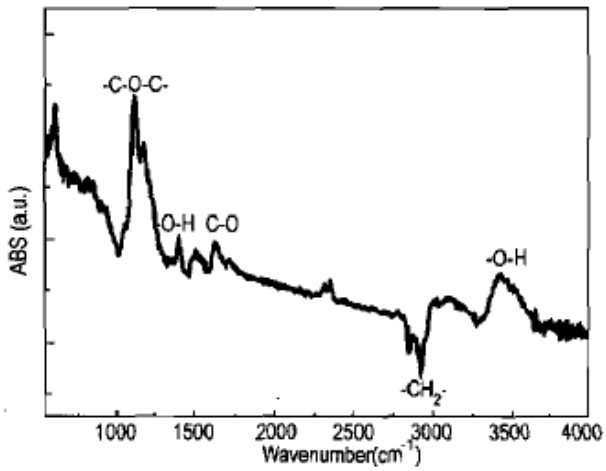

Figure 3.6. FTIR spectrum of a typical plasma-polymerized PEO-like film from diethylene glycol dimethyl ether[32]

3.4 Conclusions

In this chapter, deposition rates of PEG-like films were discussed as a function of RF input power, operating pressure and substrate temperature. Applied power levels were 32 W and 55 W, which correspond to power densities of ~1.0 W/cm^2 and ~1.5 W/cm^2, respectively at constant pressure and substrate temperature. Deposition rates increased at the higher power input. This was attributed to larger average electron energies, a higher probability of inelastic collisions and therefore higher electron and ion current densities. Operating pressure was varied from ~0.5 to ~1.5 Torr at constant power and temperature. Deposition rate increased with increasing pressure. At lower pressures, generation of free electrons and ions (e.g. current density) is limited by the frequency of inelastic collisions while at sufficiently high pressures, the mean free path drops, and thus the energy transfer per collision is reduced, leading to lower concentrations of radicals and ions. As a result, deposition rate as a function of pressure goes through a maximum. Limitations in the upper bound of operating pressure related to roughness and cloudy sample surfaces inhibited the generation of deposition rate versus pressure data at still higher pressures. Substrate temperature was varied between 95°C and 135°C at constant power and pressure. Deposition rate increased with a decrease in sample temperature which is indicative of an adsorption-limited process.

Bonding structure was examined using Fourier transform infrared spectroscopy and compared to the structures reported for solution-polymerized spun-cast PEG films and pulsed-plasma polymerized PEO-like films. The plasma-polymerized PEG-like coatings synthesized in this study resembled higher molecular weight solution-polymerized films, as indicated by the lack of an intense hydroxyl peak and because our plasma films have higher refractive indices than the solution-polymerized PEG. Such observations indicate a more highly crosslinked structure, consistent with the plasma atmosphere. The PEG-like structures polymerized from TGDE monomer were compared with those from pulsed-plasma polymerized PEO-like films synthesized from diethylene

glycol dimethyl ether. Spectra from both samples showed a characteristic C-O-C stretch, along with the existence of hydroxyl termination sites and the presence of an ethene functionality.

3.5 References

1. Yasuda, H., Glow-discharge polymerization. *J. Polym. Sci. Macromol. Revs.* **1981,** 16, 199-293.

2. Kobayash, H.; Shen, M.; Bell, A. T., Effects of reaction conditions on plasma polymerization of ethylene. *J. Macromol. Sci. Chem.* **1974,** A8, 373-391.

3. Westwood, A. R., Glow discharge polymerization. 1. Rates and mechanisms of polymer formation. *Eur. Poly. J.* **1971,** 7, 363-375.

4. Westwood, A. R., Glow discharge polymerization. 2. The structure of glow discharge polymers. *Eur. Poly. J.* **1971,** 7, 377-385.

5. Martin, Y.; Boutin, D.; Vermette, P., Study of the effect of process parameters for n-heptylamine plasma polymerization on final layer properties. *Thin Solid Films* **2007,** 515, 6844-6852.

6. Agraharam, S.; Hess, D. W.; Kohl, P. A.; Bidstrup Allen, S. A., Plasma chemistry in fluorocarbon film deposition from pentafluoroethane/argon mixtures. *J. Vac. Sci. Technol. A* **1999,** 17, 3265-3271.

7. Lopez, G. P.; Ratner, B. D., Substrate temperature effects on film chemistry in plasma depositions of organics. II. Polymerizable precursors. *J. Polym. Sci., Polym. Chem. Ed.* **1992,** 30, 2415-2425.

8. Lopez, G. P.; Chilkoti, A.; Briggs, D.; Ratner, B. D., Substrate temperature effects on film chemistry in plasma deposition of organics. III. Analysis by static secondary ion mass spectrometry. *J. Polym. Sci., Polym. Chem. Ed.* **1992,** 30, 2427-2441.

9. Duval, M.; Theoret, A., Polymerization of benzene in a capacitively coupled RF plasma. *J. Appl. Polym. Sci.* **1973,** 17, 527-537.

10. Yasuda, H.; Hirotsu, T., Critical evaluation of conditions of plasma polymerization. *J. Polym. Sci., Polym. Chem. Ed.* **1978,** 16, 743-759.

11. Morosoff, N., An Introduction to Plasma Polymerization. In *Plasma Deposition, Treatment, and Etching of Polymers*, d'Agostino, R., Ed. Academic Press, Inc.: San Diego, 1990.

12. Lieberman, M. A.; Gottscho, R. A., Design of High-Density Plasma Sources for Materials Processing. In *Plasma Sources for Thin Film Deposition and Etching*, Francombe, M. H.; Vossen, J. L., Eds. Academic Press, Inc.: San Diego, 1994; Vol. 18.

13. Yasuda, H.; Hirotsu, T., Distribution of polymer deposition in plasma polymerization. 1. Acetylene, ethylene, and effect of carrier gas. *J. Polym. Sci., Polym. Chem. Ed.* **1978,** 16, 229-241.

14. Bell, A. T., Fundamentals of plasma polymerization. *J. Macromol. Sci. Chem.* **1976,** A10, 369-381.

15. Flamm, D. L., Introduction to Plasma Chemistry. In *Plasma Etching: An Introduction*, Manos, D. M.; Flamm, D. L., Eds. Academic Press, Inc.: San Diego, 1989.

16. Agraharam, S.; Hess, D. W.; Kohl, P. A.; Bidstrup Allen, S. A., Comparison of plasma chemistries and structure-property relationships of fluorocarbon films deposited from octafluorocyclobutane and pentafluoroethane monomers. *J. Vac. Sci. Technol. B* **2001,** 19, 439-446.

17. Lee, C.; Graves, D. B.; Lieberman, M. A.; Hess, D. W., Global model of plasma chemistry in a high density oxygen discharge. *J. Electrochem. Soc.* **1994,** 141, 1546-1555.

18. Woollam, J. A.; Snyder, P. G., Variable Angle Spectroscopic Ellipsometry. In *Encyclopedia of Materials Characterization*, Brundle, C. R.; Evans, C. A. J.; Wilson, S., Eds. Butterworth-Heinemann: Boston, 1992.

19. Tompkins, H. G.; McGahan, W. A., *Spectroscopic Ellipsometry and Reflectometry: A User's Guide*. John Wiley and Sons: New York, 1999.

20. Herzinger, C. M.; Johs, B.; McGahan, W. A.; Woollam, J. A.; Paulson, W., Ellipsometric determination of optical constants for silicon and thermally grown silicon dioxide via a multi-sample, multi-wavelength, multi-angle investigation. *J. Appl. Phys.* **1998,** 83, 3323-3336.

21. Bell, A. T., Fundamentals of Plasma Chemistry. In *Techniques & Applications of Plasma Chemistry*, Hollan, J. R.; Bell, A. T., Eds. Wiley: New York, 1974.

22. Jensen, R. J.; Bell, A. T.; Soong, D. S., Plasma polymerization of ethane. I. Experimental studies of effluent gas composition and polymer deposition rates *Plasma Chem. Plasma Process.* **1983,** 3, 139-161.

23. Yasuda, H., Glow Discharge Polymerization. In *Thin Film Processes*, Vossen, J.; Kern, W., Eds. Academic Publishing, Inc.: New York, 1978.

24. Jensen, R. J.; Bell, A. T.; Soong, D. S., Plasma polymerization of ethane. II. Theoretical analysis of effluent gas composition and polymer deposition rates *Plasma Chem. Plasma Process.* **1983,** 3, 163-192.

25. Chaudhari, S. K.; Patil, K. R.; Allepus, J.; Coronas, A., Measurement of the vapor pressure of 2,2,2-trifluoroethanol and tetraethylene glycol dimethyl ether by static method. *Fluid Phase Equil.* **1995,** 108, 159-165.

26. Yasuda, H.; Wang, C. R., Plasma polymerization investigated by the substrate temperature dependence. *J. Polym. Sci., Polym. Chem. Ed.* **1985,** 23, 87-106.

27. Casserly, T. B.; Gleason, K. K., Effect of substrate temperature on the plasma polymerization of poly(methyl methacrylate). *Chem. Vap. Deposition* **2006,** 12, 59-66.

28. Tamirisa, P. A.; Koskinen, J.; Hess, D. W., Plasma polymerized hydrogel thin films. *Thin Solid Films* **2006,** 515, 2618-2624.

29. Johnston, E. E.; Bryers, J. D.; Ratner, B. D., Plasma Deposition and Surface Characterization of Oligoglyme, Dioxane, and Crown Ether Nonfouling Films. *Langmuir* **2005,** 21, 870-881.

30. Pouchert, C. J., *The Aldrich Library of FT-IR Spectra*. 2nd ed.; Aldrich: Milwaukee, 1997.

31. Socrates, G., *Infrared and Raman Characteristic Group Frequencies: Tables and Charts*. 3rd ed.; John Wiley and Sons, Ltd.: New York, 2001.

32. Liqiong, H.; Qiang, C.; Yuanjing, G., PEO-like functional films' polymerization in RF-PECVD. *Plasma Sci. Tech.* **2006,** 8, 582-584.

33. Acikgoz, S.; Bilen, B.; Demir, M. M.; Menceloglu, Y. Z.; Skarlatos, Y.; Aktas, G.; Inci, M. N., Use of polyethylene glycol coatings for optical fibre humidity sensing. *Optical Review* **2008,** 15, 84-90.

34. Aminabhavi, T. M.; Banerjee, K., Density, viscosity, refractive index, and speed of sound in binary mixtures of methyl acetate + ethylene glycol or + poly(ethylene glycol) in the temperature interval (298.15-308.15) K. *J. Chem. Eng. Data* **1998,** 43, 852-855.

35. Zajickova, L.; Rudakowski, S.; Becker, H.-W.; Meyer, D.; Valtr, M.; Wiesemann, K., Study of plasma polymerization from acetylene in pulsed r.f. discharges. *Thin Solid Films* **2003,** 425, 72-84.

CHAPTER 4

DISSOLUTION AND SWELLING BEHAVIOR OF PLASMA-POLYMERIZED PEG THIN FILMS IN WATER

4.1 Introduction

One of the most important factors in the ability to effectively utilize plasma-deposited polymers as biomaterials and drug delivery materials is crosslink density, which controls overall film dissolution and swelling behavior. Previous studies[1] have indirectly monitored degree of crosslinking by determining the C/O ratio, as measured by x-ray photoelectron spectroscopy (XPS), of the plasma-deposited polymer formed from *n*-butyl methacrylate. This ratio was varied by manipulation of input power and ultimately allowed controlled release of an antibiotic molecule. More recent investigations[2] used contact angle measurements to monitor the extent of hydrophobization over time in air as a function of deposition pressure and input power. Looser crosslinked films experienced a greater freedom of movement as surface-oriented polar groups rotated into the bulk of the film. Other issues, including reaction of trapped free radicals in air-exposed films, were also considered when accounting for film properties. However, these previous studies did not investigate the swelling and water-based dissolution behavior of plasma-deposited hydrogel films. Water and moisture uptake has been studied,[3] however, using quartz crystal microbalance with dissipation for plasma-polymerized NIPAM films to demonstrate thermoresponsive swelling behavior as a function of plasma growth conditions.

An additional factor that may affect the integrity of crosslinked films and thus their barrier and swelling properties is the presence of particles imbedded within the film. This phenomena has generally been a crucial concern in the semiconductor industry[4-7] as

the critical dimensions of very large-scale integration (VLSI) circuits shrink in size. The growth of particles on the substrate and in the plasma vapor phase can lead to wafer contamination[8] and thus, the presence of pinhole-sized defects within the continuous phase of the film. Particle formation and existence in gaseous plasmas have been referred to as "dusty" plasmas and result in many cases from heterogeneous reaction and agglomeration[9] of reactive species in the vapor phase. While the powder formation mechanism is generally unknown, homogenous reactions are believed to play a significant role in some cases, e.g., pure RF silane plasmas.[9] Particle interactions within the plasma are related to number density and size and are established by various processing parameters such as pressure, plasma on time (in pulsed plasmas)[10] and power;[11] interactions are based primarily on particle charging. Nanometer-sized agglomerates grow as ions and electrons strike particle surfaces. Because the particles are electrically floating, the accumulated negative charge eventually increases to the point where additional negatively charged species are repelled, thereby stabilizing the particle. Electrostatic, gravitational and drag forces must be taken into account in order to fully explain particle behavior.[9] Argon-silane systems have been the most extensively studied and characterized,[11-13] primarily due to their applications in various hydrogenated amorphous silicon thin-film devices.

Much of the work to date[14-17] on particle incorporation in plasma polymerized films has focused on adhesion forces at the polymer-substrate interface or surface roughness. Further information, however, is needed in order to establish relationships between deposition conditions and film behavior in aqueous media. This chapter investigates these relationships by studying deposited film structure and how the presence of particles can be used as a possible explanation for film dissolution and swelling behavior.

4.2 Experimental Details

4.2.1 Plasma Deposition of PEG-Like Films onto Silicon Substrates

Swelling and dissolution studies conducted for this chapter required plasma-polymerized PEG-like films deposited onto a silicon substrate. Absolute starting thicknesses of the coatings prior to dissolution or swelling experiments did not play an important role because *percent* decrease or increase was monitored. Rather, deposition time was maintained at ten minutes. Deposition conditions are summarized in table 4.1.

Table 4.1. Experimental conditions of plasma films deposited for dissolution and swelling studies

Sample No.	Excitation Power (W)	Reactor Pressure (mTorr)	Substrate Temperature (°C)
1	55	1000	110
2	32	1400	95
3	32	1000	110
4	55	1400	110
5	32	1400	110
6	55	1200	110

4.2.2 Ellipsometry Analysis of PEG-Like Films

Film thicknesses for samples used in both dissolution and swelling studies were determined using a variable angle spectroscopic ellipsometer as detailed in Chapter 3. In-situ studies were performed in a continuous-flow ellipsometric cell at an incident angle of 65° where film samples were exposed to water vapor to maintain the chamber relative humidity at 75%. The experimental configuration is shown in figure 4.1. Nitrogen flow rate is controlled with a manual rotometer and is bubbled into a liquid water reservoir. Water vapor is generated and directed through flexible Tygon® tubing into the cell. Dynamic monitoring of thickness changes was performed using the Woollam EASE

program. Dry film thickness measurements were determined prior to water vapor introduction. After maximum swelling was attained, water vapor supply to the cell was terminated and residual moisture purged from the chamber. Drying occurred as trapped water molecules diffused out of the coating.

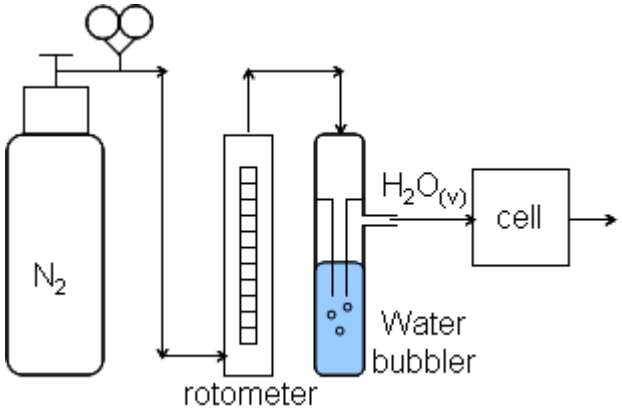

Figure 4.1. Schematic experimental configuration of water vapor introduction into an ellipsometric cell for swelling analysis of plasma-polymerized PEG-like films

4.2.3 Scanning Electron Microscopy (SEM) of PEG-Like Films

Direct measurement of particle size and density was conducted with a field-emission scanning electron microscope (FESEM; LEO 1530 FEG at 10 kV). Field-emission studies were performed in a vacuum of ~1.0×10^{-7} Torr at room temperature.

4.3 Results and Discussion

4.3.1 Dissolution Behavior of Plasma-Polymerized PEG-Like Films in Water

Spectroscopic ellipsometry was used to determine changes in film thickness upon exposure to water. These data offer an indication of how crosslink density is affected by deposition parameters. Figure 4.2 shows time-dependent thicknesses of films grown at various deposition conditions while table 4.2 summarizes their dissolution behavior. Clearly, variation of plasma processing conditions allows controlled degradation of the coatings in water. Consistent with the results shown in Chapter 3, it has been assumed

that the bonding chemistry of all six samples remains constant. SEM results in figure 4.3 indicate powder formation which may affect crosslink homogeneity or crosslink density. Polymer powder formation in plasmas has been previously studied using electron microscopy techniques,[18-20] but these investigations did not address how particle inclusion in deposited films affects crosslinking/swelling and dissolution properties.

4.3.1.1 Description of Film Dissolution Behavior

Films deposited in samples 1 and 2 represent the two extremes of dissolution behavior, with the samples deposited at higher powers, lower pressures and higher temperatures (sample 1) exhibiting a total thickness reduction of 9 percent after 49 days. In contrast, samples deposited at lower powers, higher pressures and lower temperatures (sample 2) almost completely dissolve after 18 days. In addition, the coatings in sample 2 decreased by ~15% of their as-deposited thickness after a 3-minute deionized (DI) water rinse. After the rinse, films were stored in water at room temperature and removed periodically to measure thickness. The more stable coatings (sample 1) decreased in thickness at an average rate of 0.5 nm/day versus the less stable coatings (sample 2), which decreased in thickness by ~11.5 nm/day.

Dissolution studies of samples 3-6 provided additional information into the mechanism of film degradation and helped explain film behavior at operating condition extremes (e.g. samples 1 and 2). For each of the deposition conditions investigated in samples 3-6, it can be seen (figs. 4.2(c)-(f)) that the films neither stabilize in thickness, as was observed for sample 1 (fig. 4.2(a)), nor dissolve completely (sample 2; fig. 4.2(b)). The time frame of exposure to water is detailed in column 3 of table 4.2. For the sampled time interval, the films either progressively increased in surface roughness to the point where ellipsometry no longer provided accurate thicknesses, or films began to delaminate from the silicon substrate. Time spans in table 4.2 are therefore the time over which the films remained intact with a sufficiently reflective surface to obtain meaningful

ellipsometry results. An alternate means of comparison is to use the lifetime of the least stable film as a standard and compare this value to the degree of dissolution experienced by other films over the same time interval. For the coatings tested, sample 2 completely dissolved in the shortest amount of time at 18 days; samples 3-6 dissolve between ~15-40% after 18 days. This establishes control of degree of film degradation that was achieved by varying deposition conditions and reaffirms that the deposition conditions for growth of films in samples 1 and 2 represent not only limitations of the reactor system, but also boundaries for film dissolution behavior of the PEG-like coatings.

The SEM images in figure 4.3 indicate the presence of particles embedded in the body of the as-deposited PEG-like films. With the exception of sample 2 (fig. 4.3(c)(d)), samples 1, 3-6 show relatively isolated and large particles that appear to range from ~600-1000 nm in size. Particle sizes correspond well with those reported in previous studies.[9 8, 10, 21] Contrary to previous reports,[21 8] particles were not uniform in shape, but rather displayed a combination of spherical and elliptical shapes. Particles from plasma processing originate either from gas phase nucleation (homogeneous growth) or from fragments of films that had been deposited on substrate or wall surfaces (heterogeneous growth).[8] Sample 2 shows a much higher particle count than that of the other samples with sizes reaching an upper limit of ~400 nm; from figure 4.3(c), it is observed that individual particles agglomerate. Previous reports of particle size with respect to time show that growth is nearly linear with time.[10] After a 3-minute rinse, particles contained in samples 2-5 were purged from the film while those in samples 1 and 6 remained relatively constant. Such observations can be attributed to the continuity of polymeric crosslinks within the more stable matrix, even when particles are present. A higher crosslink density reduces the ability to extract particles[22] since chain movement and thus accessibility of particles to water are constrained. Thus, electron microscopy can be invoked as an indirect technique that allows determination of relative crosslink density when comparing particle densities and particle counts of different samples.

The particles generate discontinuities within the film body; thus, the film volume taken up by the particle itself can be thought of as a "defect" that contributes to enhanced diffusion of penetrants via a defect-driven permeation mechanism.[23] Although surface area fraction of defects is small, lateral diffusion of water molecules is increased through tiny pinholes spaced closely together, as is the case in figure 4.3(c) for sample 2. Films of equivalent defect area combined into fewer, larger defects may provide a greater resistance to penetrants.[24 25] This relates well to the previous discussion on the continuity of crosslinks and how larger defects do not *necessarily* result in a greater permeation. Spacing is also an important consideration and is the reason for the difference in dissolution rates between samples 1 and 2. Defect-driven permeation through plasma deposited films has been previously investigated,[26 25, 27] where it was determined that particulate contamination was the cause of those defects.

4.3.1.2 Effect of Deposition Conditions on Particle Generation and Crosslink Density

Film dissolution behavior can be correlated with degree of crosslinking in the polymeric network. For instance, plasma conditions affect film bonding structure and crosslink density as described previously.[1, 2] Degree of crosslinking, or crosslink density, relates to network formation resulting from gas phase reactions between chemical fragments derived from electron impact collisions or between fragments and monomer species, and from surface reactions promoted by ion bombardment. Enhancement of surface reactions yields higher crosslink densities in the film although, as will be shown, increased particle formation in the vapor phase may lead to less stable, looser crosslinked coatings. Both surface and vapor phase reactions occur simultaneously and each plays a role in the eventual response behavior of the film. The impact of each is dictated by user-defined plasma processing conditions.

For a capacitively-coupled parallel-plate RF discharge, an increase in applied power leads to increased electron density, higher collision rates, increased ionic and

radical species concentrations, and therefore enhanced radical, ion and electron bombardment flux to the substrate.[28] Thus, for constant operating pressures and substrate temperatures, higher applied powers theoretically should yield a more highly crosslinked, stable film. An example of this can be seen by comparing samples 1 (55 W) and 3 (32 W) at a pressure of 1000 mTorr and a substrate temperature of 110°C. Sample 1 experienced a much smaller total percent decrease in thickness (9% versus 46% for sample 3) over an extended time frame (49 days versus 22 days for sample 3) resulting in a reduced dissolution rate (0.5 nm/day versus 3.4 nm/day for sample 3). From the SEM images in figure 4.3, we see that for both samples 1 and 3, large, irregularly-shaped particles are incorporated into the film during the deposition process. It has been determined[8] that for lower RF power, particles are generated by reactions both in the gas-phase and at the surface. Thus, the particles obtained at the low RF power are not as uniform in size as those obtained at the high RF power. Because particles are not spherically uniform at either input power (32 or 55 W), we believe that the input powers are low enough to initiate particle growth at the substrate surface. Although SEM is a surface analysis technique, particles observed on the film surface should be representative of particles trapped in the bulk because vapor phase powder formation and surface bombardment are both continuous processes. Figures 4.3(a) and (e) show the presence of particles on the as-deposited films for samples 1 and 3, respectively, while 4.3(b) and (f) show film surfaces after a 3-minute DI water rinse. There is no change in thickness of the coating for sample 1 before and after the rinse; however, a thickness decrease of 15 nm is measured for sample 3. Since particle size and count are essentially equivalent in the imaged areas, we conclude that the crosslink density establishes the ability to remove particles during the DI water rinse. That is, at higher crosslink densities, the film possesses a greater ability to retain entrapped particles and will dissolve more slowly.

Deposition pressure also affects the average electron energy and the mean free path of molecules. At lower pressures, fewer collisions occur in the gas phase due to the

reduced gas number density and the average electron energy increases. Thus, lower pressures result in increased ion and electron energies impinging on substrate and growing film surfaces.[29] Films grown at lower pressures will have a greater crosslink density and increased stability to dissolution. Dissolution as a function of pressure is evident from comparison of samples 1 (1000 mTorr), 4 (1400 mTorr), and 6 (1200 mTorr) at constant input power (55 W) and substrate temperature (110°C). From table 4.2, we observe that as pressure increases, the total percent dissolution also increases (sample 1: 9%, sample 6: 33%, sample 4: 52%) even as dissolution time remains essentially constant (sample 1: 49 days, sample 6: 42 days, sample 4: 42 days). Dissolution rate steadily increases from 0.5 nm/day for sample 1 to 2.2 nm/day for sample 6 to 3.3 nm/day for sample 4. SEM results demonstrate particle inclusion for each of three samples, although after the DI water rinse, particles have been removed only in sample 4, which corresponds to the greatest decrease in film thickness (~10 nm). All particles detected were approximately the same size, contrary to previous studies[8] where as operating pressures increased, the diameters of the spherical nanoparticles decreased. The large particles of irregular size and shape obtained in this analysis at pressures ranging from 1000-1400 mTorr, were formed by increased inelastic collisions and aggregation of nucleation sites.[8]

Substrate temperature was the third parameter investigated for its effects on dissolution and crosslink density. At higher substrate temperatures, deposition rates decrease, thereby enhancing adsorbed fragment mobility and allowing more time for chemical reaction and bond rearrangement (promoted by ion bombardment) before adsorption of an additional polymer layer.[29] Film samples 2 and 5 were deposited at substrate temperatures of 95°C and 110°C, respectively, at constant power (32 W) and pressure (1400 mTorr). As expected, at higher temperatures, the dissolution rate of sample 5 (2.1 nm/day) was much slower than for sample 2, which stabilized at an average of ~11.5 nm/day. Dissolution of sample 2 was almost complete after 18 days while

sample 5 lost approximately one-third of its original thickness after 30 days. It has been demonstrated[8, 22, 30] that the slower dissolution rate that results from higher substrate temperatures can be attributed to an increase in crosslink density and film densification; this effect explains the dissolution rate results for sample 5. Further evidence is seen in the SEM images comparing sample 2 (figs. 4.3 (c)(d)) with sample 5 (figs. 4.3 (i)(j)). As reported previously,[8] as substrate temperature increases (95 → 110°C), particle counts and size decrease. At higher substrate temperatures surface mobility and diffusion length of the deposited species increases, thus encouraging surface rearrangements and resulting in denser films with well-defined surface morphologies. Furthermore, an increase in substrate temperature reduces the probability for nucleation, causing delays in the appearance of the particles.[30]

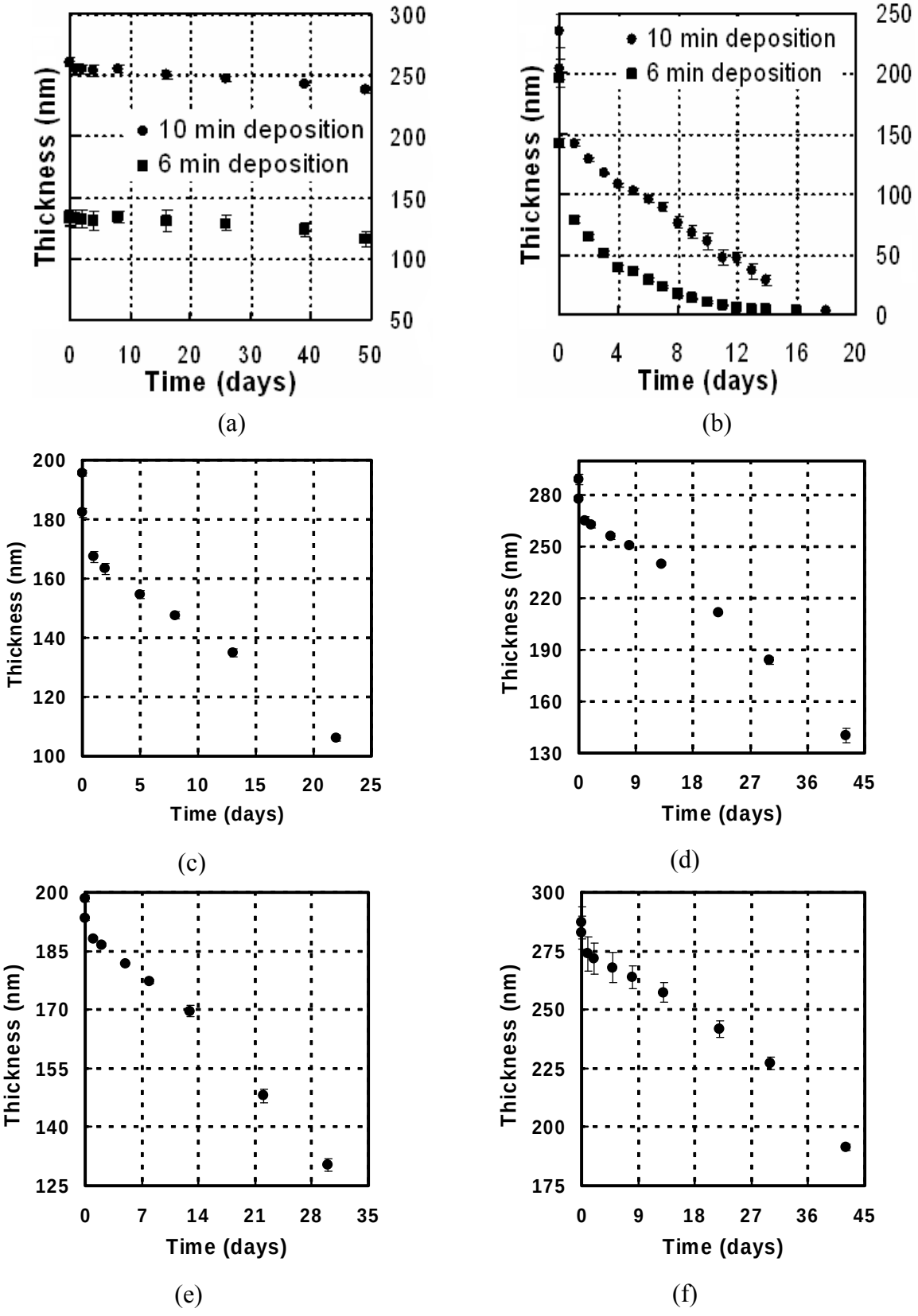

Figure 4.2. Dissolution stability comparison of films: (a) Sample 1, (b) Sample 2, (c) Sample 3, (d) Sample 4, (e) Sample 5, (f) Sample 6

Table 4.2. Dissolution and swelling behavior of plasma polymer PEG-like coatings deposited under various conditions

Sample No.	Total Percent Dissolution	Days	Dissolution Rate (nm/day)	Percent Dissolved After 18 Days	Percent Swelling
1	9	49	0.5	4	14
2	98	18	11.5	98	69
3	46	22	3.4	38	23
4	52	42	3.3	22	22
5	34	30	2.1	21	21
6	33	42	2.2	14	9

(a)

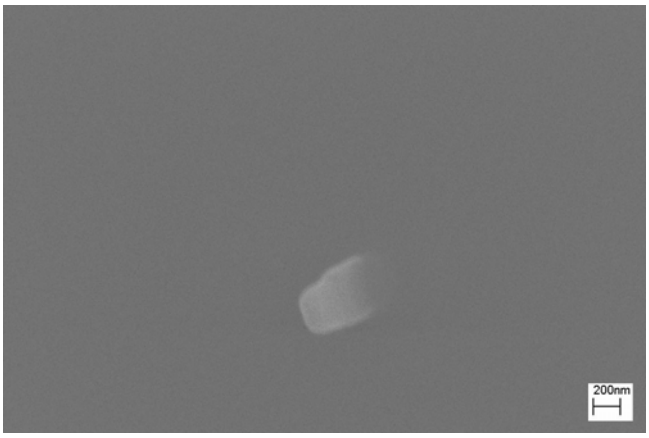

(b)

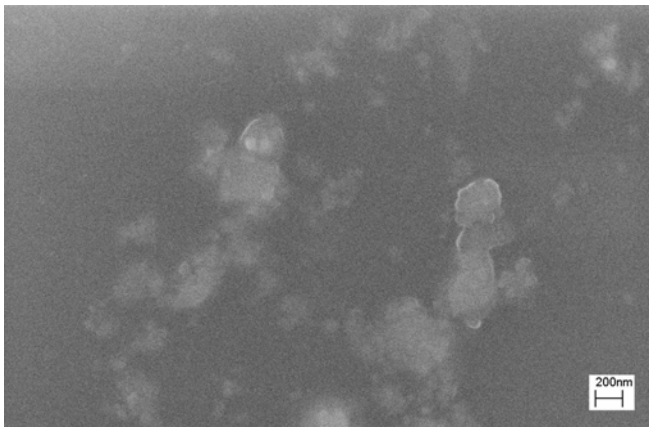

(c)

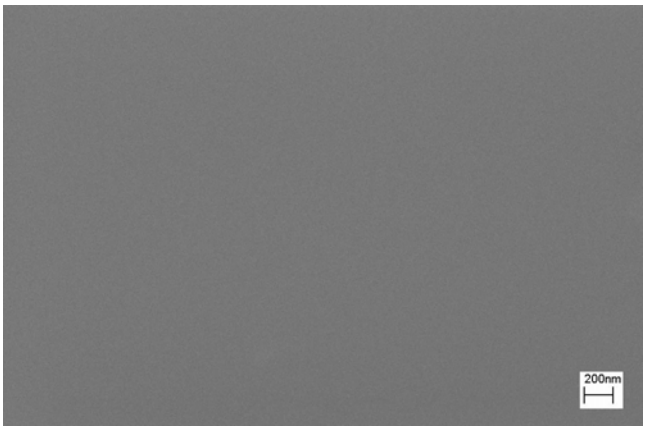

(d)

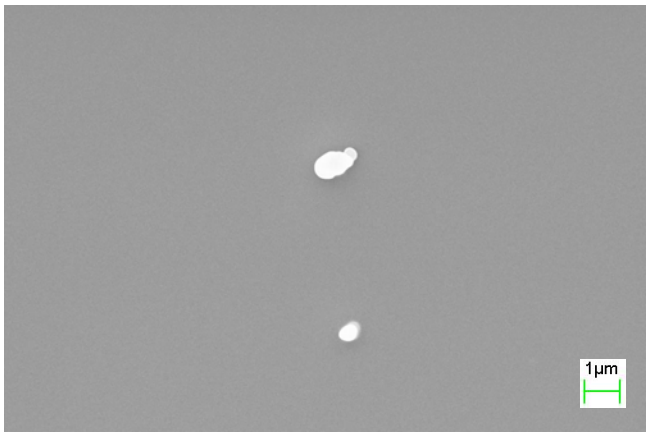

(e)

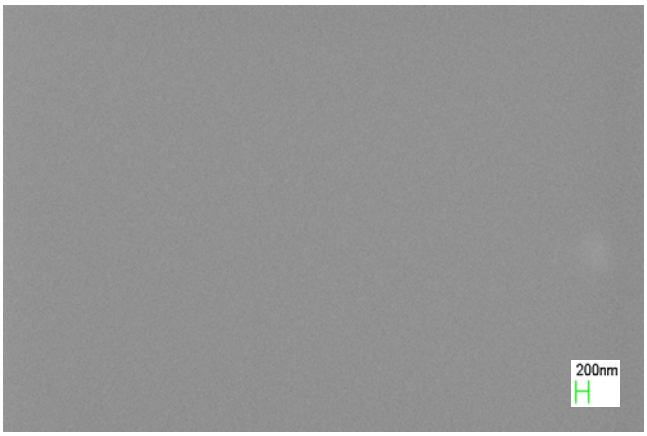

(f)

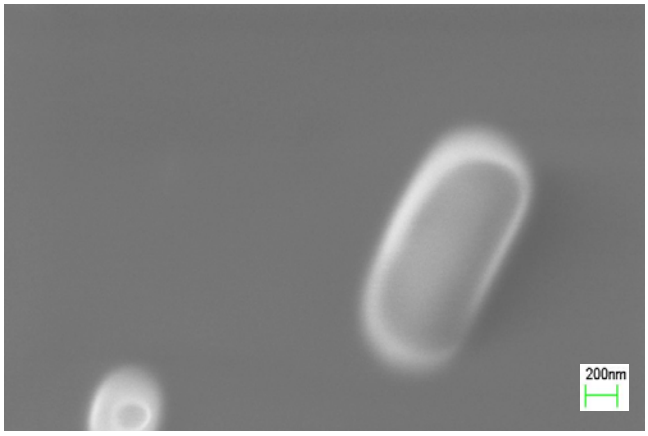

(g)

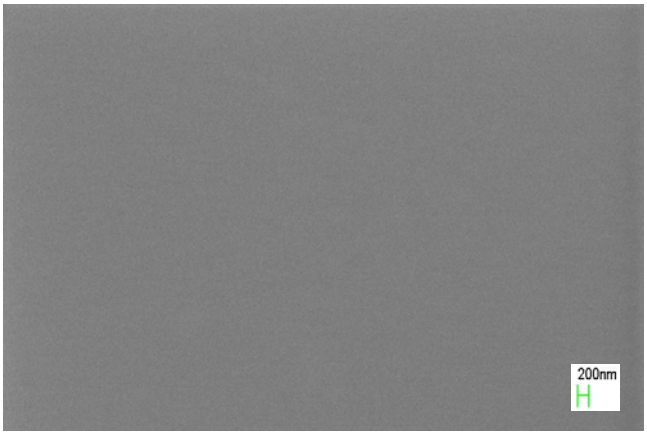

(h)

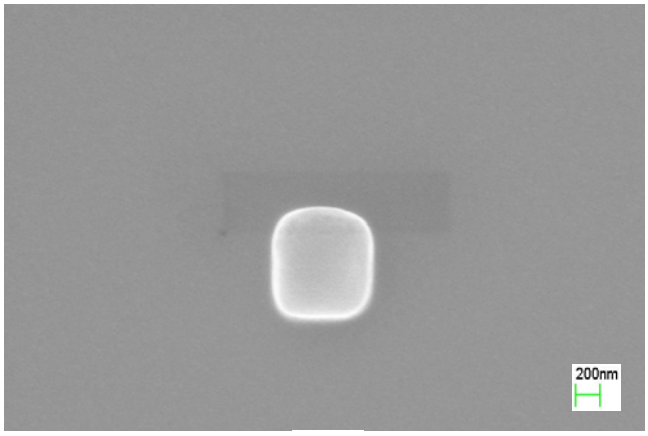

(i)

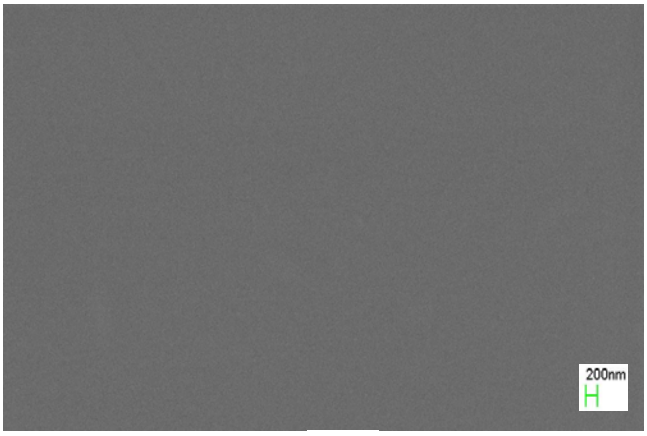

(j)

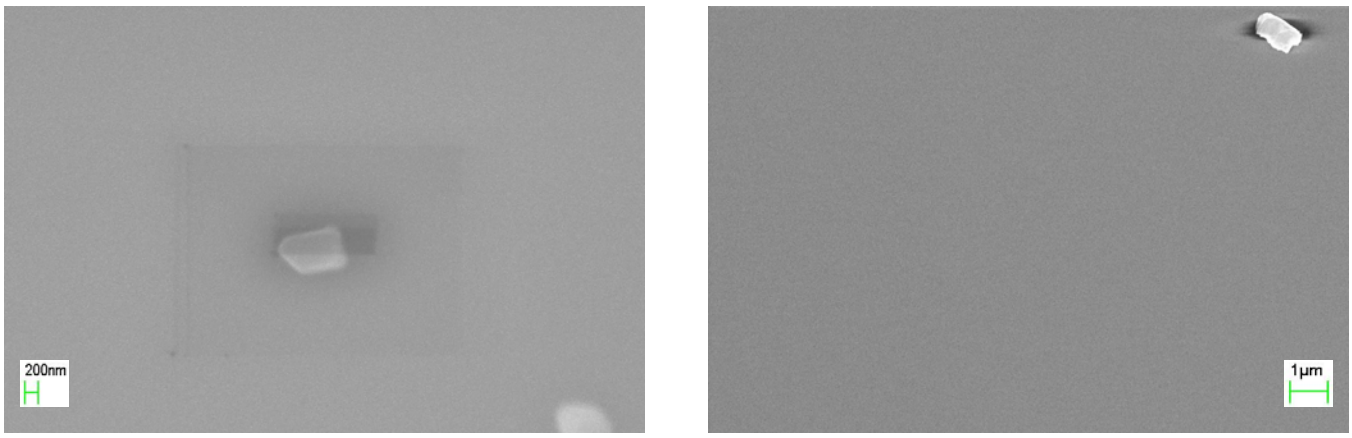

(k) (l)

Figure 4.3. SEM images profiling powder formation in plasma-polymerized PEG-like coatings, **Sample 1:** (a) as deposited; ~260 nm (b) after 3-minute deionized (DI) water rinse; ~260 nm, **Sample 2:** (c) as deposited; ~245 nm (d) after 3-minute DI water rinse; ~210 nm, **Sample 3:** (e) as deposited; ~195 nm (f) after a 3-minute DI water rinse; ~180 nm, **Sample 4:** (g) as deposited; ~290 nm (h) after a 3-minute DI water rinse; ~280 nm, **Sample 5:** (i) as deposited; ~200 nm (j) after a 3-minute DI water rinse; ~195 nm, **Sample 6:** (k) as deposited; ~290 nm (l) after a 3-minute DI water rinse; ~285 nm

4.3.2 Water Vapor Swelling of Plasma-Polymerized PEG-Like Films in Water

Extent of swelling for plasma-polymerized films is also a function of the accessibility of penetrants to pores or defects within the polymer matrix. That is, the amount of swelling is an indication of the ability of water to permeate the crosslinked polymer network. Water vapor is used in a continuous flow system to capture the difference in rate of material entry versus rate of diffusion out of the polymer matrix. Figure 4.4 shows the degree of water vapor uptake of the films deposited at the conditions summarized in table 4.1. Percent swelling for each sample in figure 4.4 is indicated in table 4.2. Swelling for the PEG-like films ranged from 10-15% for the more heavily crosslinked films (figs. 4.4(a),(e)) to almost 70% for the looser crosslinked coatings (fig. 4.4(b)). For the samples in figure 4.4, swelling is a rapid response to water vapor introduction, with the greatest increase observed within the first 10-15 minutes followed by a slower, gradual increase until an equilibrium thickness is attained. After

water vapor flow has been terminated, the drying process was displayed as an exponential decay occurring over a period of >50 minutes. Swelling is a complimentary film property to dissolution in that the more susceptible a film is to degradation, the more water it is able to uptake. These results are an indication that both properties are controlled by both the presence of defects created by powder formation and crosslink density, which can be manipulated by varying plasma processing conditions.

Previous studies[31, 32] of plasma polymerized films formed from ethylene glycol monomethyl ether monomers have correlated the water permeation coefficient with the ratio of power applied (W) to the product of monomer flow rate (F) and molecular weight (M), or so-called *W/FM* values;[33] this ratio offers a semi-quantitative value of the power supplied per unit of monomer material. Permeation coefficients have been reported to decrease as *W/FM* increases[32] at constant deposition pressure (1.3 Pa). For the reactor system in which our films were deposited, flow of monomer into the chamber is based on pressure gradients between the reaction chamber and the container flask housing the TGDE. A higher operating pressure decreased the flow rate of precursor from the source flask, which increased the *W/FM* ratio and reduced the permeation coefficient, or percent swelling. In other words, based on previous results,[32] a higher operating pressure should limit film swelling at constant power and monomer introduction. Comparing samples 1, 6, and 4, we see that as pressure is increased, percent swelling does not follow the trend established by Inagaki, although swelling at 1400 mTorr is greater than 1000 mTorr (22% for sample 4 at 1400 mTorr versus 14% for sample 1 at 1000 mTorr).

From our data, it can be reasonably assumed that there is an additional contributing factor which plays a role in film swelling. As previously discussed for dissolution behavior, particles, or defects, create disconnects within the bulk of the coating by occupying a volume of space that would otherwise be a section of the crosslinked film. Chains have a greater range of motion due to their looser crosslinked structure and may accept a greater amount of penetrant species. Earlier studies[34] confirm

this behavior, since those studies indicate that particles can also contribute to the increased diffusivity of water molecules due to an inhomogeneous film crosslink density and thus decreased tortuosity for the penetrant.

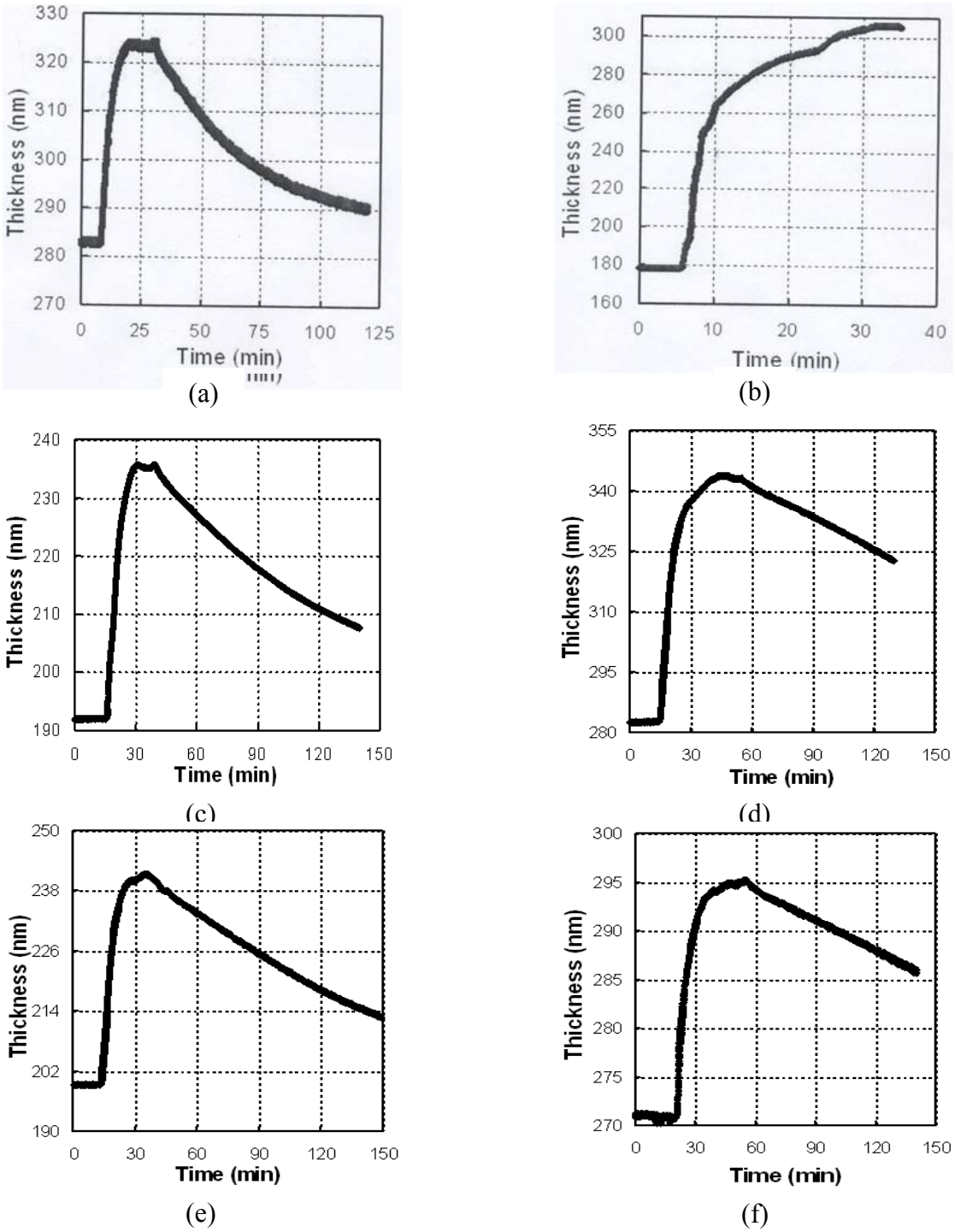

Figure 4.4. In-situ ellipsometry tracking dynamic swelling behavior of films: (a) Sample 1, (b) Sample 2, (c) Sample 3, (d) Sample 4, (e) Sample 5, (f) Sample 6

4.4 Conclusions

In this chapter, the relationship between dissolution and swelling behavior of plasma-polymerized polyethylene glycol-like films and deposition conditions was examined. Time-dependent dissolution investigations were conducted to study how the variation of plasma parameters affected powder formation and how this, in turn, created a discontinuity in film crosslink density. At constant operating pressures and substrate temperatures, higher applied powers yield a greater crosslinked, more stable film due to an increased electron density, higher collision rates, increased ionic and radical species concentrations, and an enhanced ion and electron bombardment flux. The irregularly-shaped particles entrapped within the film are partially due to nucleation and growth on the substrate and wall surfaces (heterogeneous growth) and gas phase nucleation (homogeneous growth). Higher crosslinked films have a greater ability to retain entrapped species and dissolve more slowly. Films grown at lower pressures will have a greater crosslink density and increased stability to dissolution because of fewer collisions in the gas phase and an increase in average electron and ion energy when impinging on the growing film. Substrate temperature was investigated for its effects on dissolution and crosslink density. At higher substrate temperatures, the dissolution rate was slower due to an increase in crosslink density and thus an expected increase in film density. As deposition rates decrease, surface mobility of an adsorbed fragment will increase, thereby allowing more time for chemical reaction and bond rearrangement (promoted by ion bombardment) before adsorption and bonding of an additional polymer layer.

Water vapor swelling studies were conducted using in-situ ellipsometry that dynamically measured film thickness with time. Extent of swelling for plasma-polymerized films is also a function of crosslink density. The majority of swelling occurs within the first 10-15 minutes of vapor introduction followed by a gradual increase in

thickness until equilibrium is attained. Drying occurs via an exponential decay over an extended time period. Particles can contribute to an increased diffusivity of water molecules due to an inhomogeneous film crosslink density and thus decreased tortuosity for the penetrant. Defects must be considered for their size *and* spacing to understand how they affect the penetrating ability of water molecules into the plasma film. For defects located close together, small molecules like water can laterally diffuse from pore-to-pore, resulting in either dissolution or swelling, depending upon the method of water introduction. If the defects are spaced too far apart, the film acts as an improved barrier to water penetration.

4.5 References

1. Kwok, C. S.; Horbett, T. A.; Ratner, B. D., Design of Infection-Resistant Antibiotic-Releasing Polymers II. Controlled Release of Antibiotics Through a Plasma-Deposited Thin Film Barrier. *J. of Controll. Relea.* **1999,** 62, 301-311.

2. Dorfman, A. M.; Lyakhovich, A. M.; Povstugar, V. I.; Bystrov, S. G., Influence of the plasma treatment regimes on the surface morphology and properties of films applied to steel from heptane plasma. *Protection of Materials* **2003,** 39, (1), 63-70.

3. Tamirisa, P. A.; Hess, D. W., Water and moisture uptake by plasma polymerized thermoresponsive hydrogel films. *Macromolecules* **2006,** 39, 7092-7097.

4. Selwyn, G. S.; Heidenreich, J. E.; Haller, K. L., Particle trapping phenomena in radio frequency plasmas. *Appl. Phys. Lett.* **1990,** 57, 1876-1878.

5. Selwyn, G. S., Plasma particulate contamination control. I. Transport and process effects. *J. Vac. Sci. Technol. B* **1991,** 9, 3487-3492.

6. Raoux, S.; Cheung, D.; Fodor, M.; Taylor, W. N.; Fairbairn, K., Growth, trapping and abatement of dielectric particles in PECVD systems. *Plasma Sources Sci. Technol.* **1997,** 6, 405-414.

7. Garscadden, A.; Ganguly, B. N.; Haaland, P. D.; Williams, J., Overview of growth and behaviour of clusters and particles in plasmas. *Plasma Sources Sci. Technol.* **1994,** 3, 239-245.

8. Fu, G. D.; Kang, E. T.; Neoh, K. G., Deposition of nanostructured fluoropolymer films on silicon substrates via plasma polymerization of allylpentafluorobenzene. *J. Phys. Chem. B* **2003,** 107, 13902-13910.

9. Hollenstein, C., The physics and chemistry of dusty plasmas. *Plasma Phys. Control. Fusion* **2000,** 42, R93-R104.

10. Boufendi, L.; Plain, A.; Blondeau, J. P.; Bouchoule, A.; Laure, C.; Toogood, M., Measurements of particle size kinetics from nanometer to micrometer scale in a low-pressure argon-silane radio-frequency discharge. *Appl. Phys. Lett.* **1992,** 60, 169-171.

11. Chaudhuri, P.; Gupta, N. D.; Bhaduri, A.; Longeaud, C.; Vignoli, S.; Marty, O., Powder evolution at low powers in silane-argon discharge. *J. Appl. Phys.* **2005,** 98, 044913(1-7).

12. Howling, A. A.; Sansonnens, L.; Dorier, J.-L.; Hollenstein, C., Time-resolved measurements of highly polymerized negative ions in radio frequency silane plasma deposition experiments. *J. Appl. Phys.* **1994,** 75, 1340-1353.

13. Stoffels, E.; Stoffels, W. W.; Kroesen, G. M. W.; de Hoog, F. J., Dust formation and charging in an Ar/SiH4 radio-frequency discharge. *J. Vac. Sci. Technol. A* **1996,** 14, 556-561.

14. Michaeli, W.; Fonteiner, I.; Goebel, S., Characterization of the layer growth of plasma-polymerized HMDSO coatings on polycarbonate. *Macromol. Mater. Eng.* **2000,** 284/285, 30-34.

15. Shirtcliffe, N.; Thiemann, P.; Stratmann, M.; Grundmeier, G., Chemical structure and morphology of thin, organo-silicon plasma-polymer films as a function of process parameters. *Surface and Coatings Technology* **2001,** 142-144, 1121-1128.

16. Grundmeier, G.; Thiemann, P.; Carpentier, J.; Shirtcliffe, N.; Stratmann, M., Tailoring of the morphology and chemical composition of thin organosilane microwave plasma polymer layers on metal substrates. *Thin Solid Films* **2004,** 446, 61-71.

17. Teare, D. O. H.; Spanos, C. G.; Ridley, P.; Kinmond, E. J.; Roucoules, V.; Badyal, J. P. S., Pulsed plasma deposition of super-hydrophobic nanospheres. *Chem. Mater.* **2002,** 14, 4566-4571.

18. Thompson, L. F.; Smolinsky, G., A scanning electron microscope study of plasma-polymerized organosilicon films suitable for use as lightguides. A determination of the cause of signal attenuation. *J. Appl. Polym. Sci.* **1972,** 16, 1179-1190.

19. Liepins, R.; Sakaoku, K., Submicron polymer powder in electrodeless radio frequency-induced plasma-initiated polymerization. *J. Appl. Polym. Sci.* **1972,** 16, 2633-2645.

20. Havens, M. R.; Mayhan, K. G.; James, W. J., Plasma-deposited polymer films. II. Transmission and scanning electron microscopy. *J. Appl. Polym. Sci.* **1978,** 22, 2799-2804.

21. Berndt, J.; Hong, S.; Kovacevic, E.; Stefanovic, I.; Winter, J., Dust particle formation in low pressure Ar/CH_4 and Ar/C_2H_2 discharges used for thin film deposition. *Vacuum* **2003,** 71, 377-390.

22. Doblhofer, K.; Durr, W.; Jauch, M., Electrochemical redox response of iron (II)/(III) ions implanted in permeable, polymeric electrode coatings. *Electrochimica Acta* **1982,** 27, 677-682.

23. Lewis, J. S.; Weaver, M. S., Thin-film permeation-barrier technology for flexible organic light-emitting devices. *IEEE J. Selec. Topics Quan. Elec.* **2004,** 10, 45-57.

24. Rossi, G.; Nulman, M., Effect of local flaws in polymeric permeation reducing barriers. *J. Appl. Phys.* **1993,** 74, 5471-5475.

25. Hanika, M.; Langowski, H.-C.; Moosheimer, U.; Peukert, W., Inorganic layers on polymeric films—Influence of defects and morphology on barrier properties. *Chem. Eng. Technol.* **2003,** 26, 605-614.

26. Chatham, H., Oxygen diffusion barrier properties of transparent oxide coatings on polymeric substrates. *Surf. Coat. Technol.* **1996,** 78, 1-9.

27. da Silva Sobrinho, A. S.; Czeremuszkin, G.; Latreche, M.; Wertheimer, M. R., Defect-permeation correlation for ultrathin transparent barrier coatings on polymers. *J. Vac. Sci. Technol. A* **2000,** 18, 149-157.

28. Bell, A. T., Fundamentals of Plasma Chemistry. In *Techniques & Applications of Plasma Chemistry*, Hollan, J. R.; Bell, A. T., Eds. Wiley: New York, 1974.

29. Morosoff, N., An Introduction to Plasma Polymerization. In *Plasma Deposition, Treatment, and Etching of Polymers*, d'Agostino, R., Ed. Academic Press, Inc.: San Diego, 1990.

30. Hadjadj, A.; Beorchia, A.; Cabarrocas, P. R.; Boufendi, L.; Huet, S.; Bubendorff, J. F., Effects of the substrate temperature on the growth and properties of hydrogenated nanostructured silicon thin films. *J. Phys. D: Appl. Phys* **2001,** 34, 690-699.

31. Inagaki, N.; Oh-Ishi, K., Preparation of amino group-containing polymers by plasma polymerization. *J. Polym. Sci., Polym. Chem. Ed.* **1985,** 23, 1445-1454.

32. Inagaki, N.; Kubokawa, Y., Plasma polymerization of ethylene glycol monomethylether and water-vapor permeability. *J. Polym. Sci. Polym. Chem. Ed.* **1989,** 27, 795-805.

33. Yasuda, H., Glow-discharge polymerization. *J. Polym. Sci. Macromol. Revs.* **1981,** 16, 199-293.

34. Tuzov, L. S.; Adonin, S. P.; Chuvileva, G. G.; Shurov, A. N.; Kolotyrkin, A. M., Water diffusion through polymeric films, prepared in a glow-discharge plasma. *Zh. Fiz. Khim.* **1978,** 52, 727-729.

CHAPTER 5

PORE SIZE DETERMINATION OF PLASMA-POLYMERIZED POLYETHYLENE GLYCOL-LIKE FILMS

5.1 Introduction

Pore size determination of polymer thin films has been widely investigated[1-4] as a means to control incorporation of potential drug molecules and to study film release behavior. It has been determined[4] that for the incorporation of proteins into alginate-based drug reservoirs, the loading characteristics of the system are dependent on the protein size as well as the pore sizes of the gel. Release kinetics of proteins via either diffusion or film degradation was attributed to crosslink density.[4] Release of species, specifically through diffusion, is dependent on the swelled-state pore size of the polymer matrix. The manipulation of pore sizes of hydrogel membranes synthesized from acrylic acid/acrylamide-based monomer mixtures has been previously investigated[1] to understand how chemical composition affects degree of swelling. It was found that pore sizes of the swelled-state polymer increase with the addition of hydrophilic acrylic acid groups, thereby increasing the diffusion coefficients of potential release molecules.[1]

Control of pore sizes in polymer thin films has also played important roles in engineering barrier layers in the microelectronics[5] and food and pharmaceutical packaging industries[6] as well as in organic light-emitting devices.[7] Diffusion of copper from interconnects into polymer dielectric layers has been problematic in the semiconductor industry and much research has focused on barrier layers as a means to inhibit transport. Plasma-deposited fluorocarbon films have been extensively investigated for this purpose[8] using RF[9, 10] and ECR pulsed-plasma sources.[11 12] These films have superior physical properties relative to those of conventional polymer films

with tunable carbon-to-fluorine ratios dictated by deposition conditions. Varying this ratio allows manipulation of crosslinking and presumably, pore sizes through the bulk.[8] Oxygen permeation in food and pharmaceutical applications can be reduced using highly crosslinked plasma-deposited polymer films,[6] although at best only up to 2-3 orders of magnitude improvement has been observed, apparently due to defects or pores through the body of the film. Studies indicate that both pore/defect size and spacing are instrumental in establishing overall barrier performance. If the size of the defect is small, but closely spaced with adjacent defects, the lateral diffusion of the penetrant is much greater than for large defects spaced further apart.[13, 14] Several studies have shown the correlation between permeation rate of small molecules and defect density; oxygen has been shown to diffuse through a substrate, regardless of coating material or deposition technique.[15, 16]

Dendrimers are hyperbranched, monodispersed three-dimensional molecules with well-defined molecular weights and nanoscale length scales. Starting with a central core of at least two functional groups, dendrimers grow with addition of repeated branch units and terminate with user-defined surface functional groups. Since their introduction in the mid-1980s,[17] dendrimers have gained recognition in various applications.[18-20] Of particular interest is their suitability for biomedical applications such as drug delivery vehicles.[21, 22] By the nature of their construction via either the divergent or convergent pathway, they can be controlled to have specific interactions between the guest drug molecule and host dendrimer.[23] In this chapter, dendrimers are used because of their precise size characteristics and surface functionalization ability to probe pore sizes of plasma-polymerized PEG-like coatings. An understanding of how critical size dimensions affect incorporation of the dendrimers into PEG-like coatings will also indicate other possible drug molecules that can be delivered using the specific hydrogel layers described in previous chapters. In addition, dendrimers themselves can be used as carriers of drug agents in physiological systems.[21]

Poly(amidoamine) (PAMAM) dendrimers are biocompatible, commercially-available and most widely used in biomedical applications.[24] Synthesis of PAMAM dendrimers has been described previously[17] and involves a cycling Michael addition of methyl acrylate and amidation from excess ammonia or ethylenediamine beginning with an ethylenediamine core. Each cycle adds another layer of amine-terminated end-groups and forms a successively larger shell around the ethylenediamine core; this is referred to as a 'generation'. Surface functionalization is important for dendrimer solubility, reactivity and transport properties through the delivery medium.[25] Lower generations (G0-G3) of this dendrimer class are elliptical in their nano-shape while higher generations (G4-G10) are more spherical.[26] Molecular simulation studies[27] suggest that although dendrimers can generally be thought of as globular, their shape is dynamic in aqueous environments with the presence of external stimuli such as salt concentration or pH. Changes have been interpreted as conformational shifts in mass from a dense core to a dense shell.

Recently, much interest has been focused on the molecular tracking of fluorescently-labeled PAMAM dendrimers[28, 29] and their potential applications as delivery systems[30, 31] and chemosensing materials.[32, 33] Covalent conjugation of PAMAM dendrimers have employed a wide variety of fluorophores including Oregon Green® 488,[30] fluorescein,[34, 35] and cyanine dye.[29] Characterization of the resultant fluorophore-dendrimer conjugate has been previously studied using thin layer chromatography[30] and absorption spectroscopy,[29] although recent studies using matrix-assisted laser desorption-ionization (MALDI) on PAMAM dendrimers[36] suggest an alternative route to detection of fluorophore-dendrimer conjugation. MALDI was used to determine structural inconsistencies of fan-shaped, generations 0-3, tri(ethylene glycol)-derived, PAMAM dendrimers. It was determined[36] that for lower order generations, defects are built into the dendrimer during synthesis and that these defects are able to propagate as dendrimer generation increases. MALDI detects the structural inconsistencies through molecular

weight comparisons of ionic species between fan-shaped synthesized dendrimers and standard commercially available PAMAM dendrimers.

Dendrimers containing a charged surface group have been previously investigated[37-39] using gel electrophoresis for insight into separation processes that enhance dendrimer purity and homogeneity. Additional gel electrophoresis studies have been conducted to understand the role of surface charge in the interaction between PAMAM dendrimers and biological molecules.[40] Due to their well-defined sizes and negatively-charged surface groups, we use succinamic acid surface functionalized PAMAM dendrimers with attached fluorescent dye to examine void space sizes of swelled-state plasma-polymerized PEG-like films. Such information generates insight into the ability of plasma-polymerized PEG-like films to uptake and release drug molecules. Furthermore, with the application of an electric field, molecules experience an electrophoretic drift which enhances their penetration into the bulk of the film. Previous studies using anionic PAMAM dendrimers have been performed to determine their transepithelial diffusion transport properties through sub-10 nm diameter pores for oral drug delivery applications.[25, 41, 42] In this chapter, we use electromotive and concentration (diffusion) driving forces to investigate the effect of dendrimer size in the immobilization of anionic molecules in swelled-state plasma polymer coatings.

5.2 Experimental Details

Pore size openings of swelled-state plasma-polymerized polyethylene glycol-like coatings were characterized with fluorescently-labeled poly(amidoamine) (PAMAM) dendrimers. Matrix-assisted laser desorption-ionization (MALDI) mass spectroscopy was used to affirm the association between the fluorescent marker and dendrimer. Transport of the fluorophore-dendrimer conjugate into the film was by either diffusion or electrophoretic drift. The resistance of molecule penetration was investigated as a function of dendrimer size and transport mechanism by fluorescence microscopy.

5.2.1 Plasma Deposition of PEG-Like Films onto Conducting Surfaces

For the pore size determination studies conducted in this work, plasma-polymerized PEG-like films were deposited onto conducting gold-coated (~200 nm) silicon substrates; a thin titanium layer (~20 nm) ensured proper adhesion between gold and silicon. PEG-like films were deposited at an input power of 55 W, an operating pressure of 1000 mTorr and a substrate temperature of 110°C. A contact point to the bare gold surface was established by touching a probe to an area of the substrate where a small piece of silicon wafer had been placed during plasma deposition, thereby protecting that region from deposited film. For fluorescence microscopy analysis of samples after immobilization, PEG-like films with a thickness of ~700 nm were used.

5.2.2 Preparation of the Fluorophore-Dendrimer Conjugate

The fluorophore-dendrimer conjugate was prepared by reacting Alexa Fluor® 488 cadaverine (Invitrogen Corp.) with succinamic acid PAMAM dendrimers purchased from Dendritic Nanotechnologies, Inc. Figures 5.1 and 5.2 show the structures of the fluorophore and PAMAM dendrimer, respectively.

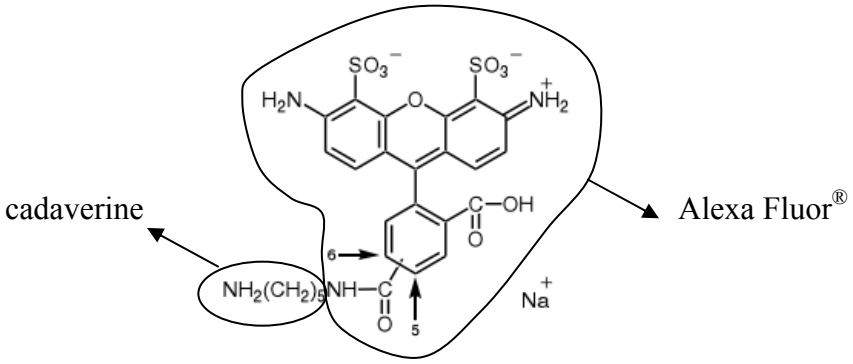

Figure 5.1. Chemical structure of Alexa Fluor® 488 cadaverine, sodium salt

Generation 2 (G2), generation 5 (G5), and generation 6 (G6) PAMAM dendrimers were used in separate labeling synthesis procedures; their physical properties are shown in table 5.1. All dendrimers contained a diaminobutane core and were dissolved in water solvent with a dendrimer concentration of 10 wt.%. Prepared PAMAM dendrimer

solutions were monodisperse (polydispersity index < 1.01), meaning that there were fewer impurities, with precise surface numbers and structures. The Alexa Fluor® 488 fluorescent dye is often used for labeling because of its relatively small size and water solubility. It has absorption and emission maxima at ~495 nm and 519 nm, respectively.

A zero-length crosslinker is used to aid the reaction between the primary amine group on the cadaverine group of the fluorophore with the carboxylic acid termination of the dendrimer.[43] Figure 5.3 shows the crosslinker chemical structure of the 1-ethyl-3-(3-dimethylaminopropyl)carbodiimide hydrochloride (EDAC) as purchased from Sigma Aldrich. EDAC is a water soluble carbodiimide that reacts with carboxylic acids to form reactive *o*-acylisourea intermediates which can then be attacked by primary amines to form an amide bond.

Stock solutions of the fluorophore and crosslinker were prepared having concentrations of 3.90×10^{-3} M and 2.61×10^{-1} M, respectively. The G2 dendrimer stock solution was 2.08×10^{-2} M, the G5 dendrimer stock solution was 2.41×10^{-3} M, and the G6 dendrimer stock was 1.20×10^{-3} M. Solutions were prepared in deionized water with a final EDAC molecule-to-dendrimer surface group ratio of 6-to-1 in the first part of the synthesis and a fluorophore molecule-to-dendrimer surface group ratio of 4-to-1 after the fluorophore was added. The mixture was reacted for two hours at room temperature and purified by dialysis.[43] Prior to reaction, the mixture is a yellow-green solution; after two hours reaction, the color of the solution is pink-red.

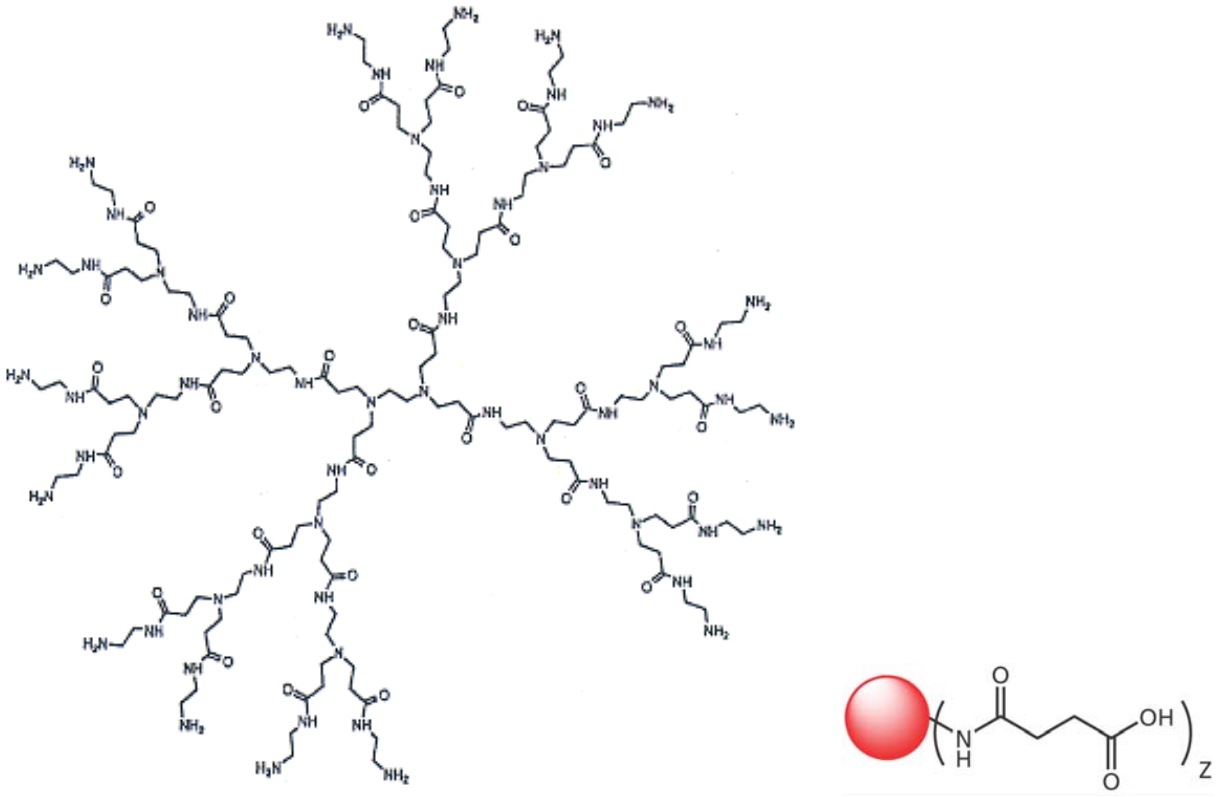

Figure 5.2. Chemical structure of (a) 2nd generation PAMAM dendrimer with (b) succinamic acid surface functional groups

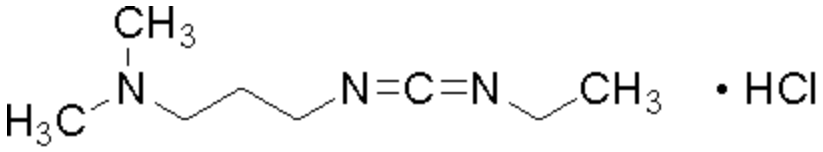

Figure 5.3. Chemical structure of 1-ethyl-3-(3-dimethylaminopropyl)carbodiimide hydrochloride

Table 5.1. Physical properties of poly(amidoamine) (PAMAM) dendrimers; molecular weights do not account for succinamic acid surface group: $C_4H_5O_3$, MW ~ 100

Generation	Surface Groups	Molecular Formula	Molecular Weight	Approximate Diameter (nm)
2	16	$C_{144}H_{292}N_{58}O_{28}$	3284	2.6
5	128	$C_{1264}H_{2528}N_{506}O_{252}$	28854	5.7
6	256	$C_{2544}H_{5092}N_{1018}O_{508}$	58076	7.2

5.2.3 MALDI Characterization of Fluorophore-G2 PAMAM Dendrimer Conjugate

Mass spectroscopy was conducted with an Applied Biosystems 4700 Proteomics Analyzer equipped with a 200Hz laser. The machine is a tandem time-of-flight mass spectrometer that generates ions via matrix-assisted laser desorption-ionization. Negative ion data collection utilized both reflecting detector and linear analysis. The former is used for high resolution, accurate mass measurement of lower molecular mass species (500-4000 Da) while the latter is used for large molecular mass species (3-15 kDa) with low resolution. Fluorophore-dendrimer conjugates were incorporated into alpha-cyano-4-hydroxycinnamic acid (CHCA) polymer matrices prepared at 10 mg/mL in 50:50 water:acetonitrile mixtures and containing 0.1% trifluoroacetic acid (TFA) (CHCA-TFA). As a means of comparison, the same fluorophore-dendrimer conjugates were prepared in CHCA matrices with the same solvents as before, except with 25 mM ammonium acetate in the solution in addition to TFA (CHCA-acetate) to ensure better ionization.[44]

5.2.4 Incorporation of Negatively-Charged Molecules into PEG-Like Films

Electrophoretic immobilization of the negatively charged fluorophore-dendrimer conjugate was accomplished by applying a voltage drop between the positively-biased conducting gold surface and the solution which contains the negatively-charged species. A diagram of the experimental setup is shown in scheme 5.1. Electrical equipment used in the circuit design included: a Hewlett-Packard E3620A DC power supply, two multimeters (Hewlett-Packard E2373A/E2378A) and a two-point probe setup. The multimeter monitoring current was in series with the electrochemical cell while the multimeter measuring voltage was in parallel. Within the electrochemical cell, one probe contacts the gold surface through the opening created during the deposition while the other probe contacts the electrolyte (~20 μL drop = 0.2 cm^2 film contact area) atop the

PEG film. After establishing both contacts, applied voltage on the DC power supply was set to 0.7 V for a period of 10 minutes (approximate time scale of complete film swelling). After the allotted time, the sample was rinsed with deionized (DI) water and dried with nitrogen. In order to investigate the effect of electric field as a driving force and the role it plays in the incorporation of the fluorophore-dendrimer conjugate into the films, diffusion was also studied for each of the generation 2, 5, and 6 dendrimer-based systems. Molecules were allowed to diffuse into the coatings for 10 minutes before undergoing the same DI water rinse/nitrogen drying post-incorporation treatment. Detection of fluorophore-dendrimer conjugate was determined using fluorescence microscopy.

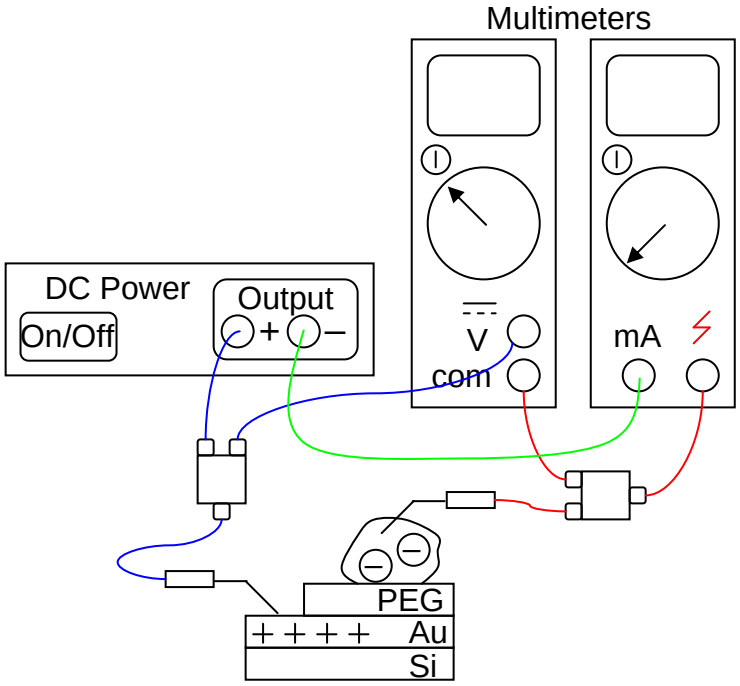

Scheme 5.1. Schematic of electrophoretic immobilization equipment for the incorporation of negatively-charged fluorophore-tagged PAMAM dendrimer molecules

5.2.5 Fluorescence Microscopy of Fluorophore-Dendrimer Conjugates

Fluorescence studies of the drifted and diffusion incorporated fluorophore-dendrimer conjugates were conducted using an air table-mounted Leica Microsystems

DM IRB inverted research microscope with an attached analog 640×480 pixel CCD camera (Model 4920, COHU Inc.), which was connected to a computer. Image transfer to the computer was with a precision frame grabber (PXC-200, Cyber Optics) and use of OpenBox image acquisition software. A high-speed shutter (Uniblitz® VMM-D1, Vincent Associates Inc.) controlled illumination of the microscope fluorescent light. Resolution with the 100× objective was 0.099 μm per pixel. Image analysis was conducted with the IDL software package (Research Systems Inc.) for generating pixel counts versus light intensity histograms, which were plotted and model fitted using OriginPro8 software (OriginLab Corp.). Matlab was used to plot contour maps of the fluorescent images.

5.2.6 Positron Annihilation Lifetime Spectroscopy of the PEG-Like Films

Two types of plasma-polymerized PEG-like coatings were prepared as previously-detailed in Chapter 3, at conditions of (1) 32 W, 1400 mTorr, 95°C and (2) 55 W, 1000 mTorr, 110°C. All films were 200-300 nm in thickness. PALS studies were conducted by Dr. David Gidley at the University of Michigan in an attempt to characterize pore size distributions of swelled-state PEG-like films. Based on swelling studies from Chapter 4, films from both deposition conditions were stored in DI water for ~15 minutes to allow complete expansion. After the allotted time, each sample was removed from the DI water holding cell and with water still covering the film surface (with the in tact swollen film), freezing was induced by either inserting the sample into a reservoir of liquid nitrogen or placing the sample into a freezer at -20°C. Once frozen, the water was sublimed from the preserved swollen structure using a FreeZone 6 liter benchtop lypophilizer from Labconco Corp.

5.3 Results and Discussion

5.3.1 Effectiveness of the Fluorophore-G2 PAMAM Dendrimer Binding Reaction

In order to characterize the pore sizes of swelled-state plasma-polymerized PEG-like films, fluorophore molecules with cadaverine binding sites were reacted in solution phase with poly(amidoamine) (PAMAM) dendrimers having carboxylic acid surface functional groups. The resulting conjugate was analyzed using negative ion scan matrix-assisted laser desorption-ionization (MALDI) mass spectroscopy to determine if conjugation had occurred.

5.3.1.1 MALDI Mass Spectroscopy of Fluorophore and G2 PAMAM Dendrimer

MALDI measurements of fluorophore and G2 dendrimer samples are shown in figures 5.4-5.9; these data serve as control samples for comparison to the MALDI spectra of the fluorophore-dendrimer conjugate. Figures 5.4 and 5.5 both show strong mass-to-charge ratio peaks of approximately 600-640 which correspond to the molecular weight of the fluorescent dye (MW = 640 g/mol). The peak at 617 m/z indicates the presence of fluorophore without conjugation to its sodium salt while the peak at 639 m/z is most likely caused by the elimination of a proton. The CHCA polymer matrix assists in the absorption of energy from the incident laser, thus helping to preserve the molecular structure of the fluorophore.[44] Comparison of figures 5.4 and 5.5 shows that the addition of ammonium acetate, a salt of a weak acid and weak base used to promote ionization of large molecular weight species, does not significantly affect the ionized species detected (e.g. ~617 and 639 m/z). This can be explained by the negative charge already present on the fluorophore prior to laser excitation (see figure 5.1). Figure 5.5 also indicates that there can be coordination between multiple fluorophore and sodium ion species. These are observed at 662 m/z (639 + Na^+), 1301 m/z (662 + 639), 1324 m/z (1301 + Na^+),

1963 m/z (1324 + 639) and ~2580 m/z (1963 + fluorophore). Peak intensity decreases with additional aggregate mass units relative to those of the parent peaks at 617 and 639 m/z. The aggregation noted is a function of charge effects of the dye and dilute concentration of fluorophore molecule (1-2 mg/mL).[45]

The strong mass-to-charge ratio peaks at 4844 and 4856 m/z shown in figures 5.7 and 5.9, respectively, are representative of the G2 PAMAM dendrimer, which has a molecular weight of 4856 g/mol when accounting for the succinamic acid surface groups. The loss of 12 mass units from the true molecular weight of the dendrimer in figure 5.7 is probably due to loss of protons, since it unlikely a single carbon atom would be eliminated without any hydrogen attachment. Similar to the fluorophore spectra, figure 5.7 shows evidence of minor aggregation reflected by the peak at 9694 m/z. More importantly, figure 5.6 indicates fragmentation of the dendrimer at mass-to-charge ratios of: 2428 m/z (one-half of the dendrimer molecular weight), 1227 m/z (one-fourth MW), and 604 m/z (one-eighth MW). Fragments shown in figure 5.6 are possible causes for the peaks seen in the low molecular weight spectrum of the G2 dendrimer and account for succinamic acid surface groups. Fragmentation occurs because relative to the fluorophore, the dendrimer is a much larger molecule and is therefore more susceptible to internal bond breaking upon exposure to the energy imparted by the laser. Although minor aggregation is seen between in-tact dendrimer molecules in figure 5.7, there is no detectable evidence of aggregation between the parent dendrimer molecule and the smaller fragments.

Because carboxylic acid is a weak acid and partially dissociates to yield a proton, surface groups of the dendrimer will have a partial negative charge. As a result, addition of ammonium acetate does not significantly alter the ionizing ability of the dendrimer (figure 5.6 vs. figure 5.8; figure 5.7 vs. figure 5.9). Such results offer further evidence

that a natural saturated negative charge on the PAMAM dendrimer exists as a result of the presence of succinamic acid functional groups.

5.3.1.2 MALDI Mass Spectroscopy of Fluorophore-G2 PAMAM Dendrimer Conjugate

Figures 5.10 and 5.11 show low and high molecular weight MALDI spectra, respectively, for the fluorophore-dendrimer conjugate after reaction. From figure 5.10, a large peak is observed at 617 m/z, indicating the presence of either unreacted fluorophore remaining after purification, a fragment of dendrimer generated during irradiation, or both. A peak at 617 m/z is observed in figure 5.4 for the fluorescent dye while peaks at 604 and 620 m/z are seen in figure 5.6 for the dendrimer solution. The high molecular weight scan in figure 5.11 shows an intense peak at 4856 m/z, which according to figure 5.7 or 5.9 represents the dendrimer without fluorophore attachment. However, an additional peak is observed at 5458 m/z, which is a shift of +602 m/z units from the pure dendrimer peak. This peak *suggests* the attachment of a single fluorophore molecule to one of the sixteen surface groups on the G2 PAMAM dendrimer. As seen from figure 5.7, it is also likely that the addition of 602 m/z units to the dendrimer in figure 5.11 is a result of an association between the dye and the dendrimer and not between a dendrimer fragment with the dendrimer. This interpretation is reasonable because there is no detectable peak indicating aggregation between the parent dendrimer molecule and the smaller dendrimer fragments (figure 5.7). A closer look reveals that, while chemical bond formation between the primary amine of the cadaverine group in the fluorophore with the carboxylic acid dendrimer surface group is possible, the difference of 15 mass units between the whole fluorophore molecule (617 m/z) and the detected addition of 602 m/z units indicates possible scission of the primary amine in the fluorophore molecule. Scission from the Alexa Fluor® portion of the fluorophore would result in a decreased or total absence of fluorescence. From these results, it is likely that no bond exists between

the fluorophore and dendrimer molecules, but rather, the two are coordinated in a one-to-one ratio (figure 5.11).

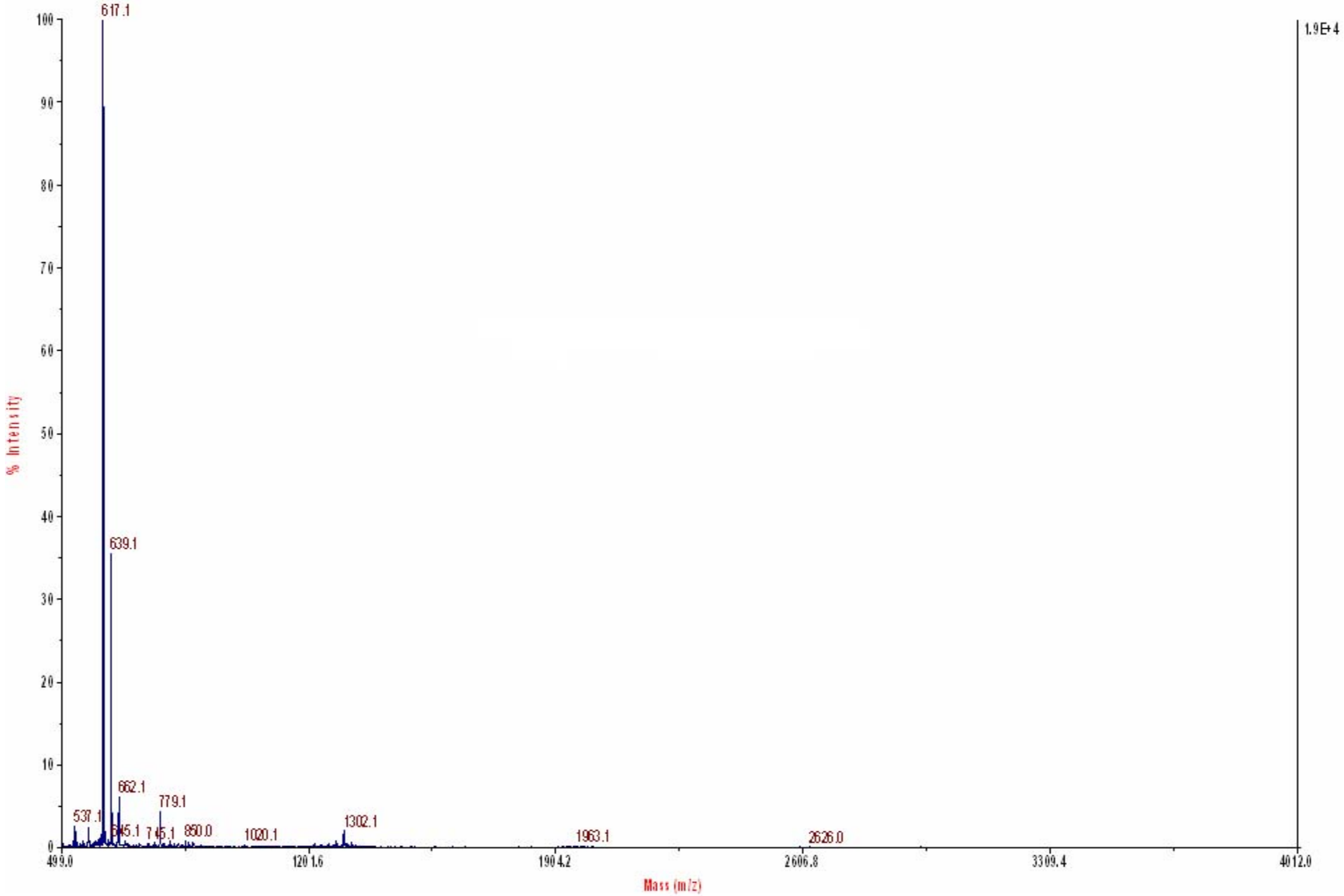

Figure 5.4. MALDI spectrum of fluorophore dye using CHCA polymer matrices in 50:50 water:acetonitrile mixtures with 0.1% TFA

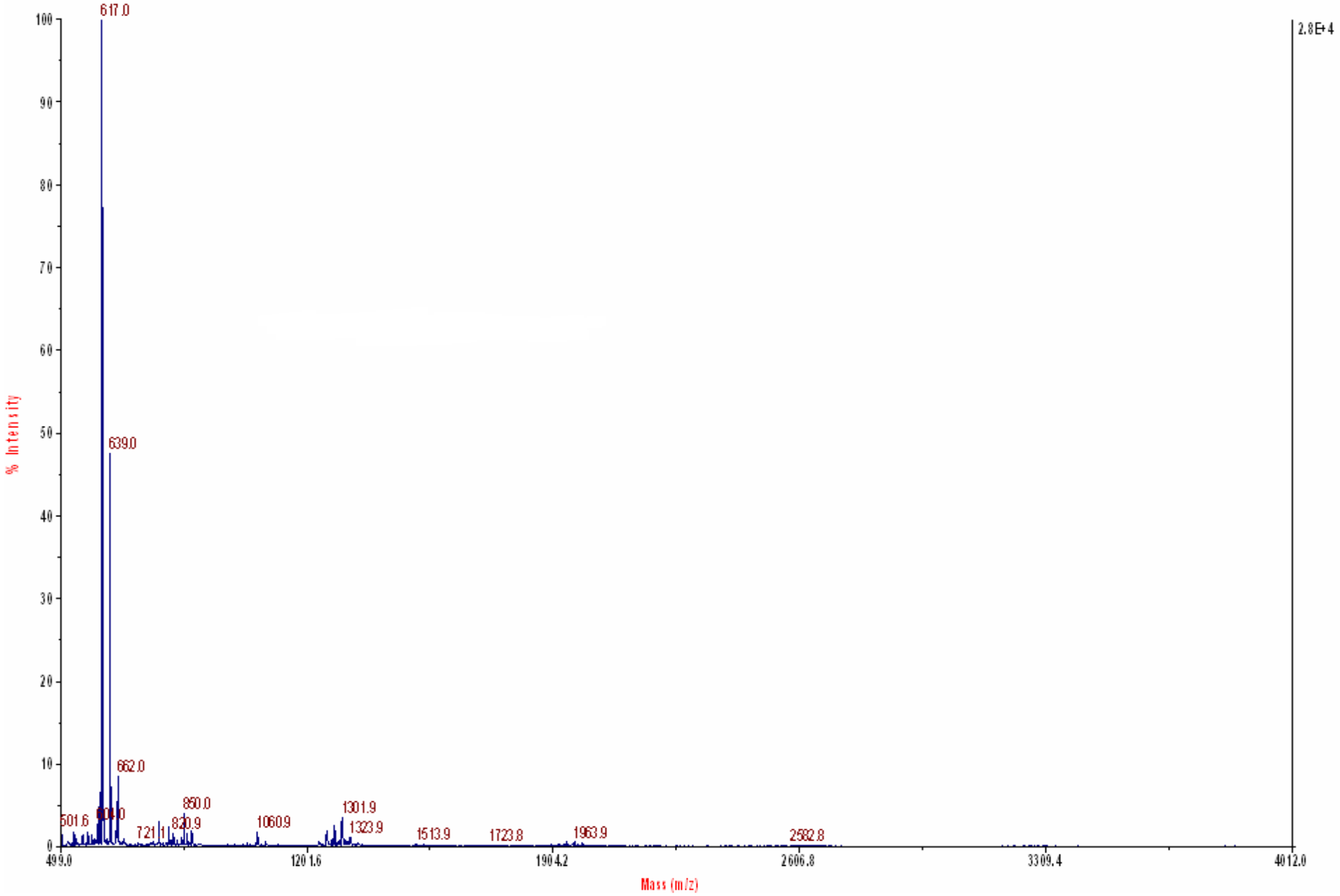

Figure 5.5. MALDI spectrum of fluorophore dye using CHCA polymer matrices in 50:50 water:acetonitrile mixtures with 0.1% TFA and 25 mM ammonium acetate

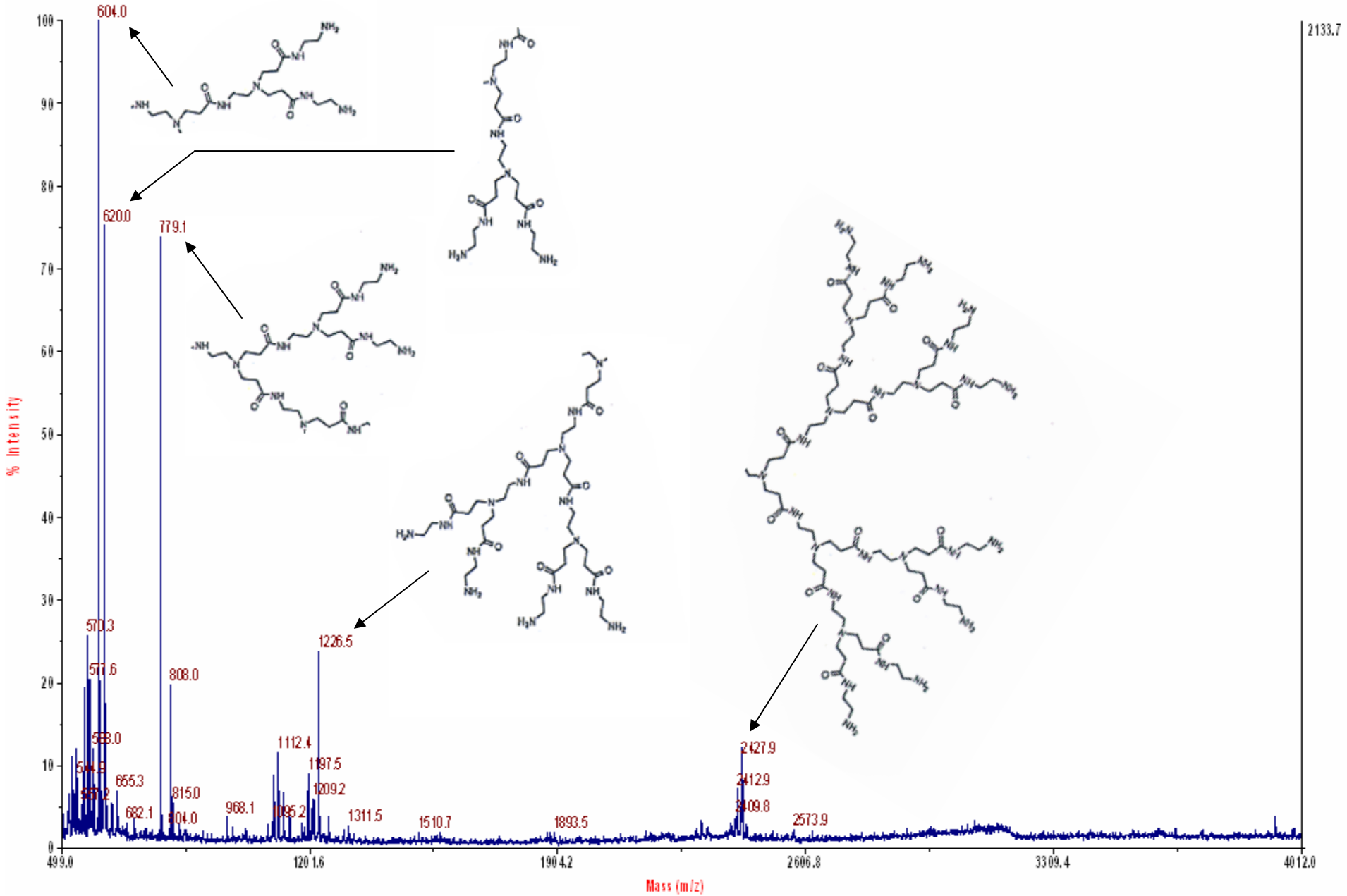

Figure 5.6. Low molecular weight MALDI spectrum of G2 PAMAM dendrimer using CHCA polymer matrices in 50:50 water:acetonitrile mixtures with 0.1% TFA

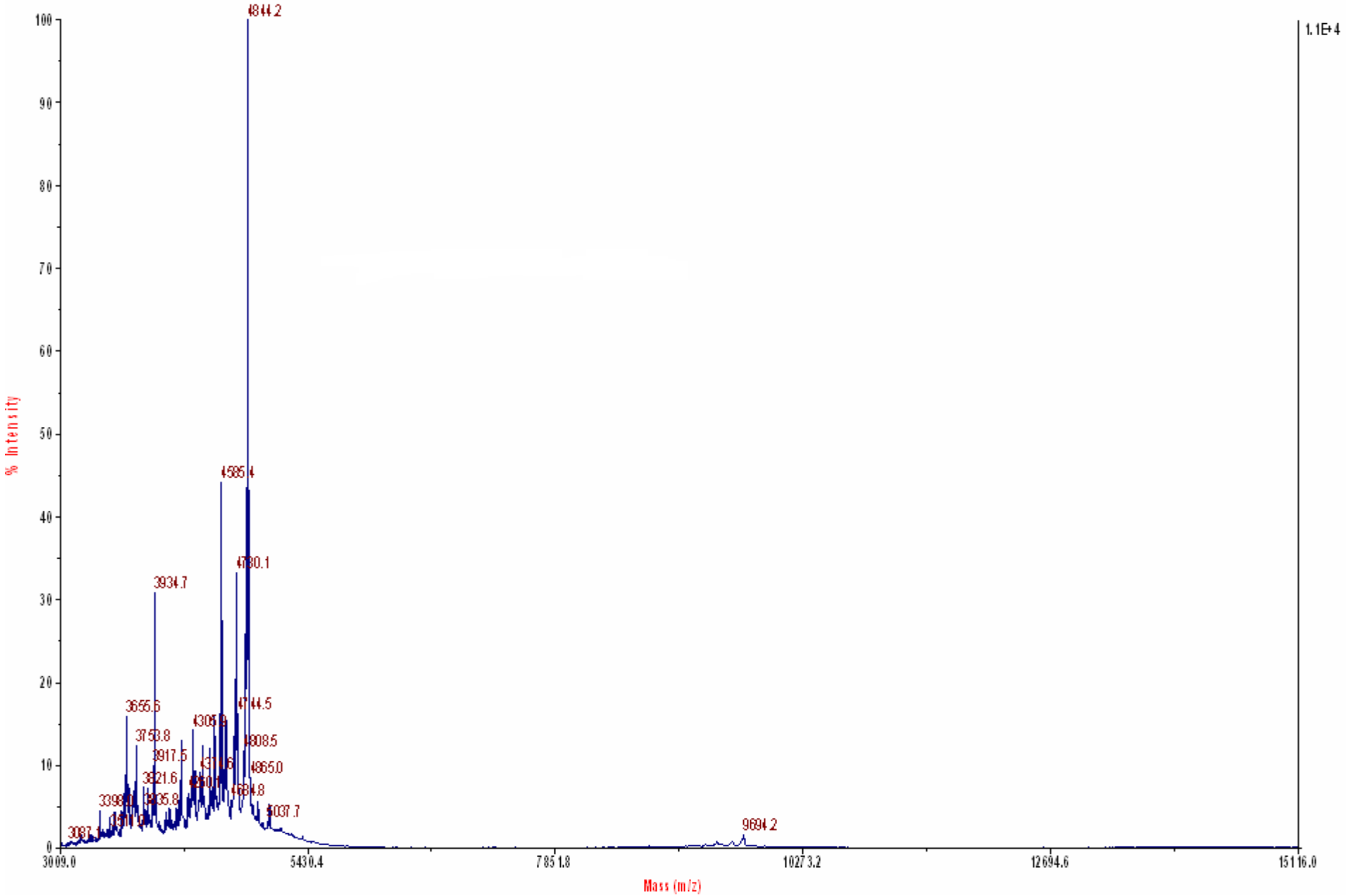

Figure 5.7. High molecular weight MALDI spectrum of G2 PAMAM dendrimer using CHCA polymer matrices in 50:50 water:acetonitrile mixtures with 0.1% TFA

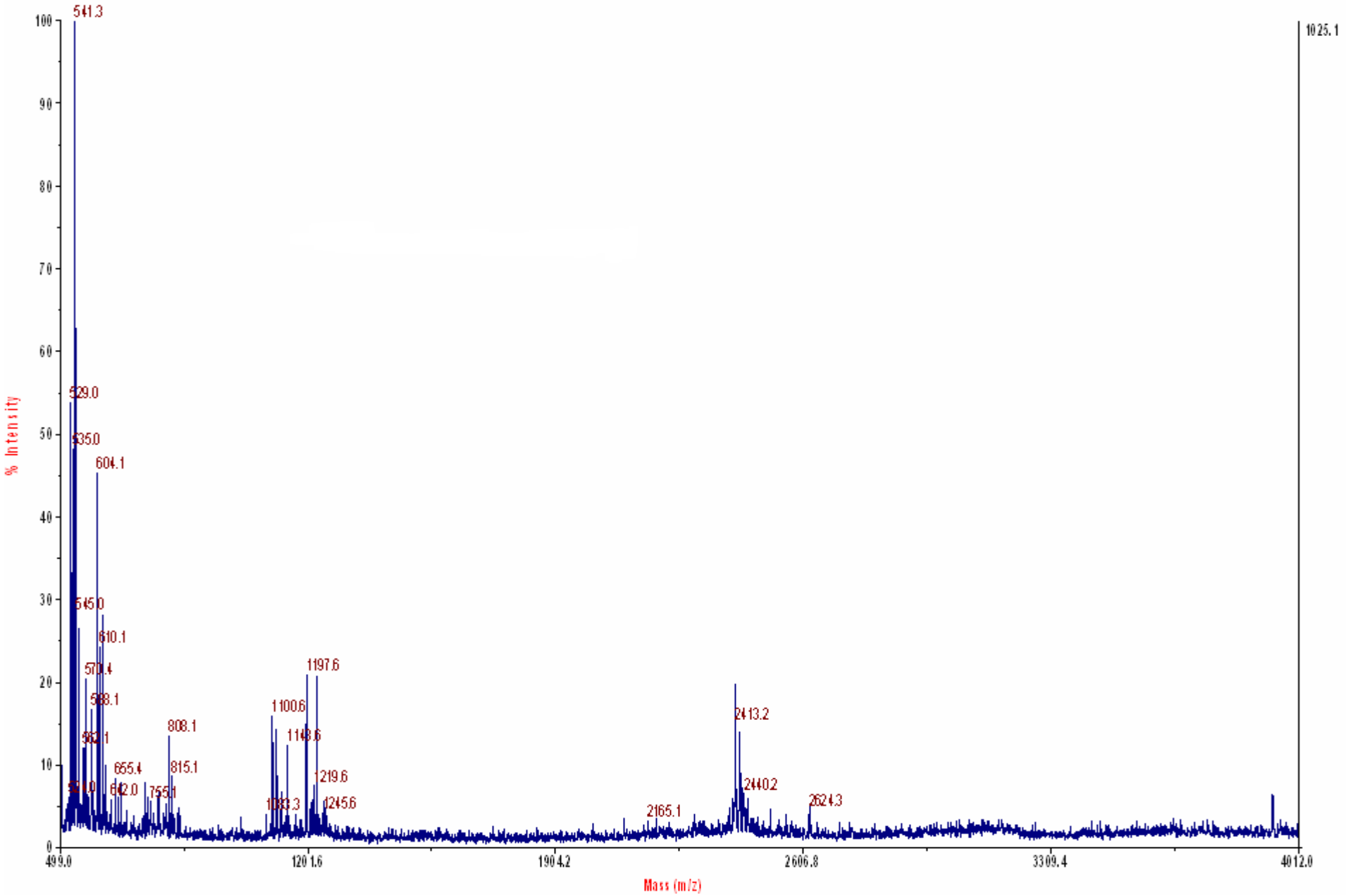

Figure 5.8. Low molecular weight MALDI spectrum of G2 PAMAM dendrimer using CHCA polymer matrices in 50:50 water:acetonitrile mixtures with 0.1% TFA and 25 mM ammonium acetate

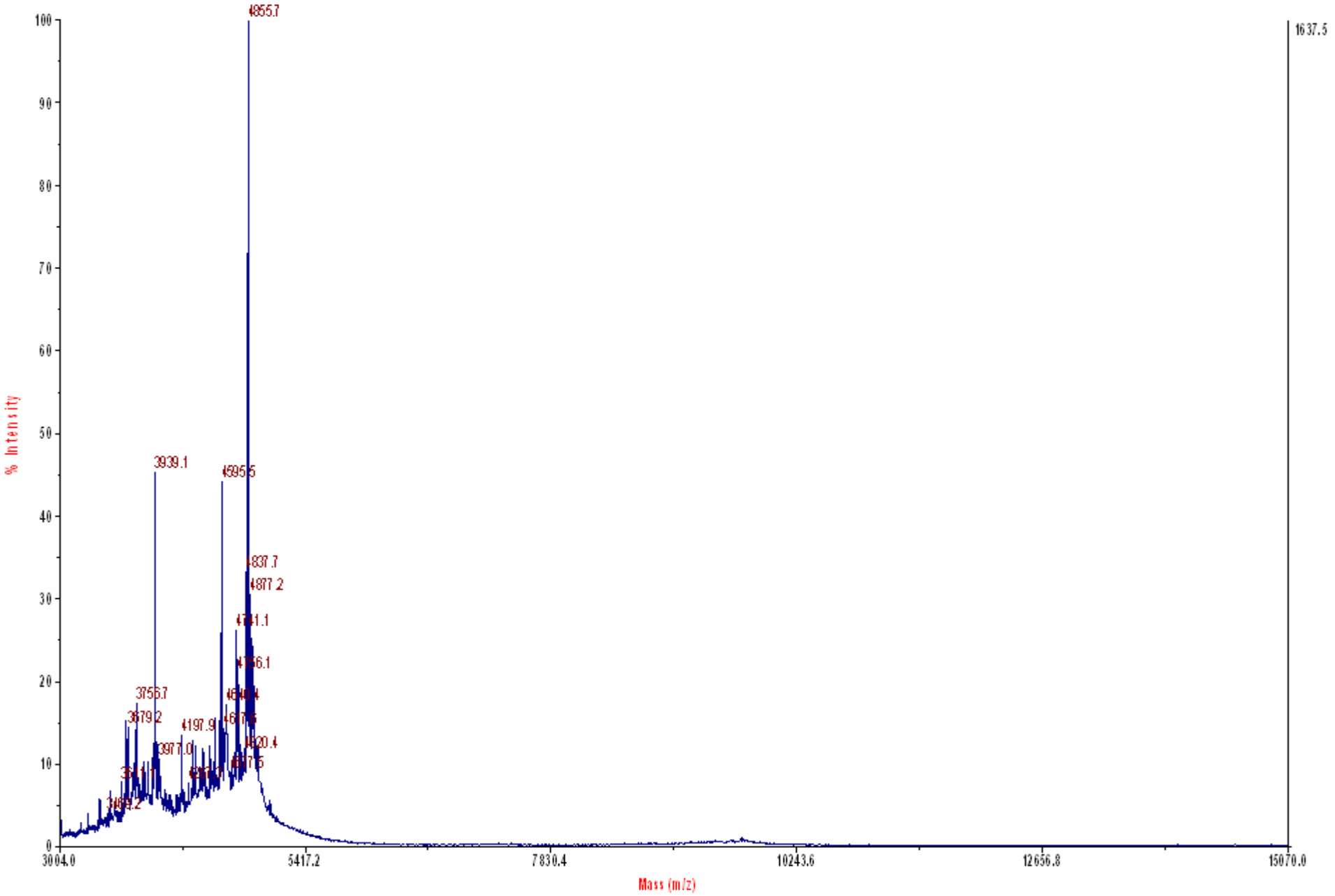

Figure 5.9. High molecular weight MALDI spectrum of G2 PAMAM dendrimer using CHCA polymer matrices in 50:50 water:acetonitrile mixtures with 0.1% TFA and 25 mM ammonium acetate

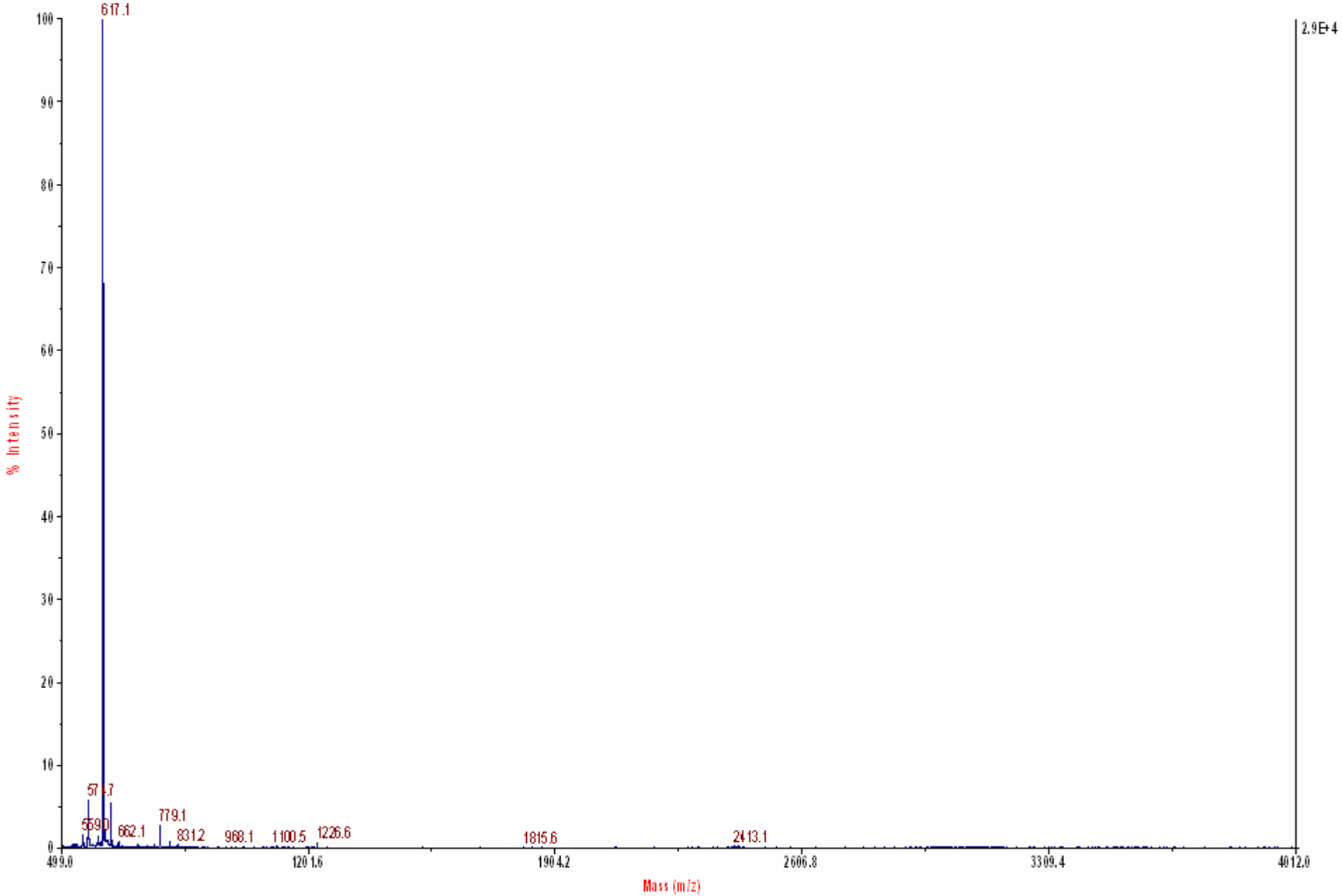

Figure 5.10. Low molecular weight MALDI spectrum of fluorophore dye-G2 PAMAM dendrimer conjugate using CHCA polymer matrices in 50:50 water:acetonitrile mixtures with 0.1% TFA

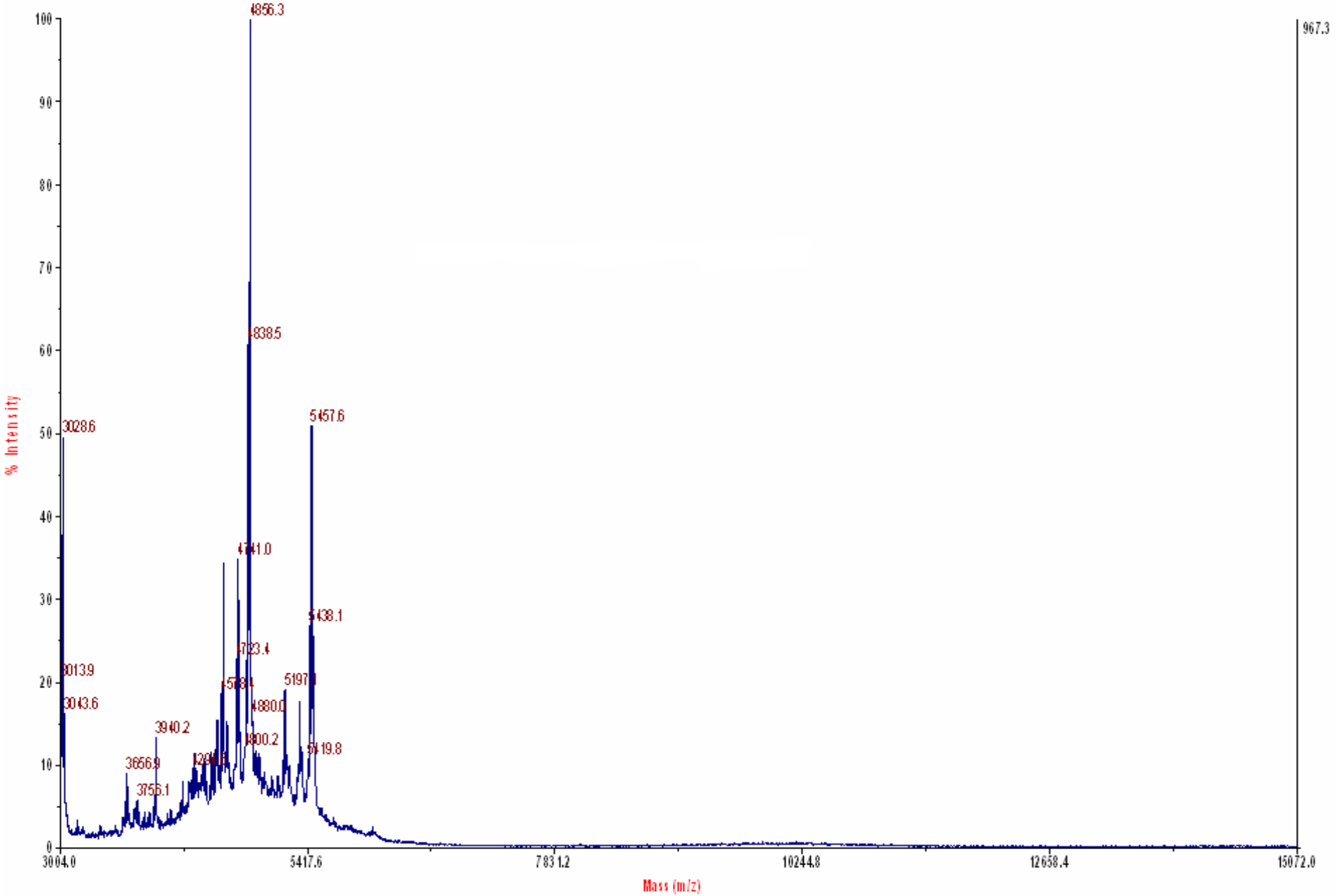

Figure 5.11. High molecular weight MALDI spectrum of fluorophore dye-G2 PAMAM dendrimer conjugate using CHCA polymer matrices in 50:50 water:acetonitrile mixtures with 0.1% TFA

5.3.2 Fluorescence Microscopy of Immobilized Fluorophore-Dendrimer Conjugate

After confirming coordination of the fluorophore to the dendrimer using MALDI, film pore sizes were determined by the degree of incorporation of the conjugate into the coating by fluorescence microscopy. Each dendrimer, with a diameter ranging from approximately 2.5 (G2) to 7.5 (G6) nm, was tested with two film entry mechanisms: diffusion and drift using the electrophoretic immobilization technique. While diffusion relies upon movement of molecules based on concentration gradients between the dendrimer solution and the water-saturated hydrogel, electrophoretic immobilization uses an electric field as a driving force to "force" charged molecules through mesh openings of the polymer film. Due to the large variety of reactive species created in the vapor phase plasma environment, subsequent ion bombardment initiates surface reactions that lead to film growth with no recognizable repeat unit and a distribution of pore sizes.[46] The dendrimer incorporation approach used in this study to probe pore sizes allows an indirect determination of the largest available void openings of swelled-state plasma-polymerized polyethylene glycol-like films by systematic size variation of transport species.

Fluorescence microscopy was used to detect the presence of fluorophore-labeled dendrimers inside the polymeric plasma-deposited coatings. Images consist of an equivalent number of pixels, with each pixel assigned a value between 0 and 255 intensity units. Higher intensity values indicated higher fluorescent species concentrations. Equivalent pixel counts allowed an accurate cross-comparison between images of different samples with the same microscope magnification. Statistical analysis involved summing the number of pixels that were assigned a particular intensity value. Representative histograms are shown in figure 5.12. From a Gaussian model fit, mathematical parameters such as integrated area under the curve, peak positioning and full-width at half-maximum (FWHM) were back-calculated to allow physical

interpretation of the raw data; results are shown in table 5.2. Calculated integration values affirm that the number of counts, or pixels in an image, remain the same (column 5). Spread of the Gaussian-distributed counts (column 6) and peak maxima (column 4) also remain fairly constant.

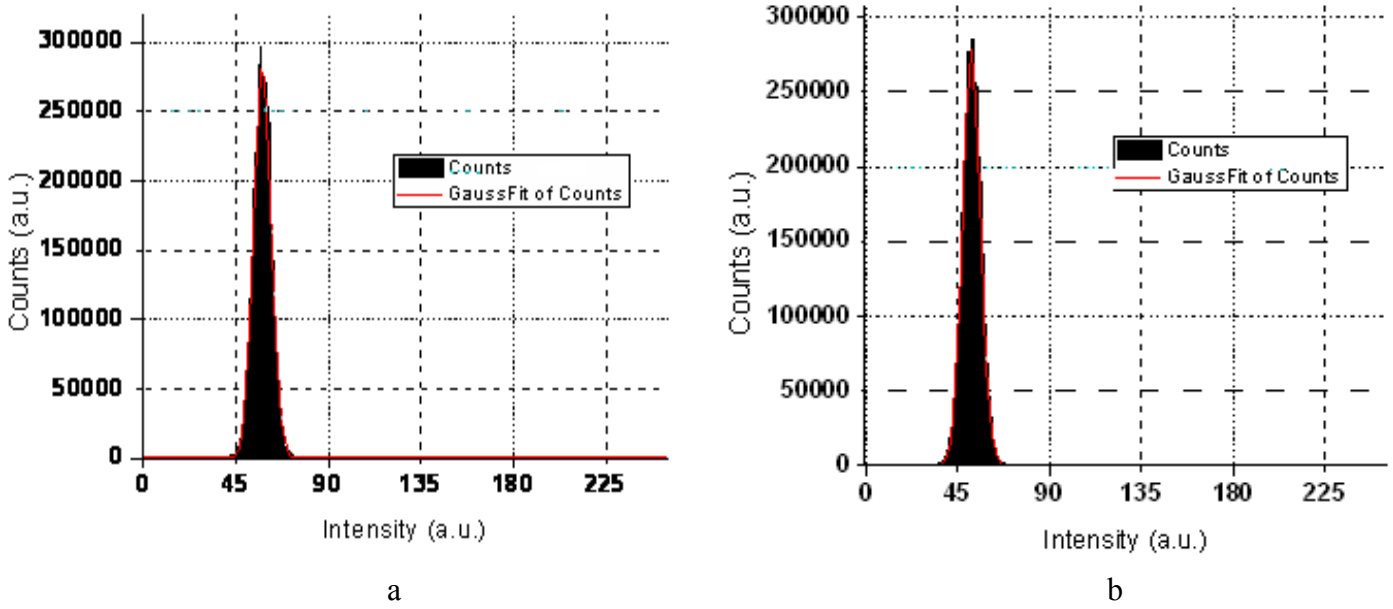

Figure 5.12. Histogram of counts versus intensity for (a) drifted G2 PAMAM dendrimer and (b) blanket hydrogel coating with no exposure to fluorophores. The peak positioning for the histogram of the smallest, most mobile G2 dendrimers in (a) centers at ~58 intensity units while the blank control sample of (b) gives a background baseline of ~52 intensity units.

Table 5.2. Gaussian Model Fit Parameters for Count Versus Intensity Histograms of Fluorophore-Labeled PAMAM Dendrimers

Generation	Mechanism of Entry	Peak Positioning (Intensity Units)	Peak Positioning (Count Units × 10^5)	Total No. Counts (× 10^6)	FWHM
2	Drifted	57.8	2.92	3.07	9.89
2	Diffusion	57.3	2.77	3.07	10.4
5	Drifted	54.4	2.83	3.07	10.2
5	Diffusion	53.0	2.91	3.08	9.95
6	Drifted	52.3	2.91	3.10	10.0
6	Diffusion	52.7	2.31	3.13	12.7
Blank	–	51.8	2.78	3.09	10.4

Because of variation in pore sizes of plasma-polymerized films, molecules entering the matrix will appear in higher concentrations at regions where transport through the hydrogel is less constricted. As a result, microscopy results show bright pockets of fluorescence captured in isolated regions of the imaging area. Figure 5.13 reveals the fluorescence difference between drifted G2 dendrimers and a blank hydrogel film with no fluorescence exposure. While the majority of the sampled area *appears* to resemble the background intensity of a blank sample, intensity peak positioning statistics (table 5.2, column 3) and visual evidence in figure 5.13 indicate a relatively uniform distribution of fluorophore-labeled dendrimer. Gaussian model curve fits show that the peak position for the histogram of the smallest, most mobile G2 dendrimer is centered at ~58 intensity units while the blank control sample gives a background baseline of ~52 intensity units. Subtle shifts in peak intensity position occur because all pixels in an image (i.e. total number of counts) are counted, not only those responsible for the bright fluorescent spots, which are at the high end of the intensity spectrum. The shift of +6 intensity units implies that the concentration of the fluorophore-dendrimer conjugate in the lower intensity areas are sufficiently low to prevent visual verification of their presence.

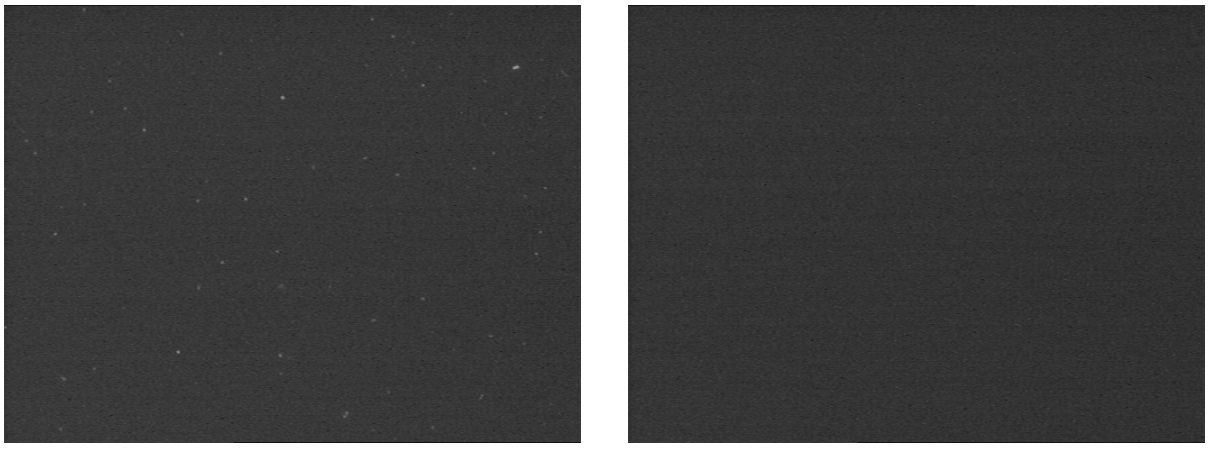

a b

Figure 5.13. Fluorescence images for (a) drifted G2 PAMAM dendrimer and (b) blanket hydrogel coating with no exposure to fluorophores. Bright fluorescent spots are observed

in regions where higher concentrations of fluorophore-labeled dendrimers enter the film, with respect to incorporation levels over the entire imaging area.

In order to confirm the uniqueness of mean values calculated from Gaussian fits of the histograms in figure 5.12 (and column 3 of table 5.2), statistical *t*-tests were conducted. *T*-values and degrees of freedom are shown in table 5.3. The *t*-distribution is a continuous, symmetric and bell-shaped curve that ranges from minus infinity to plus infinity. While the *t*-distribution is independent of sample mean and standard deviation,[47] its shape is determined by the degrees of freedom. Here, degree of freedom was approximately equal to the sum of the total number of counts in each sample as calculated from the model fit. Counts versus intensity data may be represented as a Gaussian distribution because for a large number of degrees of freedom, the *t*-distribution turns into the normal distribution.[47] *T*-values are calculated as the ratio between the difference in mean values of the two sample sets to the degree in variability, or dispersion, of the two sample sets. This is expressed by equation 5.1,[47]

$$\frac{\text{difference between sample means}}{\text{variability of samples}} = \frac{\bar{x}_1 - \bar{x}_2}{\sqrt{\frac{\text{var}_1}{n_1} + \frac{\text{var}_2}{n_2}}} = t - \text{value} \quad (5.1)$$

where, $\bar{x}$ is sample average, var is sample variance and *n* is the total number in the sample set. Given the degrees of freedom and calculated t-values, an alpha (risk) level was chosen and t-values were evaluated in a standard table of significance to determine whether the t-value is large enough to be significant. Based on the large degrees of freedom for each of the two sets of histograms compared in table 5.3, we can say that the means are statistically unique up to a 99 % level of confidence ($\alpha = 0.01$). For example, the difference in average intensity between the G2 *drifted* PAMAM dendrimer conjugate (table 5.2, column 3: 57.8) and the G2 *diffused* PAMAM dendrimer conjugate (57.3) is approximately 0.5 intensity units. This number is based on (1), the individual assignment of pixels in an image to a numerical value of between 0-255 and (2), the fact that each

image contains the same number of pixels. From table 5.3, row 2, a *t*-value of 279 was calculated using 6.14×10^6 degrees of freedom (sum of the total number of calculated pixels from model fits of histograms for the G2 drifted dendrimer and G2 diffused dendrimer). Using the limiting case when the degree of freedom approaches infinity with an alpha equal to 0.01, the calculated *t*-value is greater than the tabulated value (2.576) for a two-sided test. Therefore, even with a small difference in average intensities, the mean intensities of the G2 drifted and diffused dendrimer are unique.

Table 5.3. Statistics for the *t*-distribution test comparing the mean intensity values (table 5.2, column 3) from fluorescence images captured for PEG-like plasma films loaded with fluorophore-labeled dendrimers of varying sizes

Samples Tested Using the Student's *t*-distribution	***t*-value**	**Degrees of Freedom ($\times 10^6$)**
G2 PAMAM drifted and G2 PAMAM diffused	279	6.14
G6 PAMAM drifted and G6 PAMAM diffused	1162	6.23
G6 PAMAM drifted and blank	170	6.19
G6 PAMAM diffused and blank	952	6.22
G5 PAMAM drifted and G5 PAMAM diffused	376	6.15

The bright fluorescent spots observed in figure 5.13 may be explained by consideration of the high end of the intensity spectrum (figure 5.14) for the drifted G2 dendrimers (closed circles). Counts measured in the high end of the spectrum are proportionally small relative to the total number of pixels in an image and thus account for high intensity emissions that correspond to the small spots seen in figure 5.13(a). We can also compare the total amount of high intensity fluorescence with pore size openings in the plasma-deposited films as shown in figure 5.14 and table 5.4. From figure 5.14, it is evident that the specific transport mechanism has little effect on the incorporation of the G2 PAMAM dendrimer in the PEG-like films. This is reflected in the total fluorescence count in table 5.4 (column 2). The similarity in total counts indicates that pore size openings in the swelled state plasma films are sufficiently large (>>2.6 nm) to

allow easy transport into and out of the film. Fluorescence imaging indicates that the fluorescently-labeled dendrimers are trapped within the matrix; residual fluorophore-dendrimer molecules are washed from the surface with a DI water rinse and nitrogen dry which causes film de-swelling and molecular entrapment.

Total fluorescent count decreases by more than 50% in the loading of diffused G2 dendrimer versus the drifted G5 dendrimer. The decrease in counts (Δ = -10,785) was observed despite the fact that the G5 dendrimer, which has 128 surface groups compared to 16 for the G2 dendrimer, experienced an external electric field as the driving force. Because the largest absolute decrease takes place between the G2 and G5 dendrimer, we can narrow our search for the upper bound of pore size openings to between 2.6 and 5.7 nm in diameter. This indicates that there exists a limiting size beyond which molecules will not be able to penetrate into the bulk of the film. This is seen for the G6 dendrimer, which shows minimal fluorescence in either the drifted or diffused case. We therefore conclude that the majority of the void space openings in the plasma film are less than 7.2 nm because the significant charge from the negatively-biased succinamic functional group and fluorophore are unable to compensate for molecular size limitations. In other words, the applied electric field was insufficient to force the G6 dendrimer into the PEG film.

Also, another drastic decrease is detected between the drift and diffusion of the G5 dendrimer (Δ = -3,981). Given the equivalent species size, this implies that for the G5 dendrimer, transport mechanism is an important factor in fluorescent counts because an approximate 40% decrease in fluorescence is observed when no electric field is applied. An external force is required for molecule incorporation when the molecule diameter is approximately equal to the pore (opening) size. This, coupled with a further decrease in counts (Δ = -5,316) with increases in molecular size (G5 diffused $\rightarrow$ G6 drifted), indicates that ~5.5-6.0 nm is a reasonable estimate for the upper bound diameter of pore size of the PEG-like plasma films.

The counts listed in table 5.4 were normalized to gain additional insight into what fraction of total image area accounted for visible fluorescence (column 4). Normalization with respect to total imaging area accentuates the differences in molecular loading of different-sized species. For example, table 5.2 shows that the average intensity (with the background included) of the G2 drifted dendrimer is ~58 intensity units while the average intensity of the G6 diffused dendrimer is ~52 intensity units. When normalized, this signifies that there is ~375 times the amount of fluorescence counts from the G2 drifted dendrimer as there is from the G6 diffused dendrimer (table 5.4, column 3).

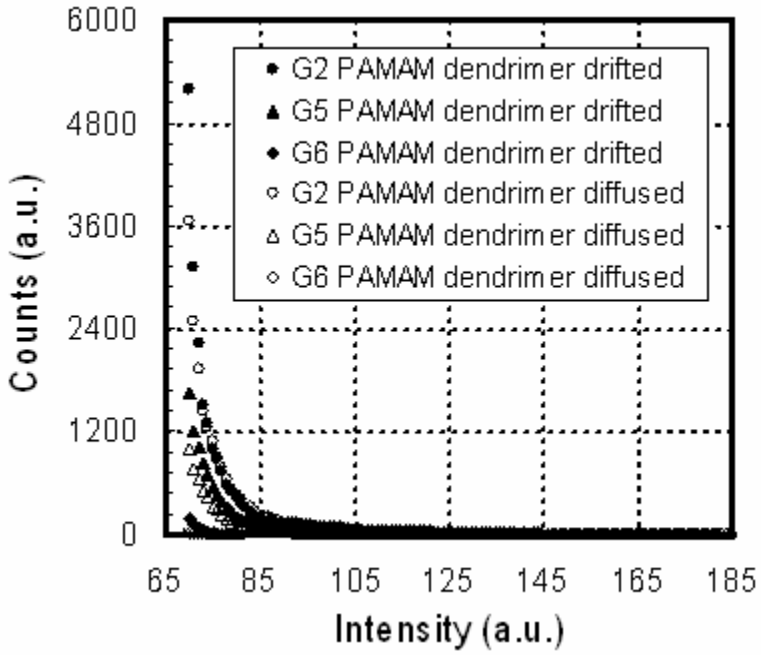

Figure 5.14. High intensity-end of counts versus intensity histogram for drifted (closed symbols) and diffused (open symbols) PAMAM dendrimers. Counts detected in upper intensity regions (>70) are responsible for the bright fluorescent spots where higher concentrations of fluorophore-labeled dendrimers are able to enter the film (see figure 5.13(a)).

Table 5.4. Total fluorescence and normalization of counts for intensities greater than 70

Sample	Count Total for Intensities ≥ 70 (Integrated Area)	Normalized Counts with Respect to:	
		G6 PAMAM Diffused Sample	Total No. of Counts
G2 PAMAM drifted	22109	375.	7.20×10^{-2}
G2 PAMAM diffused	20551	348.	6.69×10^{-2}
G5 PAMAM drifted	9766	165.	3.18×10^{-2}
G5 PAMAM diffused	5785	98.1	1.88×10^{-2}
G6 PAMAM drifted	469	7.95	1.53×10^{-3}
G6 PAMAM diffused	59	1.00	1.90×10^{-4}

Contour maps were created using Matlab to spatially resolve the location of the fluorescent spots seen in figure 5.13 for the drifted G2 dendrimer, a blank sample without exposure to fluorophores, and two control fluorophore samples of the unbound Alexa Fluor® 488 cadaverine dye and fluorescein. These results also assist in the determination of the region of sample area responsible for emission as shown in figure 5.15. The plots depict a 100 square pixel area on the surface that is an average representation of the sample. In comparing the contour maps between the G2 drifted dendrimer (figure 5.15(a)) and the blank (figure 5.15(b)), it is evident that although the background intensity of both samples *appears* to be the same visually (figure 5.13), there is an 8-12 intensity unit difference between the two that contributes to the higher average pixel intensity of the drifted G2 dendrimer (58 vs. 52 intensity units for the blank from figure 5.12). Quantitatively, the bright pockets of fluorescence for the drifted G2 dendrimer can have intensity values almost double that of the background (~110 for the fluorescent spot vs. 60 for the background). From the calibrated 0.099 μm/pixel ratio for the 100× objective we calculate that the fluorescence emission originates from an area much larger than the pore diameter calculated from the electrophoretic drift studies (5.5-6.0 nm). Figure 5.15(a) indicates that the bright fluorescent spot is confined to a box of 100 × 400 nm dimensions, or approximately 4% of the total imaged sample area. Given that fluorescence microscopy images average over the entire depth of the film, we can assume

that the emission is from fluorophore molecules occupying ~4% of the volume exposed to the dye (product between film contact area of fluorophore-dendrimer conjugate solution, 0.2 cm^2, and thickness of film, ~700 nm). With a total exposed volume of ~1.4 $\times 10^{-5}$ cm^3 and a volume of ~9.2 nm^3 for an individual G2 PAMAM dendrimer, we estimate the maximum allowable number of fluorophore-G2 PAMAM dendrimer conjugates to be ~6.1 $\times 10^{13}$, or 1.0 $\times 10^{-10}$ moles for a total of ~0.55 μg of material (using the 5458 m/z peak of the conjugate from figure 5.11 as the molecular weight). This calculated value equals the total amount of material in a 700 nm thick film using 20 μL of fluorophore-G2 PAMAM dendrimer conjugate solution transported by electrophoretic drift. Therefore, for a drug molecule of roughly the same diameter as our test complex, this equates to a loading of ~2.76 $\times 10^{-2}$ $\mu g/mm^2$. We note that this model does not establish the fluorescence emission intensity generated by a known concentration of fluorophore nor does it account for background emission. Rather, we use a cutoff point of 70 intensity units as a binary indicator of whether a pixel is part of the cluster of pixels accounting for the fluorescent spot observed in an image. From the contour maps (figure 5.15(a) and (c)), each spot appears to be localized such that there is a confined region where pixel intensities are greater than the 70 units. Thus, while a discernable shoulder at 70 intensity units in figure 5.12(a) cannot be identified, this value appears to be a reasonable estimation for our cutoff that describes the bright fluorescent spots (figure 5.13(a)).

The 100 × 400 nm region from where the fluorescence originates correlates well with size dimensions of the particles imbedded within the bulk of the film during the deposition process (figure 4.3(a)). Aside from controlling swelling and dissolution properties, particles may also create "defect" regions within the bulk of the film that allow molecular channeling, and thus facilitate incorporation of the fluorophore-dendrimer conjugate. While there is some level of fluorescence intensity observed throughout the sampled space as evidenced by a greater background intensity (figures

5.15(a) and (b)), the bulk of the film has an average pore size much smaller than that estimated by the electrophoretic drift technique.

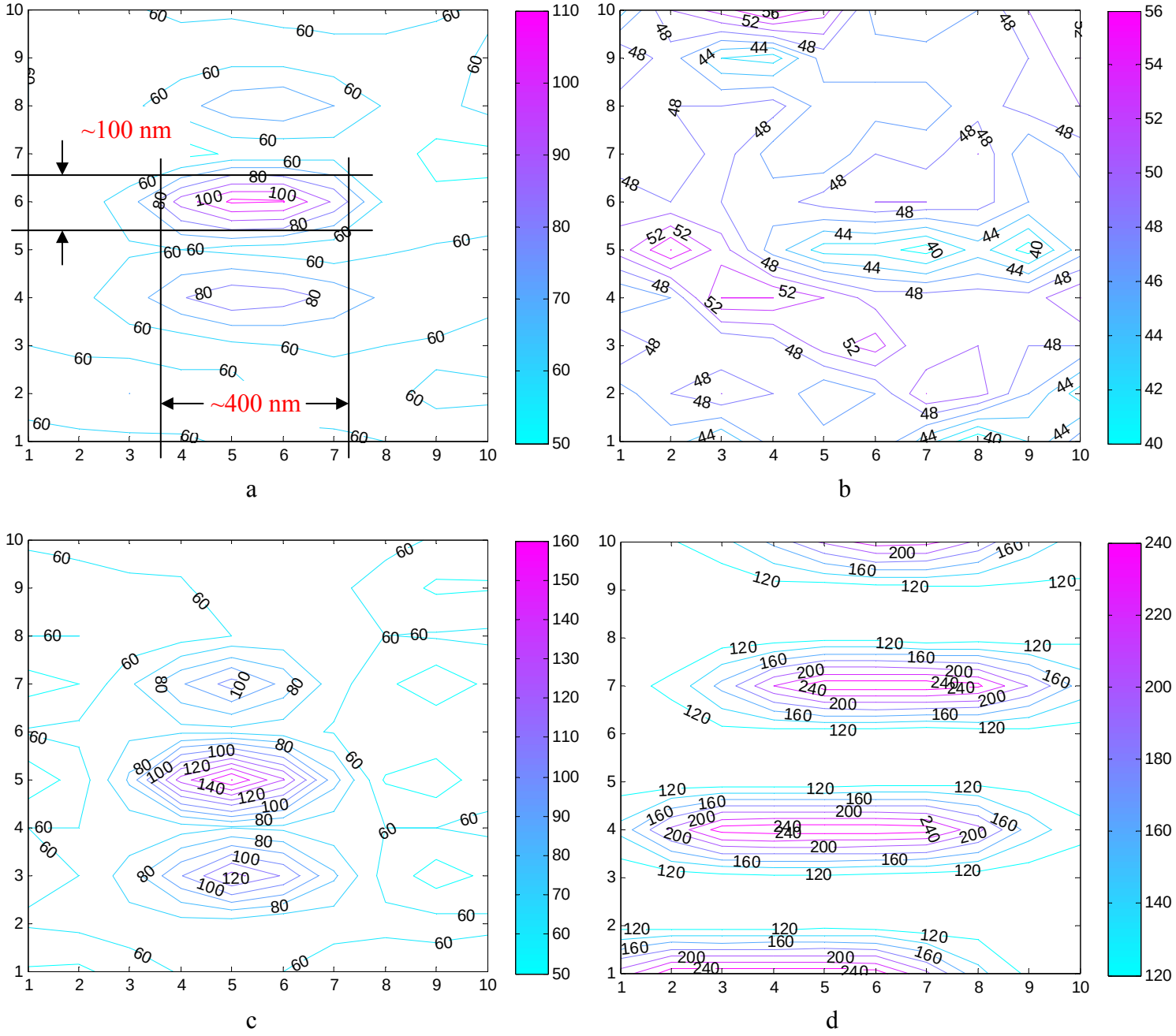

Figure 5.15. Fluorescence intensity contour plots for (a) drifted G2 PAMAM dendrimer, (b) blanket hydrogel coating with no exposure to fluorophores, (c) Alexa Fluor® 488 cadaverine fluorophore and (d) fluorescein fluorophore.

In collaboration with Dr. David Gidley at the University of Michigan, positron annihilation lifetime spectroscopy was used to determine the *average* pore size of swelled-state plasma-polymerized PEG-like coatings as a function of depth. The bulk of the film was probed by injection of positrons of varying energies. Table 5.5 summarizes the raw data of the PALS studies. Samples 3 and 4, which correspond to film deposition at higher input energy, longer mean free paths of vapor species and a greater substrate temperature, have smaller positronium micropore lifetimes and consequently, a smaller nanopore diameter in comparison to samples 1 and 2, which are deposited at lower powers, higher frequency of inelastic collisions and lower substrate temperatures.

The effect of water freezing rate on the pore size of films deposited under the same conditions (e.g. sample 1 versus 2; sample 3 versus 4) was also investigated. This test was conducted because for films experiencing a sudden rapid expansion of water from within the polymer matrix, as is the case when films are exposed to liquid nitrogen (samples 2 and 4), we expected damage to internal film crosslinks, thus creating larger void volumes and inaccurate PALS measurements of pore size. However, measurements indicated that there is little difference between liquid-nitrogen-exposed samples and samples frozen gradually at -20°C. For example, samples 1 and 2 have similar pore diameters regardless of pre-treatment and samples 3 and 4 also follow the same trend, albeit with smaller sizes. Therefore, we can average the diameters for samples 1 and 2 and compare them to the average diameters for samples 3 and 4. The average lifetimes correspond to spherical pore diameters of 0.648 ± 0.002 nm for the looser crosslinked samples 1 and 2 versus 0.589 ± 0.003 nm for the higher crosslinked samples 3 and 4. From these measurements, we conclude that there is an ~10% difference in *average* void diameters. Average pore sizes are calculated from averaging the micropore lifetime, which for samples 1 and 2 is 2.50 ns ± 0.012 ns versus 2.14 ns ± 0.015 ns for samples 3 and 4. Error bars are statistical errors. Because the difference in micropore lifetime of the films deposited under the two plasma conditions is approximately six standard

deviations, or 0.36 ± 0.02 ns, we can say that the two averages are significant. Finally, there is no indication of inhomogeneity with depth for either deposition condition. For example, as the energy of the positron is increased, which probes deeper beneath the film surface as in the case of sample 3, there is no significant difference in the average pore size.

A comparison can also be made between the pore sizes measured with PALS (~0.60 nm) and the pore size estimated by fluorophore-dendrimer incorporation (5.5-6.0 nm) for the films deposited at 55 W, 1000 mTorr and 110°C. The factor of ten difference can be explained by clarifying what the numerical values represent. The value as determined by PALS is an *average* of pore sizes as a function of film depth while the estimated value from diffusion/drift experiments of the fluorophore-labeled dendrimer is indicative of the *upper bound* of pore sizes.

Figures 5.15(c) and (d), which are contour plots of the incorporated Alexa Flour 488® cadaverine and fluorescein dyes, respectively, test the conclusions of the PALS results. The Alexa Fluor® fluorophore, due to its cadaverine group, has an estimated size of slightly greater than 1.0 nm versus about 0.5-0.6 nm for the smaller fluorescein. There is, however, a large difference in the amount of fluorescence detected in that the background intensity for the fluorescein is 120 units, double that of the Alexa Fluor® dye, which has a background similar to the Alexa Fluor®-G2 PAMAM dendrimer conjugate (2.6 nm) (figure 5.15(a)). This indicates that fluorescein is flooding the pores of the *bulk* film and thus is not solely incorporated into defect areas, although regions of higher fluorescence are still present. The unbound Alexa Fluor® dye shows a higher fluorescence intensity within the concentrated "spot" region relative to that observed when the fluorophore is bound to the G2 PAMAM dendrimer, while still retaining a similar background intensity. These results suggest that the Alexa Fluor® is still too large to saturate the bulk of the matrix, but is small enough to create the high intensity regions as seen in the Alexa Fluor®-G2 PAMAM dendrimer conjugate samples. From this, it can

concluded that PALS returns an accurate estimation of the average swelled-state pore size from the bulk of the PEG-like film.

Table 5.5. PALS results for plasma-polymerized PEG films; color shading denotes pairing of films

Sample		Deposition Condition	Freezing Method ($H_2O_{(S)}$)	Beam Energy (keV)	Mean Implantation Depth (nm)	Micropore Lifetime (ns)	Micropore Ps Intensity (%)	Spherical Pore Diameter (nm)
1	a	32 W, 1400 mTorr, 95°C	Freezer (-20°C)	1.2	38	2.2	15.6	0.60
				2.2	100	2.49(3)	14.3	0.65
	b			1.2	38	2.2	15.3	0.60
				2.2	100	2.46(3)	14.2	0.65
				3.2	182	2.49(3)	13.6	0.65
2	a		Liquid N_2	1.2	38	2.3	15.4	0.62
				2.2	100	2.50(3)	14.0	0.65
				3.2	182	2.55(3)	12.6	0.65
	b			1.2	38	2.3	14.2	0.62
				2.2	100	2.49(3)	13.4	0.65
3	a	55 W, 1000 mTorr, 110°C	Freezer (-20°C)	1.2	38	1.9	15.4	0.55
				2.2	100	2.15(3)	14.2	0.60
				3.2	182	2.18(3)	13.2	0.60
4	a		Liquid N_2	1.2	38	1.8	15.6	0.53
				2.2	100	2.13(3)	14.4	0.58
	b			1.2	38	1.9	15.5	0.55
				2.2	100	2.07(3)	14.7	0.58
				3.2	182	2.15(3)	12.9	0.58

5.4 Conclusions

In this chapter, void space sizes of swelled-state, plasma-polymerized polyethylene glycol-like films were estimated using electrophoretic drift and diffusion-controlled transport of PAMAM dendrimers into the bulk of the coating. Prior to incorporation, dendrimer molecules were tagged with Alexa Fluor® 488 fluorescent dye. Matrix-assisted laser desorption-ionization (MALDI) was used to establish coordination between dendrimer and fluorophore, with the generation 2 dendrimer used as a test sample. MALDI results indicate the coordination of a single fluorophore molecule to one

of the sixteen surface groups on the G2 PAMAM dendrimer based on the addition of ~600 m/z units to the blank dendrimer peak at ~4856 m/z. Fluorescence microscopy was used to detect the fluorophore-dendrimer conjugates that had been immobilized via either an electrophoretic drift or diffusion transport mechanism inside the PEG-like film. Images show a homogeneous distribution of bright pockets of fluorescence captured in isolated regions of the sampled area. Statistical analysis of the images was performed by constructing histograms of counts versus intensity data that accounted for all pixels within that image and provided an average intensity for that image. While the differences in the average intensities between samples were small (table 5.2), *t*-tests affirmed that the differences were unique. The bright pockets of fluorescence were attributed to intensities in the high end of the intensity spectrum (figure 5.14).

The total amount of high intensity fluorescence emission provided an alternate standard of comparison for the degree of incorporation of the different-sized dendrimers. Using the total fluorescence count, several inferences about pore size openings of the plasma polymer films can be drawn. First, the similarity in total counts between the diffused- and drift-incorporated G2 PAMAM dendrimers suggest that there is little effect of transport mechanism on the immobilization and that pore size openings of the swelled state plasma films are sufficiently large (>>2.6 nm) to allow free movement into and out of the film. Second, because the largest absolute decrease in counts is observed between the G2 and G5 dendrimer, most pore sizes range between 2.6 and 5.7 nm in diameter, thus indicating a limiting size beyond which molecules are unable to penetrate into the bulk of the film. Third, the majority of void space openings of the plasma film are less than 7.2 nm because the significant charge on the surface group and fluorophore are unable to compensate for molecular size limitations; this is evidenced by the lack of fluorescent counts from the G6 dendrimer. Finally, the transport mechanism is an important factor in establishing fluorescence counts for the G5 dendrimer because an

external force is needed when the penetrant diameter approximately equals the size of the pore opening which was estimated to be ~5.5-6.0 nm.

Contour maps were created to spatially resolve location of fluorescent spots observed for the drifted G2 dendrimer, a blank sample without exposure to fluorophores, and two control fluorophore samples of the unbound Alexa Fluor® 488 cadaverine dye and fluorescein. Comparison of the G2 drifted dendrimer and the blank contour maps indicate that there is an 8-12 intensity unit difference between the two that contributes to the higher average pixel intensity of the drifted G2 dendrimer. By relating the image pixel size with sample area and using a reasonable cutoff point to determine whether a pixel is part of the cluster of pixels accounting for the fluorescent spot observed in an image, the loading capacity of the Alexa Fluor® 488 cadaverine-G2 PAMAM dendrimer conjugate in the PEG-like films was estimated to be ~2.76×10^{-2} μg/mm^2. This model does not relate how much fluorescence emission is generated by a known concentration of fluorophore nor does it account for background emission. The high intensity fluorescence regions correlate well with size dimensions of particles imbedded within the film bulk during the deposition process. Apparently, particles create "defect" areas within the bulk of the film that allow channeling and enhanced incorporation of the fluorophore-dendrimer conjugate.

The average pore size of swelled-state plasma-polymerized PEG-like coatings was determined by PALS as a function of depth. Films deposited at a higher input power, lower pressure, and higher substrate temperature have a ~10% smaller nanopore diameter compared to coatings deposited at lower powers, higher pressures and lower surface temperatures. For films deposited under the same plasma processing conditions, the role of water freezing rate was also investigated. There is little difference in pore size between films exposed to liquid-nitrogen and coatings frozen gradually at -20°C. There is no indication of inhomogeneity with depth for either deposition condition.

Pore sizes measured with PALS were compared with estimates obtained from diffusion/drift experiments of the fluorophore-labeled dendrimers into films deposited at 55 W, 1000 mTorr and 110°C. PALS estimates an average pore size of the swelled-state PEG-like films while previously-conducted immobilization experiments reflect measurement of an upper bound for swelled-state pore sizes. PALS offers a reasonable estimation of the average swelled-state pore size from the bulk of the film because from the contour plots of the incorporated Alexa Flour 488® cadaverine (>1.0 nm) and fluorescein (0.5-0.6 nm) dyes, the background intensity for the fluorescein is 120 units, indicating that fluorescein is flooding the pores of the *bulk* film and not solely being incorporated into defect regions. Rather, this molecule is small enough to penetrate the entire thickness of the film. The Alexa Fluor® is too large to saturate the bulk of the matrix, but is small enough to create the high intensity regions observed in the Alexa Fluor®-G2 PAMAM dendrimer conjugate samples.

5.5 References

1. Das, A.; Ray, A. R., Synthesis and characterization of poly(acrylic acid-co-N-[3-(dimethylamino)propyl]-methacrylamide) hydrogel membranes for biomedical applications. *J. Appl. Polym. Sci.* **2008,** 108, 1273-1280.

2. Kravets, L. I.; Gil'man, A. B.; Drachev, A. I., A study on the water permeability of poly(ethylene terephthalate) track membranes modified by DC discharge polymerization of N,N-dimethylaniline. *High Ener. Chem.* **2005,** 39, 114-122.

3. Ying, L.; Kang, E. T.; Neoh, K. G., Synthesis and characterization of poly(N-isopropylacrylamide)-graft-poly(vinylidene fluoride) copolymers and temperature-sensitive membranes. *Langmuir* **2002,** 18, 6416-6423.

4. Gombotz, W. R.; Wee, S. F., Protein release from alginate matrices. *Adv. Drug Deli. Rev.* **1998,** 31, 267-285.

5. Opila, R. L.; Eng Jr., J., Thin film and interfaces in microelectronics: composition and chemistry as function of depth. *Prog. Surf. Sci.* **2002,** 69, 125-163.

6. Chatham, H., Oxygen diffusion barrier properties of transparent oxide coatings on polymeric substrates. *Surf. Coat. Technol.* **1996,** 78, 1-9.

7. Lewis, J. S.; Weaver, M. S., Thin-film permeation-barrier technology for flexible organic light-emitting devices. *IEEE J. Selec. Topics Quan. Elec.* **2004,** 10, 45-57.

8. Pireaux, J. J.; Delrue, J. P.; Hecq, A.; Dauchet, J. P., *Physicochemical Aspects of Polymer Surfaces*. Plenum: New York, 1983; Vol. 1.

9. Endo, K.; Tatsumi, T., Fluorinated amorphous carbon thin films grown by plasma enhanced chemical vapor deposition for low dielectric constant interlayer dielectrics. *J. Appl. Phys.* **1995,** 78, 1370-1372.

10. Endo, K.; Tatsumi, T., Fluorinated amorphous carbon thin films grown by helicon plasma enhanced chemical vapor deposition for low dielectric constant interlayer dielectrics. *Appl. Phys. Lett.* **1996,** 68, 2864-2866.

11. Cruden, B.; Chu, K.; Gleason, K.; Sawin, H., Thermal decomposition of low dielectric constant pulsed plasma fluorocarbon films: I. Effect of precursors and substrate temperature. *J. Electrochem. Soc.* **1999,** 146, 4590-4596.

12. Cruden, B.; Chu, K.; Gleason, K.; Sawin, H., Thermal decomposition of low dielectric constant pulsed plasma fluorocarbon films: II. Effect of postdeposition annealing and ambients. *J. Electrochem. Soc.* **1999,** 146, 4597-4604.

13. Rossi, G., Effect of local flaws in polymeric permeation reducing barriers. *J. Appl. Phys.* **1993,** 74, 5471-5475.

14. Hanika, M.; Langowski, H.-C.; Moosheimer, U.; Peukert, W., Inorganic layers on polymeric films—Influence of defects and morphology on barrier properties. *Chem. Eng. Technol.* **2003,** 26, 605-614.

15. da Silva Sobrinho, A. S.; Czeremuszkin, G.; Latreche, M.; Wertheimer, M. R., Defect-permeation correlation for ultrathin transparent barrier coatings on polymers. *J. Vac. Sci. Technol. A* **2000,** 18, 149-157.

16. Tropsha, Y. G.; Harvey, N. G., Activated rate theory treatment of oxygen and water transport through silicon oxide/ poly(ethylene terephthalate) composite barrier structures. *J. Phys. Chem. B* **1997,** 101, 2259-2266.

17. Tomalia, D. A.; Baker, H.; Dewald, J.; Hall, M.; Kallos, G.; Martin, S.; Roeck, J.; Ryder, J.; Smith, P., A new class of polymers - starburst-dendritic macromolecules. *Polym. J.* **1985,** 17, 117-132.

18. Wu, H.; Liu, Z.; Wang, X.; Zhao, B.; Zhang, J.; Li, C., Preparation of hollow capsule-stabilized gold nanoparticles through the encapsulation of the dendrimer. *J. Coll. Inter. Sci.* **2006,** 302, 142-148.

19. Mak, C. C.; Chow, H. F., Dendritic catalysts: reactivity and mechanism of the dendritic bis(oxazoline) metal complex catalyzed diels-alder reaction. *Macromolecules* **1997,** 30, 1228-1230.

20. Karthaus, O.; Ijiro, K.; Shimomura, M., Monomolecular layers of diarylethene-containing dendrimers. *Langmuir* **1996,** 12, 6714-6716.

21. Svenson, S.; Tomalia, D. A., Dendrimers in biomedical applications - reflections on the field. *Adv. Drug Deli. Rev.* **2005,** 57, 2106-2129.

22. Patri, A. K.; Majoros, I. J.; Baker, J. J., Dendritic polymer macromolecular carriers for drug delivery *Curr. Opin. Chem. Biol.* **2002,** 6, 466-471.

23. D'Emanuele, A.; Attwood, D., Dendrimer-drug interactions. *Adv. Drug Deli. Rev.* **2005,** 57, 2147-2162.

24. Kim, Y.; Zimmerman, S. C., Applications of dendrimers in bio-organic chemistry. *Curr. Opin. Chem. Biol.* **1998,** 2, 733-742.

25. Wiwattanapatapee, R.; Carreno-Gomez, B.; Malik, N.; Duncan, R., Anionic PAMAM dendrimers rapidly cross adult rat intestine in vitro: A potential oral delivery system? *Pharma. Research* **2000,** 17, 991-998.

26. Tomalia, D. A., Birth of a new macromolecular architecture: dendrimers as quantized building blocks for nanoscale synthetic polymer chemistry. *Prog. Polym. Sci.* **2005,** 30, 294-324.

27. Welch, P.; Muthukumar, M., Tuning the density profile of dendritic polyelectrolytes. *Macromolecules* **1998,** 31, 5892-5897.

28. Koyama, Y.; Talanov, V. S.; Bernardo, M.; Hama, Y.; Regino, C. A. S.; Brechbiel, M. W.; Choyke, P. L.; Kobayashi, H., A dendrimer-based nanosized contrast agent dual-labeled for magnetic resonance and optical fluorescence imaging to localize the sentinel lymph node in mice. *J. Magnet. Reson. Imag.* **2007,** 25, 866-871.

29. Talanov, V. S.; Regino, C. A. S.; Kobayashi, H.; Bernardo, M.; Choyke, P. L.; Brechbiel, M. W., Dendrimer-based nanoprobe for dual modality magnetic resonance and fluorescence imaging. *Nano Lett.* **2006,** 6, 1459-1463.

30. Yoo, H.; Juliano, R. L., Enhanced delivery of antisense oligonucleotides with fluorophore-conjugated PAMAM dendrimers. *Nucleic Acids Research* **2000,** 28, 4225-4231.

31. Balzani, V.; Ceroni, P.; Gestermann, S.; Gorka, M.; Kauffmann, C.; Vogtle, F., Fluorescent guests hosted in fluorescent dendrimers. *Tetrahedron* **2002,** 58, 629-637.

32. Ghosh, S.; Banthia, A. K., Fluorophore-labeled polyamidoamine (PAMAM) dendritic architectures: Synthesis and fluorescence sensing properties. *Supramol. Chem.* **2004,** 16, 487-494.

33. Balzani, V.; Ceroni, P.; Gestermann, S.; Kauffmann, C.; Gorka, M.; Vogtle, F., Dendrimers as fluorescent sensors with signal amplification. *Chem. Commun.* **2000,** 10, 853-854.

34. Ong, K. K.; Jenkins, A. L.; Cheng, R.; Tomalia, D. A.; Durst, H. D.; Jensen, J. L.; Emanuel, P. A.; Swim, C. R.; Yin, R., Dendrimer enhanced immunosensors for biological detection. *Anal. Chim. Acta* **2001,** 444, 143-148.

35. Quintana, A.; Raczka, E.; Piehler, L.; Lee, I.; Myc, A.; Majoros, I.; Patri, A. K.; Thomas, T.; Mule, J.; Baker Jr., J. R., Design and function of a dendrimer-based therapeutic nanodevice targeted to tumor cells through the folate receptor. *Pharma. Research* **2002,** 19, 1310-1316.

36. Giordanengo, R.; Mazarin, M.; Wu, J.; Peng, L.; Charles, L., Propagation of structural deviations of poly(amidoamine) fan-shape dendrimers (generations 0–3) characterized by MALDI and electrospray mass spectrometry. *Int. J. Mass Spec.* **2007,** 266, 62-75.

37. Brothers II, H. M.; Piehler, L. T.; Tomalia, D. A., Slab-gel and capillary electrophoretic characterization of polyamidoamine dendrimers. *J. Chromat. A* **1998,** 814, 233-246.

38. Welch, C. F.; Hoagland, D. A., The electrophoretic mobility of PPI dendrimers: Do charged dendrimers behave as linear polyelectrolytes or charged spheres? *Langmuir* **2003,** 19, 1082-1088.

39. Hudson, R. H. E.; Damba, M. J., Nucleic acid dendrimers: Novel biopolymer structures. *J. Amer. Chem. Soc.* **1993,** 115, 2119-2124.

40. Kukowska-Latallo, J. F.; Bielinska, A. U.; Johnson, J.; Spindler, R.; Tomalia, D. A.; Baker Jr., J. R., Efficient transfer of genetic material into mammalian cells using starburst polyamidoamine dendrimers. *Proc. Natl. Acad. Sci.* **1996,** 93, 4897-4902.

41. Kitchens, K. M.; El-Sayed, M. E. H.; Ghandehari, H., Transepithelial and endothelial transport of poly(amidoamine) dendrimers. *Adv. Drug Deli. Rev.* **2005,** 57, 2163-2176.

42. Sakthivel, T.; Toth, I.; Florence, A. T., Distribution of a lipidic 2.5 nm diameter dendrimer carrier after oral administration. *Int. J. Pharm.* **1999,** 183, 51-55.

43. Hermanson, G. T., *Bioconjugate Techniques*. Academic Press, Inc.: San Diego, 1996.

44. Dass, C., *Fundamentals of Contemporary Mass Spectroscopy*. Wiley-Interscience: Hoboken, N.J., 2007; p 585.

45. Russel, W. B.; Saville, D. A.; Schowalter, W. R., *Colloidal Dispersions*. Cambridge University Press: New York, 1989; p 525.

46. Morosoff, N., An Introduction to Plasma Polymerization. In *Plasma Deposition, Treatment, and Etching of Polymers*, d'Agostino, R., Ed. Academic Press, Inc.: San Diego, 1990.

47. Sachs, L., *Applied Statistics, A Handbook of Techniques*. 2nd ed.; Springer-Verlag: New York, 1984; p 707.

CHAPTER 6

CONCLUSIONS AND FUTURE WORK

6.1 Conclusions

A parallel-plate capacitively-coupled plasma deposition system was designed and built for the growth of polyethylene glycol-like films. Deposition rates and bonding structures were characterized as a function of input RF power, reactor pressure and substrate temperature to provide information on the relationship between plasma parameters invoked and the film properties. Deposition rates increased at the higher power input due to larger average electron energies, a higher probability of inelastic collisions and therefore higher neutral species generation and electron and ion current densities. Deposition rate as a function of pressure goes through a maximum due to the competition between the frequency of inelastic collisions (at lower pressures) and the energy transfer per collision (at higher pressures). However, over the parametric range studied in this work, deposition rate increased with increasing pressure. Deposition rate increased with a decrease in sample temperature which is indicative of an adsorption-limited process. The plasma-polymerized PEG-like coatings synthesized in this study resembled higher molecular weight solution-polymerized films that have a more highly crosslinked structure (higher refractive indices), consistent with the presence of a plasma atmosphere.

The relationship between deposition conditions and film behavior in aqueous media was also examined by studying deposited film structure and how the presence of particles (defects) can be used as an additional indicator of film crosslink density, and in turn, dissolution and swelling behavior. At constant operating pressures and substrate temperatures, higher applied powers yield a more highly crosslinked, stable film due to an increased electron density, higher collision rates, increased ionic and radical species

concentrations, and an enhanced ion and electron bombardment flux. The irregularly-shaped particles entrapped within the film appear to be generated by both heterogeneous and homogeneous growth. Higher crosslinked films have a greater ability to retain entrapped species and dissolve slower. Films grown at lower pressures have a greater crosslink density and increased stability to dissolution because of fewer collisions in the gas phase and an increase in average electron and ion energy when impinging on the growing film surface. At higher substrate temperatures, surface mobility of adsorbed fragments increases, desorption increases and thus the net deposition rate decreases. The frequency of chemical reactions and bond rearrangements increase with temperature, resulting in an increase in crosslink density and a decrease in dissolution rate. Extent of swelling for plasma-polymerized films is also a function of crosslink density. Particles contribute to an increased diffusivity of water molecules due to an inhomogeneous film crosslink density and thus decreased tortuosity for the penetrant. Lateral diffusion can occur for defects spaced too close together and lead to dissolution in liquid water or swelling in the presence of water vapor. For both phenomena, imbedded particles, incorporated by either homogeneous or heterogeneous growth, control the behavior of the bulk film to water exposure.

Finally, the pore sizes of the swelled-state, plasma-polymerized PEG-like films were determined using both transport of fluorophore-tagged PAMAM dendrimers (electrophoretic drift- and diffusion-controlled) and positron annihilation lifetime spectroscopy (PALS) to probe the bulk of the film. PAMAM dendrimers were used because of their well-defined sizes and negatively-charged succinamic acid surface groups. Prior to incorporation, the dendrimer was tagged with fluorescent dye, with the coordination between the two molecules detected using matrix-assisted laser desorption-ionization (MALDI). Fluorescence microscopy was used to detect the immobilized fluorophore-dendrimer complexes inside the film and statistical analysis of the images allowed an estimation of the upper bound of pore size openings of the plasma polymer

coatings. Fluorescence studies of the diffused and drifted G2 dendrimers suggest a free movement of the molecule into and out of the film due to void openings much larger than its characteristic size (2.6 nm). Due to the lack of detected fluorescence from either the diffused or drifted G6 dendrimer, it was concluded that the applied electric field was insufficient to compensate for molecular size, and that the majority of void space openings of the plasma film are less than 7.2 nm. Finally, from the large differences in fluorescence counts between the diffused and drifted G5 dendrimer, it was determined that the upper bound of pore size was roughly equal to that of the penetrant (~5.5-6.0 nm). The loading capacity of the Alexa Fluor® 488 cadaverine-G2 PAMAM dendrimer conjugate in the PEG-like films was estimated to be ~2.76×10^{-2} μg/mm^2, which was determined using contour maps to help resolve the location and spread of the fluorescent spots. Image pixel size was related to sample area and a cutoff intensity was used to determine the location of the pixel clusters accounting for the localized spots. This model was not calibrated for how much fluorescence emission is generated by a known concentration of fluorophore nor does it account for background emission. The high intensity fluorescence regions correlate with size dimensions of imbedded particles that create "defect" areas within the bulk film and allow channeling to enhance incorporation of the fluorophore-dendrimer conjugate.

Average pore sizes of swelled-state plasma-polymerized PEG-like coatings were determined by PALS as a function of depth. Films deposited at a higher input power, lower pressure, and higher substrate temperature have a ~10% smaller nanopore diameter compared to coatings deposited at lower powers, higher pressures and lower surface temperatures. The contour plots of the incorporated Alexa Flour 488® cadaverine and fluorescein dyes indicate that, because the fluorescein floods the bulk film pores and is not solely restricted to defect regions while the Alex Fluor® is confined to the larger defect areas, the fluorescein is small enough to penetrate the entire thickness of the film.

Thus, the PALS data is a reasonable estimation of the average swelled-state bulk pore size.

6.2 Future Work

In this thesis, we have determined estimates for the *upper bound* of pore sizes in plasma-polymerized PEG-like films using a combination of electrophoretic drift and diffusion transport of size-controlled PAMAM dendrimers (Chapter 5). In addition, we compared these results with *average* pore size of the plasma films as a function of depth using positron annihilation lifetime spectroscopy (PALS) (Appendix A). However, due to the nature of the deposition process, growth of plasma-deposited films results in a *distribution* of pore sizes.[1] One method to investigate this further, is by using *in*-situ ellipsometry.[2, 3] Ellipsometric porosimetry utilizes the change in optical properties of the mesoporous film during vapor adsorption and desorption to determine the mass of an absorbant that is condensed or absorbed into the pores. Calculation of physical parameters such as pore size may be conducted using various fitting equations (e.g. Lorentz–Lorenz, Newton–Laplace, Bragg–Pippard, etc.).[4, 5] This technique offers several advantages including: (1) films may be deposited on any smooth surface (e.g. silicon, gold), (2) a minimal surface area of ~1 mm^2 is required, (3) real-time structural changes of the film can be detected during the absorption/desorption process (e.g. pore size versus time data in response to film swelling), (4) calculation of mean pore length from effective pore volume[6], and (5) measurements are performed at room temperature for pores 2-25 nm in diameter. Ellipsometric porosimetry is advantageous for our PEG-like films because sample preparation requirements can be satisfied for plasma deposition processes and initial experiments may be performed using the *in*-situ ellipsometry cell described in Chapter 4.

In order to utilize the plasma-polymerized PEG-like materials in drug-eluting applications, it is important to test the incorporation amount and time-dependent release

kinetics of potential drug molecules. From Chapter 5, we have described our estimations of the largest available swelled-state openings through which molecules can penetrate. We have also established a baseline for the estimated loading amount of a molecule ~2.6 nm in diameter. Using this information and the electrophoretic drift technique, loading concentrations can be established by tagging other potential molecules with fluorophores and tracking their release behavior from the films in water or buffer solution by measuring the decay in fluorescence of the fluorophore-labeled penetrant with time. Simultaneous ellipsometry measurements will help establish whether release is due to film degradation or diffusion of molecules through the pore size openings. Initially, release kinetics of the incorporated dendrimer molecules should be established because dendrimer-film interactions have been previously determined (Chapter 5) and dendrimers themselves may be used as drug carriers.[7-9] Testing discharge kinetics of paclitaxel and sirolimus from the plasma polymer films can also be compared to previous release studies from various reservoirs.[10-14]

From the property studies detailed in Chapters 3 and 4, we have described the synthesis and characterization of pseudo-hydrogels that have controllable dissolution and swelling properties. A good comparison to our customized films would be to solution-polymerized PEG or PEG-based hydrogel coatings. This is especially useful in stability comparisons during electrophoretic immobilizations of alternative molecules. Plasma polymerized films have been shown (Chapter 5) to be stable enough to withstand the applied voltage and thus electric field during the incorporation process due to high crosslink densities. Another aspect to investigate would be the mechanism for drug release between the plasma- and solution-polymerized networks. Plasma films, as was shown in Chapter 4, can have tunable dissolution properties and therefore, can in principle, deliver molecules based on both release mechanisms. Pure hydrogels are expected to elute molecules via diffusive transport.

Barrier films are another potential application for the films used in this study. Water permeation through our plasma-polymerized PEG-like films were investigated in Chapter 4; however, an alternative might be to use a quartz crystal microbalance with dissipation (QCM-D) technique to numerically determine the mass of water uptake by films deposited under different plasma environments.[15] Based on dissolution and swelling behavior, we expect that the total mass of water will decrease with increasing applied power and temperature and decreasing operating pressure. Additionally, QCM-D also provides structural information and viscoelastic properties (rigidity) that should offer insight into film crosslink density. Once the mass has been determined, flux calculations can be performed to track water permeation through films deposited under different conditions.

6.3 References

1. Morosoff, N., An Introduction to Plasma Polymerization. In *Plasma Deposition, Treatment, and Etching of Polymers*, d'Agostino, R., Ed. Academic Press, Inc.: San Diego, 1990.

2. Dultsev, F. N.; Baklanov, M. R., Nondestructive determination of pore size distribution in thin films deposited on solid substrates. *Electro. Solid State Let.* **1999,** 2, 192-194.

3. Baklanov, M. R.; Mogilnikov, K. P.; Polovinkin, V. G.; Dultsev, F. N., Determination of pore size distribution in thin films by ellipsometric porosimetry. *J. Vac. Sci. Technol. B* **2000,** 18, 1385-1391.

4. Muranova, G. A.; Perveev, A. F., Microporosity of thin-films. *Sov. J. Opt. Technol.* **1993,** 60, 91-100.

5. Sing, K. S. W.; Everett, D. H.; Haul, R. A. W.; Moscou, L.; Pierotti, R. A.; Rouquerol, J.; Siemieniewska, T., Reporting physisorption data for gas/solid systems with special reference to the determination of surface area and porosity. *Pure & Appl. Chem.* **1985,** 57, 603-619.

6. Baklanov, M. R.; Vasilyeva, L. L.; Gavrilova, T. A.; Dultsev, F. N.; Mogilnikov, K. P.; Nenasheva, L. A., Porous structure of SiO_2 films synthesized at low temperature and pressure. *Thin Solid Films* **1989,** 171, 43-52.

7. D'Emanuele, A.; Attwood, D., Dendrimer-drug interactions. *Adv. Drug Deli. Rev.* **2005,** 57, 2147-2162.

8. Dhanikula, R. S.; Hildgen, P., Synthesis and evaluation of novel dendrimers with a hydrophilic interior as nanocarriers for drug delivery. *Bioconjugate Chem.* **2006,** 17, 29-41.

9. Jansen, J. F. G. A.; de Brabander-van den Berg, E. M. M.; Meijer, E. W., Encapsulation of guest molecules into a dendritic box. *Science* **1994,** 266, 1226-1229.

10. Dong, Y.; Zhang, Z.; Feng, S.-S., d-alpha-Tocopheryl polyethylene glycol 1000 succinate (TPGS) modified poly(l-lactide) (PLLA) films for localized delivery of paclitaxel. *Int. J. Pharm.* **2008,** 350, 166-171.

11. Huang, L.-Y.; Yang, M.-C., Behaviors of controlled drug release of magnetic-gelatin hydrogel coated stainless steel for drug-eluting-stents application. *J. Magnetism Magnetic Mater.* **2007,** 310, 2874-2876.

12. Livnat, M.; Beyar, R.; Seliktar, D., Endoluminal hydrogel films made of alginate and polyethylene glycol: Physical characteristics and drug-eluting properties. *J. Biomed. Mat. Research Part A* **2005,** 75, 710-722.

13. Colombo, A.; Drzewiecki, J.; Banning, A.; Grube, E.; Hauptmann, K.; Silber, S.; Dudek, D.; Fort, S.; Schiele, F.; Zmudka, K.; Guagliumi, G.; Russell, M. E., Randomized study to assess the effectiveness of slow- and moderate-release polymer-based paclitaxel-eluting stents for coronary artery lesions. *Circulation* **2003,** 108, 788-794.

14. Farb, A.; Heller, P. F.; Shroff, S.; Cheng, L.; Kolodgie, F. D.; Carter, A. J.; Scott, D. S.; Froehlich, J.; Virmani, R., Pathological analysis of local delivery of paclitaxel via a polymer-coated stent. *Circulation* **2001,** 104, 473-479.

15. Tamirisa, P. A.; Hess, D. W., Water and moisture uptake by plasma polymerized thermoresponsive hydrogel films. *Macromolecules* **2006,** 39, 7092-7097.

APPENDIX A

CHEMICAL TESTS FOR DETERMINATION OF CARBONYL GROUP IDENTITY IN PLASMA-POLYMERIZED PEG-LIKE HYDROGEL THIN FILMS

A.1 Introduction

Fourier transform infrared spectra of PEG-like coatings indicate structural inconsistencies as compared to PEG materials synthesized by traditional solution polymerization methods.[1] As addressed in Chapter 3, a peak at 1735 cm^{-1} indicated the presence of a carbonyl group, although it was unclear whether the peak was due to ketone, aldehyde, carboxylic acid or ester functionalities (table 3.3). It was hypothesized that the formation of ketones and esters may be more likely due to the existence of C-O-C linkages in the precursor structure and that aldehydes and acids, which signify chain termination, were unlikely to cause the majority of carbonyl moieties in the film. Based on the premise that ketones and esters are the most likely functionalities present, in this section we describe attempts to understand the nature of the carbonyl group by conducting common identification tests to detect the presence of ketones and aldehydes.[2]

A.2 Brady's Test for Detection of Ketones and Aldehydes

Brady's reagent was prepared by first dissolving 3 g of 2,4-dinitrophenylhydrazine (Sigma Aldrich) in 15 mL of concentrated sulfuric acid, then adding this mixture to a water (20 mL) – ethanol (70 mL) solution and finally filtering any precipitates. The presence of a ketone or an aldehyde is confirmed if a color change is detected upon exposure of Brady's reagent to the unknown compound. The chemical reaction stimulating this color change is detailed in figure A.1.

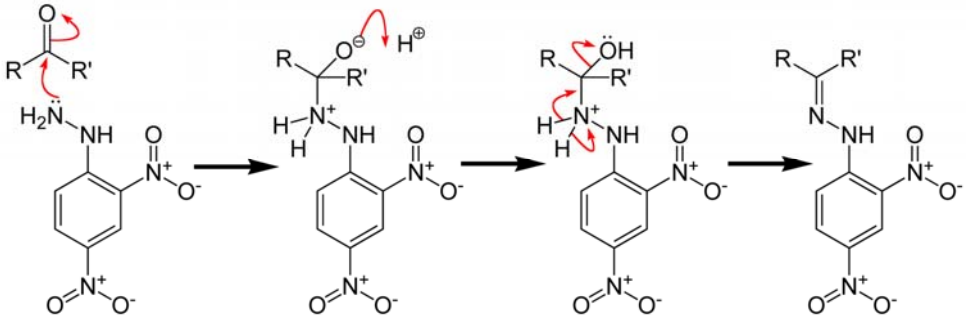

Figure A.1. Mechanism for the reaction between 2,4-dinitrophenylhydrazine and a ketone or an aldehyde

Typically, dinitrophenylhydrazones (final product) of ketones or aldehydes are yellow in color when carbonyl groups are not conjugated with another functional group and orange-red when conjugated with a carbon-carbon double bond or benzene ring. Figure A.2 shows the color test results of (a) as-synthesized Brady's reagent; (b) Brady's reagent upon exposure to films deposited at 32 W, 1400 mTorr, 95°C; (c) Brady's reagent upon exposure to films deposited at 55 W, 1000 mTorr, 110°C; and (d) side-by-side comparison of the two films. It is difficult to confirm a positive test for either type of film because the color of Brady's reagent is similar before and after exposure to the PEG-like thin films. A yellowish tint is seen, indicating an unconjugated carbonyl group; however, the FTIR peak at 1582 cm^{-1} in table 3.3 suggests the presence of carbon-carbon double bonds. An orange or red color is difficult to interpret because of possible contamination by the original 2,4-dinitrophenylhydrazine starting material, which is also orange-red in color. In addition, figure A.1 is stoichiometric, making it unlikely that ~250 nm thick film would cause a dramatic color change of the reaction media (~100 mL) even with the presence of carbonyl groups. Finally, an unknown precipitate is also observed, which originally was thought to be due to contaminants since dinitrophenylhydrazones are soluble in this acid-water-ethanol solution. Ultimately, it was determined that the precipitate was due to the silicon wafer and not the polymer coating because when the bare substrate was stored in Brady's reagent, the same

cloudiness appeared. These results suggest that a reaction may be taking place between Brady's reagent and the silicon substrate and thereby causing the contamination observed in the sample.

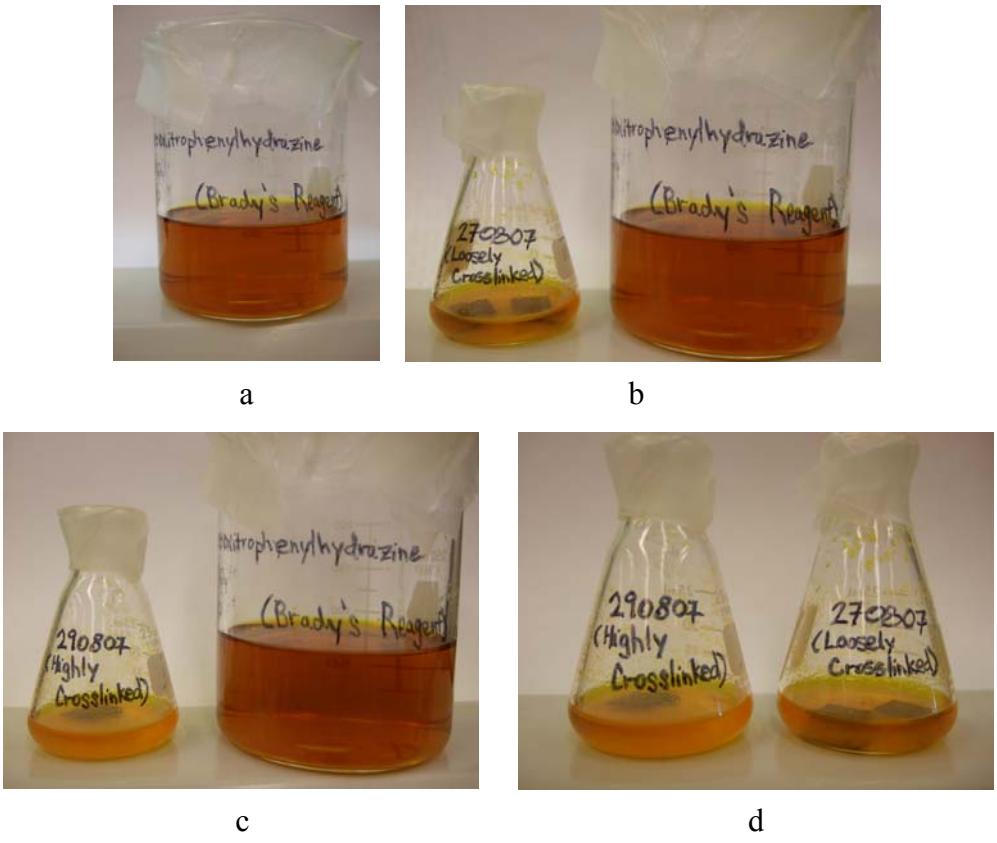

Figure A.2. Color test results of (a) Brady's reagent; (b) Brady's reagent after reaction with films deposited at 32 W, 1400 mTorr, 95°C; (c) Brady's reagent after reaction with films deposited at 55 W, 1000 mTorr, 110°C; and (d) side-by-side comparison of the two coatings.

A.3 Schiff's Test for Detection of Aldehydes

Schiff's reagent was purchased from Sigma Aldrich as a clear, colorless liquid and tested with the PEG-like films to determine the presence of aldehydes in the coating. Figure A.3 shows the synthesis of Schiff's reagent followed by its reaction with an aldehyde. Schiff's reagent is synthesized by reaction of fuchsin, a pink triphenylmethane dye, with sulfurous acid to form leucosulfonic acid; reaction of this acid with an aldehyde yields a violet-purple product. Figure A.4 shows the resulting solution after reaction of

leucosulfonic acid with *o*-phthaldialdehyde to identify color changes, and the results of our color tests with PEG-like coatings.

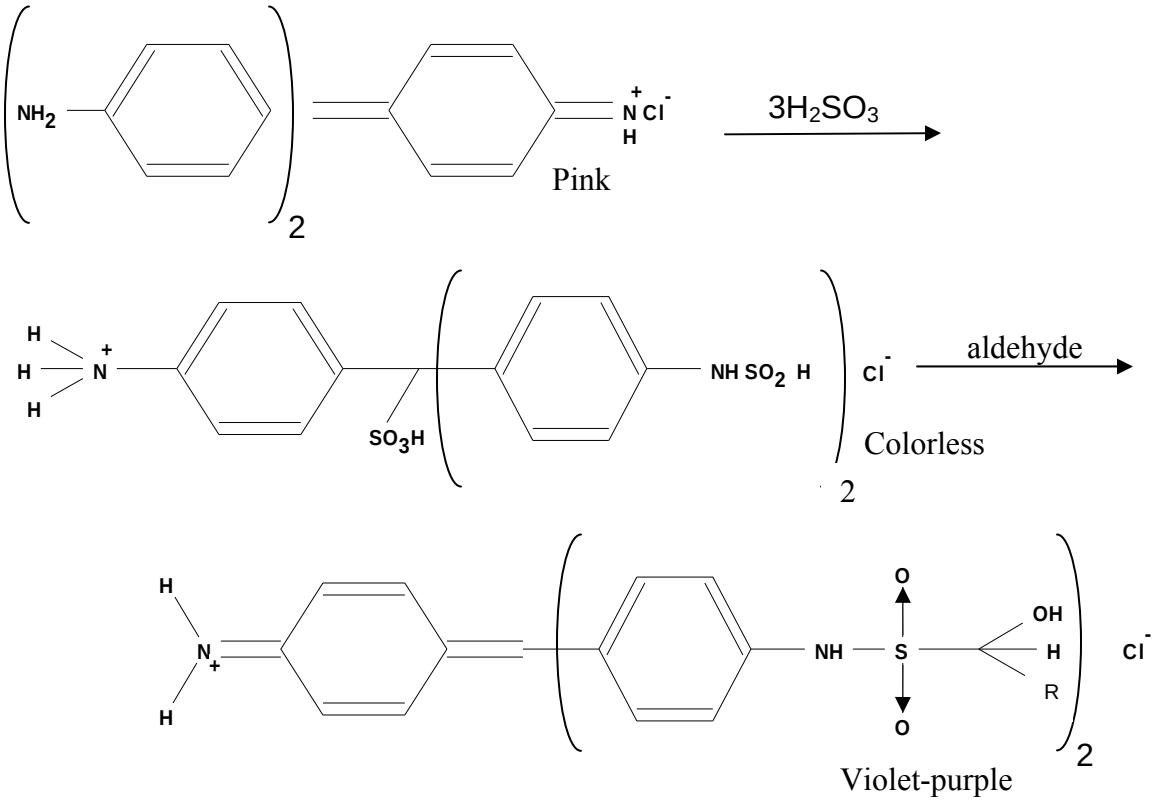

Figure A.3. Mechanism for (1) the synthesis of Schiff's reagent and (2) the reaction between Schiff's reagent and an aldehyde

a b

Figure A.4. Schiff's test results for (a) reaction with *o*-phthaldialdehyde and (b) reaction with plasma-polymerized PEG-like films deposited at 55 W, 1000 mTorr, 110°C (left) and 32 W, 1400 mTorr, 95°C (right)

Figure A.4(a) affirms the characteristic violet-purple color indicative of the Schiff's reagent reaction with an aldehyde, however a clear, colorless liquid remains upon exposure of the PEG-like films to leucosulfonic acid. This suggests one of two possibilities: (1) that there are no aldehyde moieties present in the film, or (2) that the concentration of aldehydes is too low (e.g. insufficient amount of material) to be visually detected. Because Schiff's test is also a stoichiometric reaction, we can conclude that there is an insufficient amount of material to confirm a negative identity test.

A.4 Tollens Test for Detection of Aldehydes

Tollens reagent was prepared by adding 2 mL of a 5% solution of silver nitrate to a clean flask and diluting with one drop of 10% sodium hydroxide solution. A 2% ammonia solution was then added dropwise and gently shaken until all silver oxide precipitate dissolved. Reaction of an aldehyde with Tollens reagent should yield a smooth silver deposit along the interior of the glassware as described by figure A.5.

$$RCHO + 2Ag(NH_3)_2OH \rightarrow 2Ag(s) + RCOONH_4 + H_2O + 3NH_3$$

Figure A.5. Tollens reagent reaction with an aldehyde to form silver precipitate

While the results of the Tollens test (Figure A.6) do not indicate the presence of aldehyde groups and thus corroborate the negative results of the Schiff's test, the question remains whether there is sufficient aldehyde present in the film or film surface to allow detection or whether the coatings lack aldehyde groups.

Figure A.6. Negative Tollens test for the presence of aldehyde groups in plasma-polymerized films deposited at 55 W, 1000 mTorr, 110°C (left) and 32 W, 1400 mTorr, 95°C (right)

A.5 Conclusions

In this section an attempt was made to identify the carbonyl group present in our plasma-polymerized PEG-like coatings. This was investigated by conducting Brady's test, Schiff's test, and Tollens test on films deposited at 55 W, 1000 mTorr, 110°C and 32 W, 1400 mTorr, 95°C to detect for the presence of ketones and aldehydes. We expect that the predominant barrier in making conclusive statements regarding the presence of these moieties is a lack of sufficient material for visual detection.

A.6 References

1. Pouchert, C. J., *The Aldrich Library of FT-IR Spectra*. 2nd ed.; Aldrich: Milwaukee, 1997.

2. Shriner, R. L.; Fuson, R. C.; Curtin, D. Y.; Morrill, T. C., *The Systematic Identification of Organic Compounds*. 6th ed.; John Wiley & Sons: New York, 1980.

APPENDIX B

POLYETHYLENE GLYCOL HYDROGEL DEPOSITION EXPERIMENTAL PROTOCOL

B.1 Preliminary System Setup

B.1.1 Chamber Heating

The deposition system is heated with cartridge heaters (lower electrode) and heating tape controlled by eight variable transformers (variacs). Begin by turning on variacs that heat the six sides of the chamber (labeled: 'viewport', 'top', 'pressure', 'bottom', 'inlet' and 'vacuum') and the flexible stainless steel tubing that is attached to the throttle valve (labeled: 'pump inlet'). Heating the chamber leads to an increase in temperature of the bottom electrode as well; therefore, variac settings can be calibrated to obtain a specific bottom electrode temperature, T_{var}. Settings are identified in table B.1.

Table B.1. Effect of variac settings on bottom electrode temperature

Variac	Setting for a bottom electrode temperature of ~106°C (V)	Setting for a bottom electrode temperature of ~85°C (V)
Viewport	90	90
Top	82.5	68.5
Pressure	82.5	68.5
Bottom	82.5	67
Inlet	82.5	68.5
Vacuum	82.5	67
Pump inlet	110	110
Gas line	110	110

Any additional heating to account for differences between T_{var} and operating temperature, T_{oper}, were addressed with insert cartridge heaters in the bottom electrode. For cautionary purposes, allow system to heat overnight. Once the heated system has been given sufficient time to equilibrate, turn on temperature controller and set to the designated operating condition. Allow 15-20 minutes to stabilize.

B.1.2 Loading Samples

In order to load samples for deposition, the reactor must be brought to atmospheric pressure. Close throttle valve and flow nitrogen into the chamber by opening regulator valves leading from the cylinder and turning on the designated flow controller. Set flowrates to a maximum of 200 standard cubic centimeters per minute (sccm). This is especially important when unloading samples because at higher flow rates, substrates can be blow off the grounded electrode by convective flow. When the chamber has fully vented, close all nitrogen valves, starting from the cylinder and working towards the reactor. This ensures that gas lines are clear to prevent residual gases or vapors from contaminating the system. After the samples are loaded, close viewport and slowly (incrementally) begin opening the throttle valve. This prevents the substrate from blowing off the electrode and helps to avoid damage to the roughing pump. Pump down system to base pressure (~15-25 mTorr).

B.2 Oxygen Plasma Cleaning of Substrate

Oxygen plasmas are used for cleaning organic contaminants from chamber sidewalls, electrode surfaces and substrate surfaces. Turn on oxygen supply in the same manner as nitrogen and set flow to 145 sccm. With the throttle valve completely open, reactor pressure should range between 280 and 300 mTorr. Allow oxygen to flow for 3 minutes. Close throttle valve until pressure reaches operating pressure. Turn on signal generator, frequency counter and amplifier. A power setting on the signal generator of -

9.0 dBm inputs ~55 W on the powered electrode and while -12.0 dBm inputs ~32 W. After a glow discharge is struck, pressure will rise slightly due to additional vapor species formed from molecular dissociation during inelastic collisions with electrons. Adjust the throttle valve to stabilize at the designated operating pressure. Slowly adjust the transmitter and antenna matching knobs on the Heathkit SA-2060A impedance matching network until the reflected power, as observed from the Bird Electronics Wattmeter, reads zero. Record this setting, as parameters are unlikely to significantly change in future runs. The inductor knob should remain constant at a setting of '026'. Monitor system pressure and electrode temperature for the duration of the run. Turn off power to amplifier after two minutes and continue to run oxygen through the system for an additional 3 minutes. Close all oxygen valves and slowly open throttle valve to return system to base pressure.

B.3 Polymerization of Tetraethylene Glycol Dimethyl Ether

Start by turning on the variac labeled 'gas line' and begin heating monomer with a variac setting of 60 V. Gas line heating should equilibrate to a stabilized temperature in 15-20 minutes. Begin flowing argon into the chamber at a flowrate of 75 sccm. With the throttle valve completely open, reactor pressure should range between 170-180 mTorr. Record this pressure. Allow argon to flow for 3 minutes. For depositions conducted at 1000 mTorr, close throttle valve until the reactor pressure reaches ~450 mTorr. For depositions conducted at 1400 mTorr, close the throttle valve until the reactor pressure reaches ~900 mTorr. Record this pressure. After the temperature of the TGDE reactant reaches 148°C, slowly start opening the flask valve. Flow relies on pressure differences between the inside of the monomer flask and the vacuum system. Opening the flask too fast results in pressure equilibration and no net flow. Pressure increases resulting from TGDE flow will fluctuate somewhat; however, a good indicator of when to ignite the

discharge is whether condensation appears on the viewport. Typically, a pressure increase of 20-30 mTorr is seen. Record this pressure.

TGDE discharges are dark blue/purple in color while argon plasmas are white. Color differentiation allows qualitative determination of monomer concentrations. As pressure begins to rise, manipulate the throttle valve to stabilize at the selected operating pressure. As with oxygen, adjust transmitter and antenna matching knobs on the impedance matching network until the reflected power reads zero. Monitor electrode temperature, chamber pressure, reflected power, temperature of monomer, and color of plasma. Temperature of TGDE should stay within 4-5 degrees of 148°C. Stable TGDE temperatures indicate constant flows to the chamber. Record the final monomer temperature after ending the run. After the allotted deposition time, turn off plasma power, stop flow of TGDE to the chamber by closing the flask valve, turn off heating to the monomer flask and slowly open the throttle valve. Continue running argon through the system for at least 15 minutes. Stop all argon flow. To unload samples, close the throttle valve and vent to atmosphere using nitrogen.

B.4 Shutdown Checklist

To ensure proper shutdown, make sure cylinder regulator valves and all plug valves between cylinder and mass flow controllers (MFC) are closed. All power and flow equipment including the signal generator, frequency counter, amplifier and flow readout should be turned off. Temperature controller, monomer flask variac and monomer flask temperature readout should be turned off and the flask valve closed. The chamber is kept idle at ambient temperature and base pressure so all variacs for system heating should also be turned off and the throttle valve left open. Finally, since the mass flow controllers regulate gas flow to other reactor systems, make sure that the plug valve located immediately after the MFCs and leading to the PEG reactor is closed.

B.5 Restocking Monomer Supply

Confirm that the flask valve is securely tightened (over-tightening will cause air leaks). Isolate the monomer container by switching the quarter-turn plug valve closest to the flask to the 'closed' position. Detach the flask from the Swagelok tubing and refill TGDE so that the flask is slightly less than half full. Excessive monomer will yield inconsistent flowrates during deposition. Re-attach the flask with fresh TGDE back to the system, making certain that all valves and inlets are closed. First open the plug valve. Pressure will spike dramatically due to trapped air between the flask valve and the plug valve; allow air to pump from system. Slowly begin exposing flask contents to vacuum by opening the flask valve. Leave flask contents exposed to vacuum for 15-20 minutes to permit trapped air in the TGDE to escape. For the first run after restocking the monomer, heating allows a complete purge of air from the precursor and results in large increases in pressure. For this preliminary deposition, do not strike the discharge until condensate is seen on the viewport.

VITA

SHANTANU C. PATHAK

Shantanu Pathak was born on the 19th of June, 1982 to Udaya and Sudha Pathak. After graduating high school in 2000, he attended the University of Illinois at Urbana-Champaign, earning a Bachelor's Degree in Chemical and Biomolecular Engineering in 2004. Upon graduation, he would move from the cow pastures of central Illinois to the humid wetlands of the ATL to begin graduate studies at the Georgia Institute of Technology where he would earn a Doctor of Philosophy in Chemical and Biomolecular Engineering in August 2008. He currently works in the *exciting* field of patent law at the United States Patent and Trademark Office.